U.S. Department of Transportation

Federal Railroad Administration

Measurement of Vertical Track Deflection from a Moving Rail Car

Office of Research and Development
Washington, DC 20590

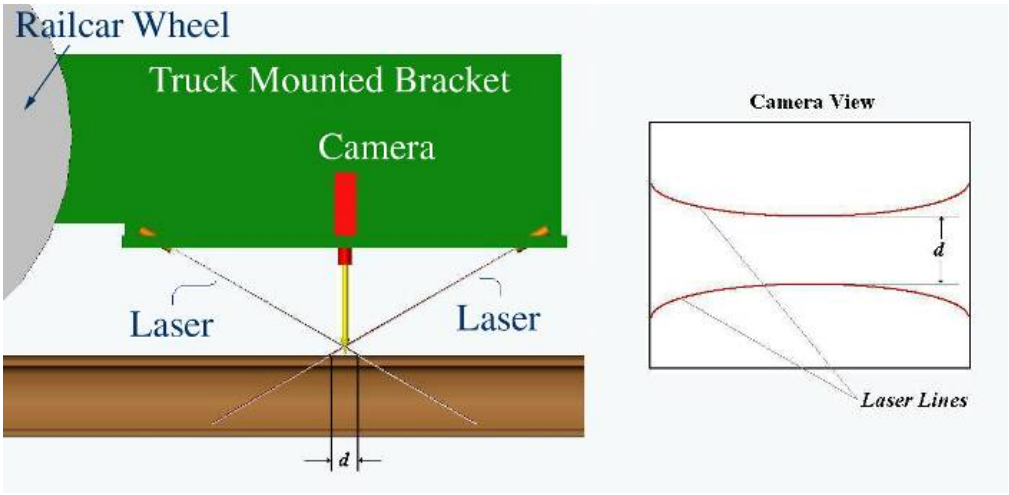

DOT/FRA/ORD-13/08

Final Report
February 2013

NOTICE

This document is disseminated under the sponsorship of the Department of Transportation in the interest of information exchange. The United States Government assumes no liability for its contents or use thereof. Any opinions, findings and conclusions, or recommendations expressed in this material do not necessarily reflect the views or policies of the United States Government, nor does mention of trade names, commercial products, or organizations imply endorsement by the United States Government. The United States Government assumes no liability for the content or use of the material contained in this document.

NOTICE

The United States Government does not endorse products or manufacturers. Trade or manufacturers' names appear herein solely because they are considered essential to the objective of this report.

REPORT DOCUMENTATION PAGE

Form Approved
OMB No. 0704-0188

1. AGENCY USE ONLY (Leave blank)	2. REPORT DATE	3. REPORT TYPE AND DATES COVERED
	February 2013	Technical Report

4. TITLE AND SUBTITLE
Measurement of Vertical Track Deflection from a Moving Rail Car

5. FUNDING NUMBERS

6. AUTHOR(S) and FRA Technical Representative
Shane Farritor and Mahmood Fateh

7. PERFORMING ORGANIZATION NAME(S) AND ADDRESS(ES)
University of Nebraska-Lincoln
Department of Mechanical Engineering
Lincoln, NE 68588

8. PERFORMING ORGANIZATION REPORT NUMBER

9. SPONSORING/MONITORING AGENCY NAME(S) AND ADDRESS(ES)
U.S. Department of Transportation
Federal Railroad Administration
Office of Research and Development
Washington, DC 20590

10. SPONSORING/MONITORING AGENCY REPORT NUMBER
DOT/FRA/ORD-13/08

11. SUPPLEMENTARY NOTES
Program Manager: Mahmood Fateh

12a. DISTRIBUTION/AVAILABILITY STATEMENT
This document is available to the public through the FRA Web site at http://www.fra.dot.gov.

12b. DISTRIBUTION CODE

13. ABSTRACT (Maximum 200 words)

The University of Nebraska has been conducting research sponsored by the Federal Railroad Administration's Office of Research and Development to develop a system that measures vertical track deflection/modulus from a moving rail car. Previous work has suggested the system can find critical maintenance problems not found by other inspection methods including standard track geometry.

The University of Nebraska system uses cameras and lasers to measure a portion of the track deflection basin, and this measurement is used to estimate vertical rail deflection and/or track modulus. This report presents the measurement system along with development of the theory behind the measurement to support diagnosis of track conditions. The results of significant field testing are presented, including the results of a test designed to verify the accuracy of the measurement. A Finite Element Analysis of the measurement is presented along with several variations on closed form solution analysis, based on beam on elastic foundation as well as a discrete support model for rail.

The University of Nebraska system has identified several critical maintenance problems not found by other inspection methods, and all previous studies indicate that measuring track deflection provides unique and valuable insight to track conditions that can improve inspection, maintenance, and safety. Finally, some guidelines are suggested for development of thresholds to guide data interpretation and track condition assessment, but more study and tests are needed to better define threshold criteria.

14. SUBJECT TERMS
Vertical track deflection, track deflection, rail deflection, track measurement system, vertical track modulus, track modulus, track stiffness, track geometry measurement

15. NUMBER OF PAGES
136

16. PRICE CODE

17. SECURITY CLASSIFICATION OF REPORT	18. SECURITY CLASSIFICATION OF THIS PAGE	19. SECURITY CLASSIFICATION OF ABSTRACT	20. LIMITATION OF ABSTRACT
Unclassified	Unclassified	Unclassified	

NSN 7540-01-280-5500
Standard Form 298 (Rev. 2-89)
Prescribed by ANSI Std. 239-18
298-102

METRIC/ENGLISH CONVERSION FACTORS

ENGLISH TO METRIC	METRIC TO ENGLISH
LENGTH (APPROXIMATE)	**LENGTH (APPROXIMATE)**
1 inch (in) = 2.5 centimeters (cm)	1 millimeter (mm) = 0.04 inch (in)
1 foot (ft) = 30 centimeters (cm)	1 centimeter (cm) = 0.4 inch (in)
1 yard (yd) = 0.9 meter (m)	1 meter (m) = 3.3 feet (ft)
1 mile (mi) = 1.6 kilometers (km)	1 meter (m) = 1.1 yards (yd)
	1 kilometer (km) = 0.6 mile (mi)
AREA (APPROXIMATE)	**AREA (APPROXIMATE)**
1 square inch (sq in, in^2) = 6.5 square centimeters (cm^2)	1 square centimeter (cm^2) = 0.16 square inch (sq in, in^2)
1 square foot (sq ft, ft^2) = 0.09 square meter (m^2)	1 square meter (m^2) = 1.2 square yards (sq yd, yd^2)
1 square yard (sq yd, yd^2) = 0.8 square meter (m^2)	1 square kilometer (km^2) = 0.4 square mile (sq mi, mi^2)
1 square mile (sq mi, mi^2) = 2.6 square kilometers (km^2)	10,000 square meters (m^2) = 1 hectare (ha) = 2.5 acres
1 acre = 0.4 hectare (he) = 4,000 square meters (m^2)	
MASS - WEIGHT (APPROXIMATE)	**MASS - WEIGHT (APPROXIMATE)**
1 ounce (oz) = 28 grams (gm)	1 gram (gm) = 0.036 ounce (oz)
1 pound (lb) = 0.45 kilogram (kg)	1 kilogram (kg) = 2.2 pounds (lb)
1 short ton = 2,000 pounds (lb) = 0.9 tonne (t)	1 tonne (t) = 1,000 kilograms (kg)
	= 1.1 short tons
VOLUME (APPROXIMATE)	**VOLUME (APPROXIMATE)**
1 teaspoon (tsp) = 5 milliliters (ml)	1 milliliter (ml) = 0.03 fluid ounce (fl oz)
1 tablespoon (tbsp) = 15 milliliters (ml)	1 liter (l) = 2.1 pints (pt)
1 fluid ounce (fl oz) = 30 milliliters (ml)	1 liter (l) = 1.06 quarts (qt)
1 cup (c) = 0.24 liter (l)	1 liter (l) = 0.26 gallon (gal)
1 pint (pt) = 0.47 liter (l)	
1 quart (qt) = 0.96 liter (l)	
1 gallon (gal) = 3.8 liters (l)	
1 cubic foot (cu ft, ft^3) = 0.03 cubic meter (m^3)	1 cubic meter (m^3) = 36 cubic feet (cu ft, ft^3)
1 cubic yard (cu yd, yd^3) = 0.76 cubic meter (m^3)	1 cubic meter (m^3) = 1.3 cubic yards (cu yd, yd^3)
TEMPERATURE (EXACT)	**TEMPERATURE (EXACT)**
[(x-32)(5/9)] °F = y °C	[(9/5) y + 32] °C = x °F

QUICK INCH - CENTIMETER LENGTH CONVERSION

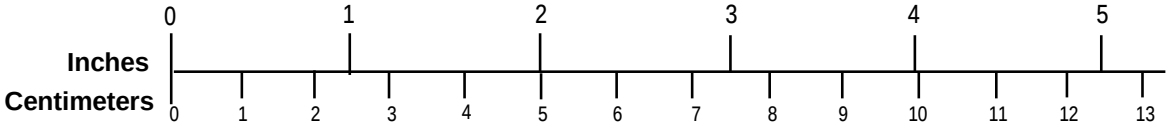

QUICK FAHRENHEIT - CELSIUS TEMPERATURE CONVERSIO

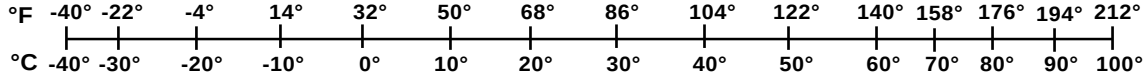

For more exact and or other conversion factors, see NIST Miscellaneous Publication 286, Units of Weights and Measures. Price $2.50 SD Catalog No. C13 10286

Updated 6/17/98

Contents

Illustrations

Tables

Executive Summary

This report documents the research and development work, "Track Modulus Measurement from a Moving Railcar," performed by the University of Nebraska at Lincoln (UNL) under an FRA grant. It is believed that the grant's objective has been met. There is a strong indication of value in the UNL measurement. The report shows that the UNL measurement is different from standard geometry measurements and that the UNL system can find critical maintenance problems not found by other inspection methods. It suggests that there is value in the UNL measurement that could be used to improve railroad operating efficiency and increase safety. Some guidelines are suggested here for implementation of the system. However, it is also clear that more study and tests are needed to define appropriate threshold criteria. The rationale for the indicated confidence in this report for the UNL measurement is based on the extensive validation tests which are documented in the various sections throughout the report. In addition, further confirmation is provided towards the end of the report with finite element modeling using a nonlinear track model.

Based on the prevalent opinions as expressed at the relevant industry conferences, such as the Transportation Research Board (TRB) and the American Railway Engineering and Maintenance-of-way Association (AREMA), there is consensus that both passenger and freight railroad traffic are moving to higher-speeds and higher axle loads as a means to improve efficiency. The heavy axle loads and high speeds of modern freight trains produce high track stresses leading to quicker deterioration of track condition. Fast and reliable methods are vital for identifying and prioritizing track maintenance needs to minimize delays, avoid derailments, and reduce costs.

The condition and performance of railroad track depends on a number of different parameters. Some commonly monitored parameters include internal rail defects, profile, cross level, gage, and gage restraint. More recently, Ground Penetrating Radar (GPR) has been used for track subsurface condition assessment, including track layer thickness, ballast fouling, and drainage. Monitoring these parameters can improve safe train operation by identifying track locations that produce poor vehicle performance or derailment risk. However, at the present time, no effective tool is available to measure one of the most important parameters—vertical track deflection (VTD)—at normal track speeds in real time from a moving rail car. The track deflection measurement could be used to estimate track stiffness by dividing the applied load by the measured deflection. In turn, the track stiffness value is central to the estimation of track modulus. This parameter, VTD, is difficult to measure because no stable reference frame is available on the moving rail car. The UNL approach presented here uses cameras and lasers to measure the shape of the rail relative to the two wheel-rail contact points in a truck assembly. The results herein presented include simulation analysis, extensive field testing, field verification, and a demonstration measurement system that has shown capability of practical implementation in revenue service.

This report presents extensive field validation tests as well as analytical background for the measurement including a full description of the classic Winkler linear model of track deflection and the definition of track modulus as it relates to this model. Some field measurements of track deflection are presented that illustrate the limitations of this model. Two new closed-form analytical models of track deflection are presented that have been produced during this project. The first is a discrete tie analytical model that can represent independent stiffness values for each tie. The second is a new nonlinear closed-form analytical model presented for track deflection.

This model is based on a cubic relationship between distributed load and vertical deflection. The advantages of the nonlinear cubic model are discussed, and this is again related to field measurements of track deflection. Other systems that have been proposed to measure track modulus are included in the discussion.

The practical aspects of the system are addressed, including the basic principle of the proposed measurement and corrections that can be made for pre-existing variations in track profile. This practical implementation of the system culminates in an autonomous system designed for implementation in revenue service. Also included in this discussion is a fully defined method for system calibration. A series of field tests that were designed and conducted to validate the measurement system under many conditions are presented. This effort included using several independent measurement techniques to confirm the UNL measurement at several locations on real track, and related investigations of how the measurement did or did not change with vehicle speed and vehicle direction. The results of these extensive field tests include site visits to manually validate the measurements. These tests occurred on several thousand miles of revenue service track on various host railroads. Included is an analysis of some specific track locations where variations in modulus are known problems and how these locations can change over time. Specifically, an analysis of various bridge approaches is shown. This work has identified several locations where the track support is extremely complex and the track does not behave according to conventional norms. More work will be needed to fully understand these potentially significant locations.

1 Introduction

This report documents the research and development work performed to measure VTD from a moving rail car. These deflection measurements can be used to estimate track modulus. The developed system uses a noncontact vision sensor system to make displacement measurements with respect to the wheel-rail contact point. The system is inexpensive and does not require significant equipment support and personnel. It is capable of autonomous operation in revenue service.

1.1 Statement of Problem and Task Goals

The economic constraints of both passenger and freight railroad traffic are moving the railroad industry to higher-speed vehicles and heavier axle loads. The heavy axle loads and high speeds of modern freight trains produce high track stresses leading to quicker deterioration of track condition. As a result, the need for track maintenance increases. Fast and reliable methods are needed to identify and prioritize track in need of maintenance to minimize delays, avoid derailments, and reduce maintenance costs.

The condition and performance of railroad track depends on a number of different parameters. Some of the factors that influence track quality are track support (defined by track modulus/stiffness/deflection), internal rail defects, profile, crosslevel, gage, and gage restraint. Monitoring these parameters can improve safe train operation by identifying track locations that produce poor vehicle performance or derailment potential. Track monitoring also provides information for optimizing track maintenance activities by focusing activities where maintenance is critical and by selecting more effective maintenance and repair methods.

Automated methods of inspection are available for most of the parameters that are included in track geometry (Li et al., 2002). However, at the present time, no vehicle is available to measure track deflection, one of the most important parameters, at normal track speeds in real time. The track deflection measurement could be used to estimate track stiffness by dividing the applied load by the measured deflection. In turn, the track stiffness value is central to the estimation of track modulus, which has been defined as the coefficient of proportionality between the rail deflection and the vertical contact pressure between the rail base and track foundation (Cai et al., 1994) in Beam on Elastic Foundation Theory but will be extended in this report. In other words, track modulus is the supporting force per unit length of rail per unit rail deflection (Selig and Li, 1994), assuming the track support is continuous and elastic. Track modulus is a single parameter that represents the effects of all of the track components under the rail (Cai et al., 1994). These components include the subgrade, ballast, subballast, ties, and tie fasteners. Track modulus is particularly useful for the design of new track and the evaluation of good quality track where the assumptions of the theory are not violated. Also, it should be noted that the track stiffness/modulus can dramatically vary over a very short distance such as from one tie to the next. Therefore, it can be appropriate to talk about an average modulus value over a characteristic length of track (e.g., 10 or 100 feet (ft)).

The characteristics of track support including measurement of track modulus, stiffness, or deflection are important because they significantly affect track performance and maintenance requirements. Both low track modulus and large variations in track modulus are undesirable. Low track modulus has been shown to cause differential settlement that subsequently increases maintenance needs (Ebersohn et al., 1993; Read et al., 1994). Large variations in track modulus,

such as those often found near bridges and crossings, have been shown to increase dynamic loading (Davis et al., 2003; Zarembski and Palese, 2003). Increased dynamic loading reduces the life of the track components, resulting in shorter maintenance cycles (Davis et al., 2003). It has been shown that reducing variations in track modulus at grade (i.e., road) crossings leads to better track performance and less track maintenance (Zarembski and Palese, 2003). It also has been suggested that track with a high and consistent modulus will allow for higher train speeds and therefore increase both performance and revenue (Heelis et al., 1999). Ride quality, as indicated by vertical acceleration, is also dependent on track modulus.

The ultimate goal of this project is to provide a system capable of measuring VTD and modulus from a moving car at a high speed. The track deflection measurement would be used to estimate track stiffness or modulus depending on the track conditions and intent of the survey. The measurement system can be used as a tool for maintenance planning, track design, and acceptance of newly constructed and reconstructed track.

1.2 Previous United States Track Modulus Measurement Systems

Previous localized field testing has shown that it is possible to measure areas of low track modulus, variable track modulus, void deflection, variable total deflection, and inconsistent rail deflection (Ebersohn and Selig, 1994; Sussmann et al., 2001). In the past, such systems have been used to identify sections of track with poor performance. These measurements have been useful. However, they are expensive and have only been made over short distances (in the range of tens of meters). The ability to make these measurements continuously over large sections of track is desirable (Ebersohn and Selig, 1994; Read et al., 1994).

One vehicle, called the Track Loading Vehicle (TLV), uses this approach (Thompson and Li, 2002). This vehicle is capable of measuring track modulus at speeds up to 16.1 kilometers per hour (km/hr) (10 miles per hour (mph)). The TLV uses two cars, each with a center load bogie capable of applying loads from 4.45 to 267 kilonewtons (kN) (1–60 kilopounds per second (kips)). A light load (13.3 kN or 3 kips) is applied by the first vehicle, whereas a heavier load is applied by the second vehicle. A laser-based system on each vehicle measures the deflections of the rail caused by the center load bogies. The test procedure involves two vehicles that pass over a section of track—first applying a 44.5-kilonewton (10 kip) load and then a 178-kilonewton (40 kip) load (Thompson and Li, 2002). The use of two loads eliminates the problems with the Winkler assumptions as described in Figure 2-8. Both the light load and the heavier load are large enough to remove the track "slack" (i.e. low stiffness at low loads as in Figure 2-5). The use of two loads (if properly chosen) then becomes an approximation of the modulus defined by the derivative in Equation 2.2-12.

Although the TLV is operational, it does have limitations. First, tests are often performed at speeds below 16.1 km/hr (10 mph); therefore, it is difficult to test long sections of track (hundreds of miles). Second, significant expense in both equipment and personnel are required for operation. For these reasons, the TLV has not yet been widely implemented.

1.3 Related Track Measurements

Track geometry data includes the measurement of track gage, alignment, cross level, curvature, etc. The data is collected with track geometry vehicles. The geometry cars are equipped with instruments, measuring devices, and computers necessary to calculate track geometry. Some track geometry vehicles are equipped with a Gage Restraint Measurement System (GRMS) that

can apply known lateral and vertical loads to the track structure and measure the gage restraint capacity of crossties and rail fasteners.

Ground-penetrating radar (GPR) is a geophysical method that uses radar pulses to image the subsurface. This nondestructive method uses electromagnetic radiation in the microwave band (UHF/VHF frequencies) of the radio spectrum and detects the reflected signals from subsurface structures. The technology has been implemented into detecting fouling ballast and mapping subballast and subgrade. These are the physical changes in the roadbed often causing track deflection variations. The ability to detect these changes makes GPR a useful tool to diagnose causes of track deflection variations that are not obvious from the surface.

None of the track geometry, GRMS, or GPR technologies can evaluate the load-deflection response of the track. A track deflection or stiffness measurement is important to implement to ensure that a complete set of track characteristic measurements is available for maintenance planning, safety assessment, and vehicle track interaction analyses.

2.1.1 Track Mechanics

The relationship between applied loads and track deformations is an important parameter to be considered in proper track design and maintenance. A representative mathematical model that accurately describes this relationship is desirable.

2.1.1.1 The Winkler Model of Track Deflection

The Beam on an Elastic Foundation (BOEF) model, also known as the Winkler model, describes a point load applied to an infinite beam on an infinite elastic foundation. It assumes the distributed supporting force of the track foundation is linearly proportional to the vertical rail deflection (i.e., $p(x)=uw(x)$). Here, the coefficient u is defined as track modulus. The differential equation then becomes:

$$EI\frac{d^4w(x)}{dx^4}+uw(x)=q(x) \qquad \text{Equation 1.2-1}$$

This model has been shown to be an effective method for determining track modulus (Raymond, 1985; Meyer, 2002), and derivations can be found in Kerr (1976) and Boresi and Schmidt (2003). The vertical deflection of the rail, w, as a function of longitudinal distance along the rail x (referenced from the position of the applied load) is given by:

$$w(x)=-\frac{P\beta}{2u}e^{-\beta\cdot x}\left[\cos(\beta x)+\sin(\beta x)\right] \qquad \text{Equation 1.2-2}$$

$$\beta=\left(\frac{u}{4EI}\right)^{\frac{1}{4}} \qquad \text{Equation 1.2-3}$$

where: P is the load on the track

u is the track modulus

E is the modulus of elasticity of the rail

I is the moment of inertia of the rail

x is the longitudinal distance along the rail

When multiple loads are applied, the rail deflections caused by each of the loads are superposed (assuming small vertical deflections) (Boresi and Schmidt, 2003).

A plot of the rail deflection given by the Winkler model over the length of a four-axle coal hopper is shown in Figure 2-1. The deflection is shown relative to the wheel/rail contact point for five different reasonable values of track modulus (6.89, 13.8, 20.7, 27.6, and 34.5 megapascals (MPa) corresponding to 1,000, 2,000, 3,000, 4,000, and 5,000 pounds per square inch (psi), respectively). The model assumes a 115-pound rail with an elastic modulus of 206.8 gigapascals (30,000,000 psi) and an area moment of inertia of 2,704 centimeters (cm)^4 (64.97 inches (in)^4).

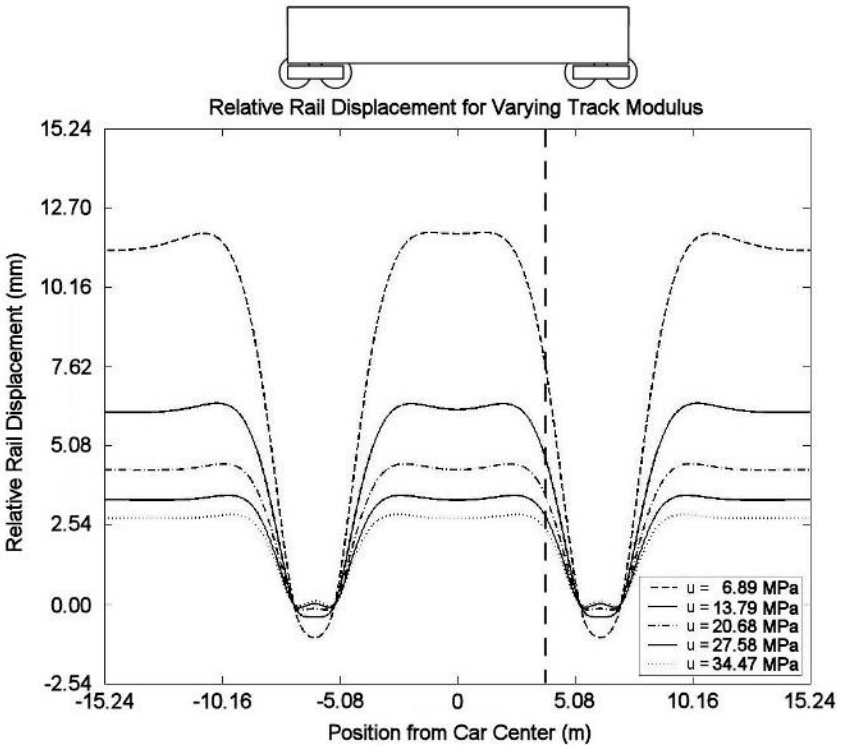

Figure 2-1. Relative Rail Displacement under a Rail Car

The limitations of the Winkler model are clear given the widely accepted nonlinearity of track structure. However, this model is often used because it does provide a clear closed-form solution to the relationship between load and deflection in track structure.

2.1.1.2 A Discrete Tie Model of Track Deflection

In this section, a new discrete tie model is presented that is an output of this project. This model has been described previously (e.g., Norman, 2004). The discrete support model describes the rail supported on a number of discrete springs with a single force applied. The discrete springs represent support at the crossties, and the single applied load represents one rail-car wheel. At this time, tie support is modeled by linearly elastic springs. This model is more applicable at low speeds, but future work will include viscoelastic behavior. It is expected that measurements of track modulus may vary with train speed because of damping. However, the experimental results in this paper suggest the influence of track damping may not be significant at speeds below 48 km/h (30 mph).

The discrete tie model is shown to be useful in the experimental results because track modulus can vary from tie to tie. The proposed model considers only finite lengths of rail and a finite number of ties (Figure 2-2). To reduce the model's computational requirements (so it can be implemented in real time), the rail is assumed to extend beyond the ties and is fixed at a (large) distance from the last tie. This ensures the boundary conditions are well defined (the rail is flat and far away), and the rail shape is continuous.

The deflection in each of the springs (i.e. the rail deflection) can be determined by first solving for the forces in each of the springs by using energy methods. The principles of stationary

potential energy and Castigliano's theorem on deflections are applied (Boresi and Schmidt, 2003). For these methods to be applicable, small displacements and linear elastic behavior is assumed. The number of equations needed to determine the forces in the springs is equal to the number of springs (i.e., spring forces are the unknowns).

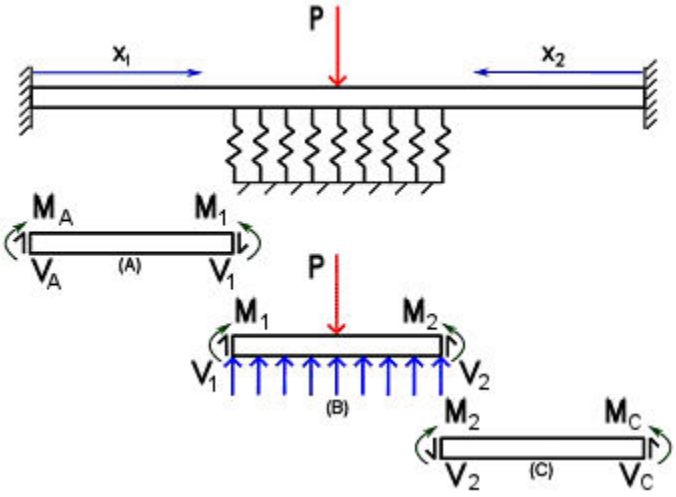

Figure 2-2. Discrete Model and Free Body Diagram

The discrete support model is similar to the Winkler model when the ties are uniformly spaced and have uniform stiffness, and the rail is long. Nine ties are used in this work, and experimental trackside measurements have shown this to be sufficient (Norman, 2004).

The moment and shear force in the cantilevered sections of the model (Figure 2-2 (A) and (C)) can now be calculated. Static equilibrium requires the moment and shear force, for Section A, to be:

$$M_1 = M_A + V_A x_1 \qquad \text{Equation 1.2-4}$$

$$V_1 = V_A \qquad \text{Equation 1.2-5}$$

Likewise, for Section C:

$$M_2 = M_C + V_C x_2 \qquad \text{Equation 1.2-6}$$

$$V_2 = V_C \qquad \text{Equation 1.2-7}$$

Now, the forces in the springs can be determined with energy methods (Figure 2-2(B)). Section B is split into segments separated by the springs, and the segment's internal moments are found to determine the beam's strain. Energy from shear force is small and is neglected (Norman, 2004).

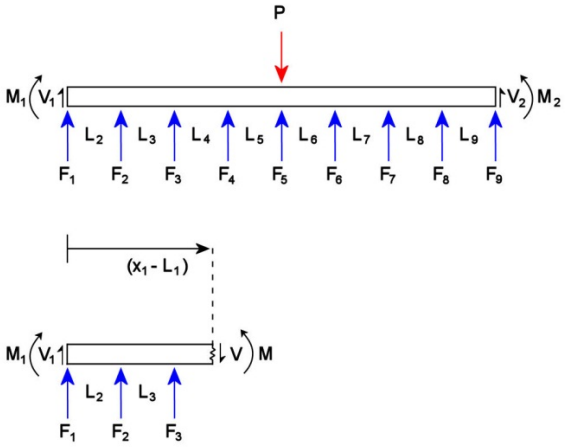

Figure 2-3. Middle Segment of Discrete Tie Model

The equations for the internal moments in each segment can be written (Equations 1.2-8 – 1.2-17), where moments M_1 and M_2, and the shear forces V_1 and V_2 are given by Equations 1.2-4 – 1.2-7 above. The lengths of each of the segments (i.e., tie spacing) in the beam are given by L_1 – L_{10}, and the spring forces are denoted by $F_1 - F_9$.

$$M = M_1 \quad \text{for } 0 \le x_1 \le L_1 \qquad \text{Equation 1.2-8}$$

$$M = -\left[M_1 + V_1(x_1 - L_1) + F_1(x_1 - L_1)\right] \quad \text{for } L_1 \le x_1 \le L_1 + L_2 \qquad \text{Equation 1.2-9}$$

$$M = -\left[M_1 + V_1(x_1 - L_1) + F_1(x_1 - L_1) + F_2(x_1 - L_1 - L_2)\right] \quad \text{for } L_1 + L_2 \le x_1 \le L_1 + L_2 + L_3 \qquad \text{Equation 1.2-10}$$

$$M = -\begin{bmatrix} M_1 + V_1(x_1 - L_1) + F_1(x_1 - L_1) + F_2(x_1 - L_1 - L_2) \\ + F_3(x_1 - L_1 - L_2 - L_3) \end{bmatrix} \quad \text{for } L_1 + L_2 + L_3 \le x_1 \le L_1 + L_2 + L_3 + L_4 \qquad \text{Equation 1.2-11}$$

$$M = -\begin{bmatrix} M_1 + V_1(x_1 - L_1) + F_1(x_1 - L_1) + F_2(x_1 - L_1 - L_2) \\ + F_3(x_1 - L_1 - L_2 - L_3) + F_4(x_1 - L_1 - L_2 - L_3 - L_4) \end{bmatrix} \quad \text{for } L_1 + L_2 + L_3 + L_4 \le x_1 \le L_1 + L_2 + L_3 + L_4 + L_5 \qquad \text{Equation 1.2-12}$$

$$M = \begin{bmatrix} M_2 + V_2(x_2 - L_{10}) + F_9(x_2 - L_{10}) + F_8(x_2 - L_{10} - L_9) \\ + F_7(x_2 - L_{10} - L_9 - L_8) + F_6(x_2 - L_{10} - L_9 - L_8 - L_7) \end{bmatrix} \quad \text{for } L_{10} + L_9 + L_8 + L_7 \le x_2 \le L_{10} + L_9 + L_8 + L_7 + L_6 \qquad \text{Equation 1.2-13}$$

$$M = \begin{bmatrix} M_2 + V_2(x_2 - L_{10}) + F_9(x_2 - L_{10}) + F_8(x_2 - L_{10} - L_9) \\ + F_7(x_2 - L_{10} - L_9 - L_8) \end{bmatrix} \quad \text{for } L_{10} + L_9 + L_8 \le x_2 \le L_{10} + L_9 + L_8 + L_7 \qquad \text{Equation 1.2-14}$$

$$M = \left[M_2 + V_2(x_2 - L_{10}) + F_9(x_2 - L_{10}) + F_8(x_2 - L_{10} - L_9)\right] \quad \text{for } L_{10} + L_9 \le x_2 \le L_{10} + L_9 + L_8 \qquad \text{Equation 1.2-15}$$

$$M = \left[M_2 + V_2(x_2 - L_{10}) + F_9(x_2 - L_{10})\right] \quad \text{for } L_{10} \le x_2 \le L_{10} + L_9 \qquad \text{Equation 1.2-16}$$

$$M = -M_2 \quad \text{for } 0 \le x_2 \le L_{10} \qquad \text{Equation 1.2-17}$$

In the above equations, the shear forces, moments, and spring forces are all unknown; however, one spring force can be determined by a vertical force balance:

$$F_1 = P - V_1 - V_2 - F_2 - F_3 - F_4 - F_5 - F_6 - F_7 - F_8 - F_9 \qquad \text{Equation 1.2-18}$$

where P is a known wheel load (e.g., 157 kN or 35 kips). Now, the strain energy can be written where k_i is the stiffness of spring i:

$$\begin{aligned} U = {} & \int_0^{L_1} \frac{M^2}{2EI}\,dx_1 + \int_{L_1}^{L_1+L_2} \frac{M^2}{2EI}\,dx_1 + \int_{L_1+L_2}^{L_1+L_2+L_3} \frac{M^2}{2EI}\,dx_1 + \int_{L_1+L_2+L_3}^{L_1+L_2+L_3+L_4} \frac{M^2}{2EI}\,dx_1 \\ & + \int_{L_1+L_2+L_3+L_4}^{L_1+L_2+L_3+L_4+L_5} \frac{M^2}{2EI}\,dx_1 + \int_0^{L_{10}} \frac{M^2}{2EI}\,dx_2 + \int_{L_{10}}^{L_{10}+L_9} \frac{M^2}{2EI}\,dx_2 + \int_{L_{10}+L_9}^{L_{10}+L_9+L_8} \frac{M^2}{2EI}\,dx_2 \\ & + \int_{L_{10}+L_9+L_8}^{L_{10}+L_9+L_8+L_7} \frac{M^2}{2EI}\,dx_2 + \int_{L_{10}+L_9+L_8+L_7}^{L_{10}+L_9+L_8+L_7+L_6} \frac{M^2}{2EI}\,dx_2 + \frac{F_1^2}{2k_1} + \frac{F_2^2}{2k_2} + \frac{F_3^2}{2k_3} \\ & + \frac{F_4^2}{2k_4} + \frac{F_5^2}{2k_5} + \frac{F_6^2}{2k_6} + \frac{F_7^2}{2k_7} + \frac{F_8^2}{2k_8} + \frac{F_9^2}{2k_9} \end{aligned} \qquad \text{Equation 1.2-19}$$

Castigliano's theorem is now used to create the number of equations needed to solve for the unknown spring forces and boundary conditions (moment and shear force). In this case, there

are 12 unknown variables (8 spring forces, 2 reaction moments, and 2 reaction forces). From Castigliano's theorem:

$$\frac{\partial U}{\partial F_2} = \frac{\partial U}{\partial F_3} = \frac{\partial U}{\partial F_4} = \frac{\partial U}{\partial F_5} = \frac{\partial U}{\partial F_6} = \frac{\partial U}{\partial F_7} = \frac{\partial U}{\partial F_8} = \frac{\partial U}{\partial F_9} = 0,$$
$$\frac{\partial U}{\partial M_A} = \frac{\partial U}{\partial M_B} = 0, \quad \text{and} \quad \frac{\partial U}{\partial V_A} = \frac{\partial U}{\partial V_B} = 0 \qquad \text{Equation 1.2-20}$$

With these relationships, a set of 12 equations and 12 unknowns are developed by substituting the moment expressions (1.2-4 – 1.2-18) into (1.2-19). These expressions can be written in matrix form:

$$\mathbf{MF} = \mathbf{P} \qquad \text{Equation 1.2-21}$$

where:

P is the load vector

M is a 12 x 12 matrix of coefficients of the external forces

F is a column vector of the external forces $F_2 – F_9$, M_A, V_A, M_B, and V_B

The solution to this matrix equation gives the forces in each of the springs. Now, the spring deflections are:

$$d_i = \frac{F_i}{k_i} \qquad \text{Equation 1.2-22}$$

where:

d_i is the deflection of spring i

F_i is the force in spring i

k_i is the stiffness of spring i

The two models are now compared. Experimental results have shown the Winkler model is a good representation of track deflection (Zarembski and Choros, 1980; Norman, 2004). Therefore, the discrete model should give results similar to the Winkler model for similar inputs. However, the discrete model will have the additional ability to represent nonuniform track.

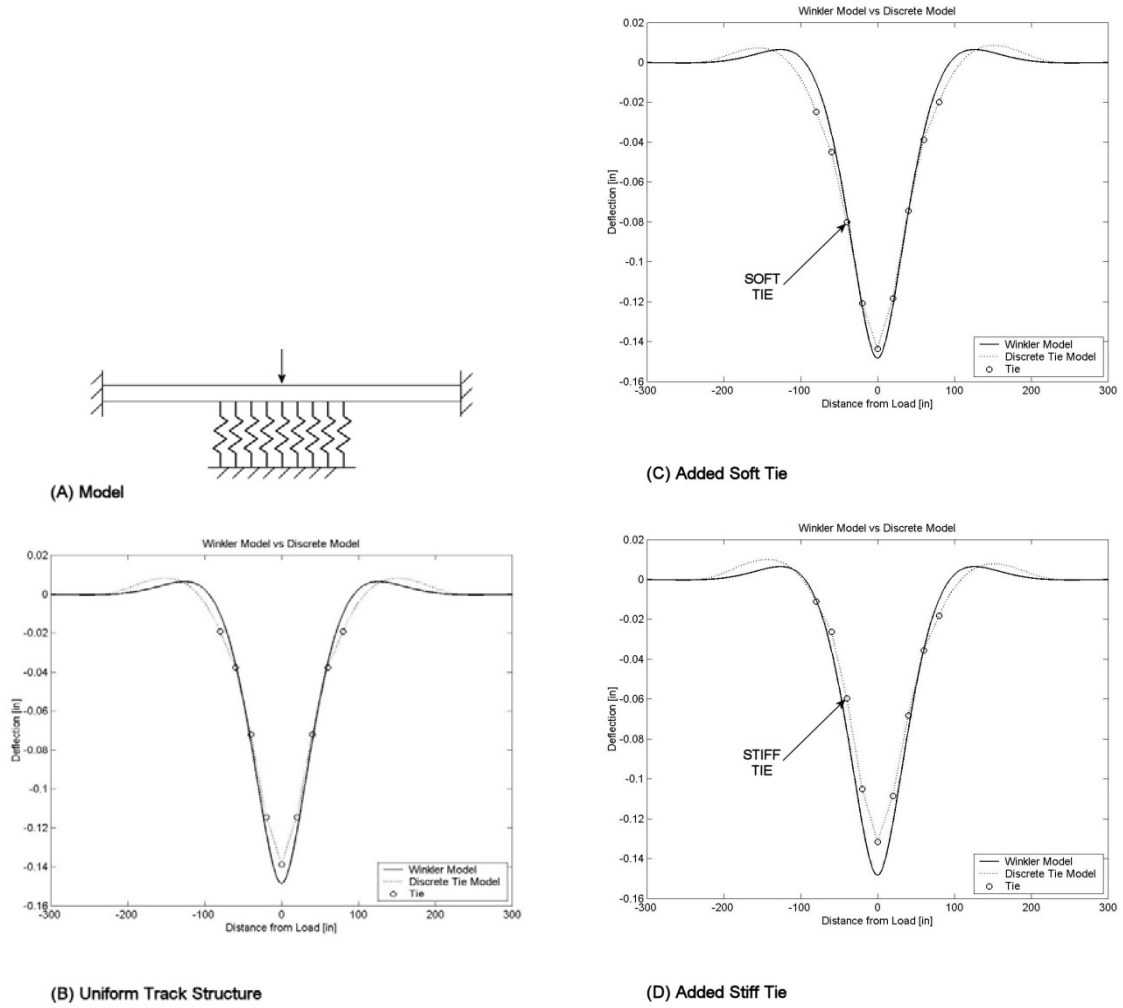

Figure 2-4. Comparison of Winkler and Discrete Models

Figure 2-4(B) compares the deflections from the two models for uniform modulus. The continuous line represents the Winkler model, and the boxes indicate the tie locations in the discrete model. The track modulus used in the Winkler model was 20.7 MPa (3,000 pounds-force (lbf)/in/in), and the corresponding tie stiffness was 10.5 MN/m (60,000 lbf/in). Track modulus is equated to tie stiffness by dividing by the tie spacing (ties spacing of 50.8 cm (20 in)). A single point load of 157 kN (3,575 lbf) (representing a single vehicle wheel) was applied over the center tie. The deflection predicted by both models is very similar with a maximum change of 6.47 percent (relative to the accepted Winkler model is correct).

Real track has nonuniform modulus and these differences can be represented by the discrete model. In Figure 2-4(C), the stiffness of the third tie from the left end has been decreased by 50 percent (to 5.25 meganewtons per meter (MN/m) or 30,000 lbf/in). In Figure 2-4(D), the stiffness of the third tie has been increased by 100 percent (to 21.0 MN/m or 120,000 lbf/in). In both of these cases, the Winkler model is shown with a uniform modulus.

The track deflection with a single soft tie (Figure 2-4(C)) is no longer symmetric about the loading point. The rail is deflected more on the left side of the load where the soft tie is located. The maximum deflection of the rail was also slightly increased (by approximately 0.1219 mm

(0.0048 in)). Figure 2-4(D) shows the rail deflection where the stiffness of the third tie has been doubled to 21.0 MN/m (120,000 lbf/in). The discrete model shows that the deflection near the stiff tie and the maximum deflection have both decreased (by approximately 0.1829 mm (0.0072 in)). The results from these examples show that 1) the two models give similar results for similar inputs, and 2) the deflection curve can be affected by a single tie.

2.1.1.3 A Cubic Model of Track Deflection

Another model of track deflection was developed as an output of this project. This model is based on a cubic relationship between rail deflection and the supporting distributed load. This model has been previously published in McVey (2006).

Field tests conducted by the American Society of Civil Engineers (ASCE) Special Committee on Stresses in Railroad Track (1918) clearly showed that the vertical rail deflections were not linearly proportional to the wheel loads. An extensive experimental study conducted by Zarembski and Choros (1980) also clearly documented this nonlinear response.

Figure 2-5 shows the experimental results of the track responses under various applied loads. This experiment was conducted by UNL at Level, NE. Rail deflection was measured at given locations by using linear variable differential transformers (LVDTs) as a short, slow moving train of known weight passed. The axles of the train weighed 150,600 N (33,850 lbf), 60,230 N (13,540 lbf), and 30,650 N (6,890 lbf). The LVDTs were mounted to steel rods (about 1 m (3ft)) driven into the subgrade to provide a stable reference. The LVDTs then measured the vertical motion of the flange relative to the steel rod. The results from four LVDTs are shown in Figure 2-5. Here, the LVDTs were placed at 1 m (3 ft) increments along the track (x = 1m, 2m, 3m, and 4m).

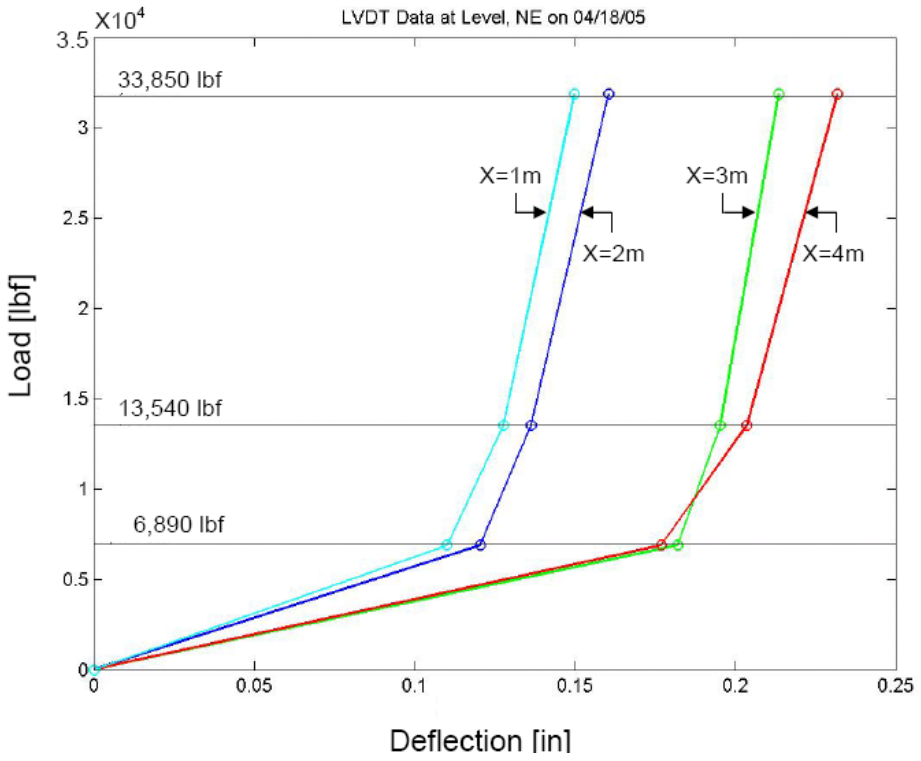

Figure 2-5. Deflection of Track under Three Loads

These measurements, along with many others dating back to the Talbot report (ASCE-AREA Special Committee, 1918), clearly indicate that the vertical rail deflections are not linearly proportional to the wheel loads. It is also important to note that the "degree" of nonlinearity can change dramatically over very short distances along the track. Note the deflection of the track under the 30,650 N (6,890 lbf) load increased about 60 percent over a distance of 1 m. This nonlinearity and variability greatly complicates determining and modeling track structure and violates most assumptions of the Beam on Elastic Layer Theory. Several methods have been developed for calculating modulus with each method assuming a different definition of track modulus that approximates the nonlinear behavior of real track.

Here, a new model is proposed that represents the relationship between vertical rail deflection and the distributed rail support force, $p(x)$, as a cubic polynomial as defined in Equation 2.2-4 below. To support this approach, this relationship to the experimental results of (Zarembski and Choros, 1980) are plotted in Figure 2-6, along with a cubic polynomial curve fit between the distributed rail support force and displacement. The cubic polynomial fits the experimental results very well ($R^2 = 0.9987$).

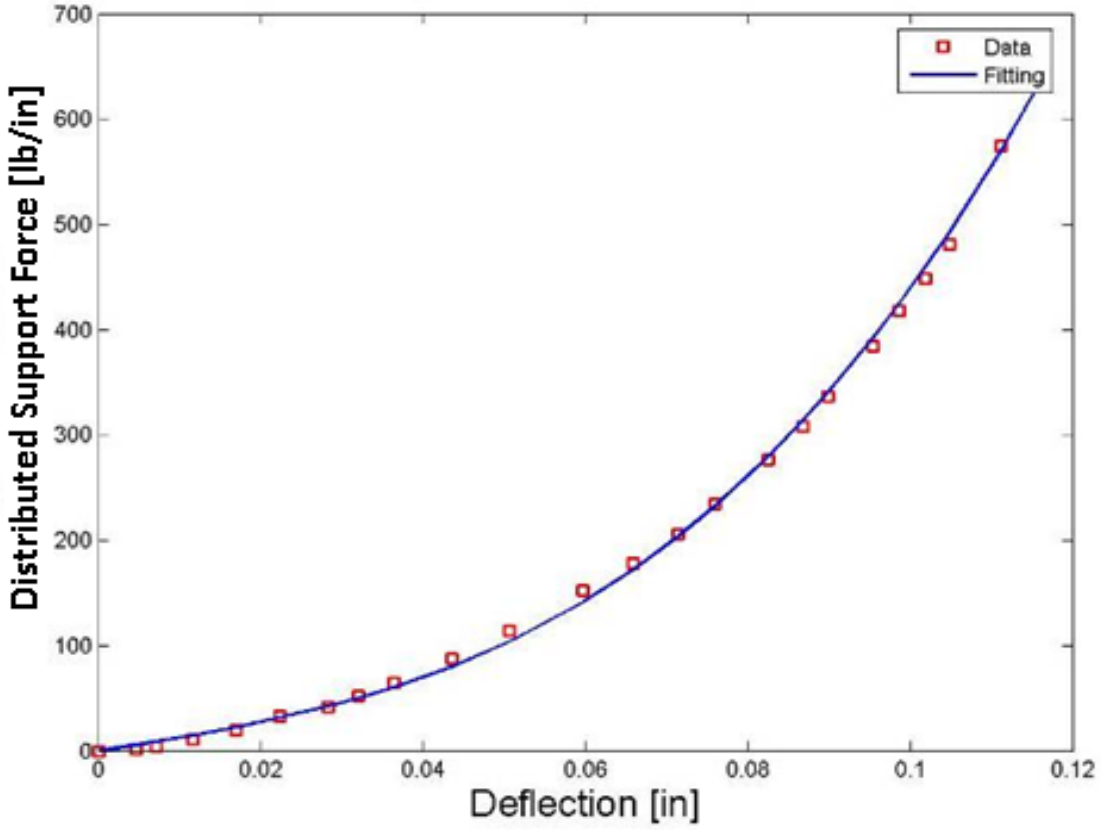

Figure 2-6. Experimental Data and Curve Fitting (Zarembski and Choros, 1980)

Using a cubic polynomial has several advantages. First, it captures the behavior of real track in that it provides for low stiffness at low loads and higher stiffness at higher loads, such as is shown in the field measurements of Figure 2-5. Also, negative displacement of the track (track lift) does not result in significant downward forces being applied to the rail. Unlike the previous models, the cubic polynomial closely represents the fact that if the track rises slightly, the ballast does not pull the track down.

Here, the supporting distributed load *p(x)* has a cubic relationship between *p(x)* and *w(x)*:

$$p(x) = u_1 w(x) + u_3 w(x)^3 \qquad \text{Equation 1.2-23}$$

Note that symmetry about the applied load requires the second order term to vanish. Substitution into the BOEF model gives the following differential equation:

$$EI \frac{d^4 w}{dx^4} + u_1 w + u_3 w^3 = q \qquad \text{Equation 1.2-24}$$

Equation 1.2-24 is a nonlinear differential equation, and a closed-form analytical solution is not straightforward. One analytical approximation based on Cunningham's method can be found by

McVey (2006). However, a numerical solution for this boundary value problem (BVP) can be obtained.

The BVP can be written in state space notation as:

$$\underline{w'} = f(\underline{w}, x) \qquad \text{Equation 1.2-25}$$

$$\underline{w'} = \frac{\partial}{\partial x}\begin{bmatrix} w(x) \\ w'(x) \\ w''(x) \\ w'''(x) \end{bmatrix} = f(\underline{w}, x) \qquad \text{Equation 1.2-26}$$

Given Equation 1.2-26, the BVP becomes:

$$\frac{\partial}{\partial x}\begin{bmatrix} w(x) \\ w'(x) \\ w''(x) \\ w'''(x) \end{bmatrix} = \begin{bmatrix} w'(x) \\ w''(x) \\ w'''(x) \\ -\frac{1}{EI}\left(u_1 w(x) + u_3 w^3(x)\right) \end{bmatrix} \qquad \text{Equation 1.2-27}$$

As the name implies, the fourth-order BVP described above requires the value of four boundary conditions which are displayed in the following equations:

$$\begin{aligned} w(x)|_{x=\infty} &= 0 \\ w(x)|_{x=-\infty} &= 0 \\ w'(x)|_{x=0} &= 0 \\ w(x)|_{x=0} &= w_o \end{aligned} \qquad \text{Equation 1.2-28}$$

Now, because the BVP can have more than one correct solution, an initial "guess" for the last boundary condition is needed in order for the solution to converge to an expected solution. In this case, the initial guess is provided by the Winkler model evaluated at $x = 0$ and $u = u_3$.

$$w(0) = w_o = -\frac{P\beta}{2u_3} \quad \text{where}: \beta = \left(\frac{u_3}{4EI}\right)^{\frac{1}{4}} \qquad \text{Equation 1.2-29}$$

The mechanics of this problem also require the solution be found subject to the additional constraint given by symmetry about the load:

$$\int_0^\infty \left(u_1 w + u_3 w^3\right) dx = \frac{P}{2} \qquad \text{Equation 1.2-30}$$

The unique solution that satisfies each of these constraints will give the rail deflection. Many numerical techniques can be used to solve this well-posed BVP. In this work, the "bvp4c" function in Matlab (Kierzenka and Shampine, 2001) was used.

Although the cubic model closely represents the deflection test data over the entire range of wheel loads, the accuracy of the linear analysis depends on the magnitude of the test load.

Computed deflections for loads other than the test load will have an error of the nonlinearity and the fact that the linearization results in accurate predictions where the linearization intersects the nonlinear behavior.

Because the cubic spring is initially softer than the one in the Winkler model, the rail must deflect more before the base can pick up the full load. This means that the distributed load will be spread over a wider span than for the linear model as shown in Figure 2-7, which makes logical sense with expected behavior of railway track.

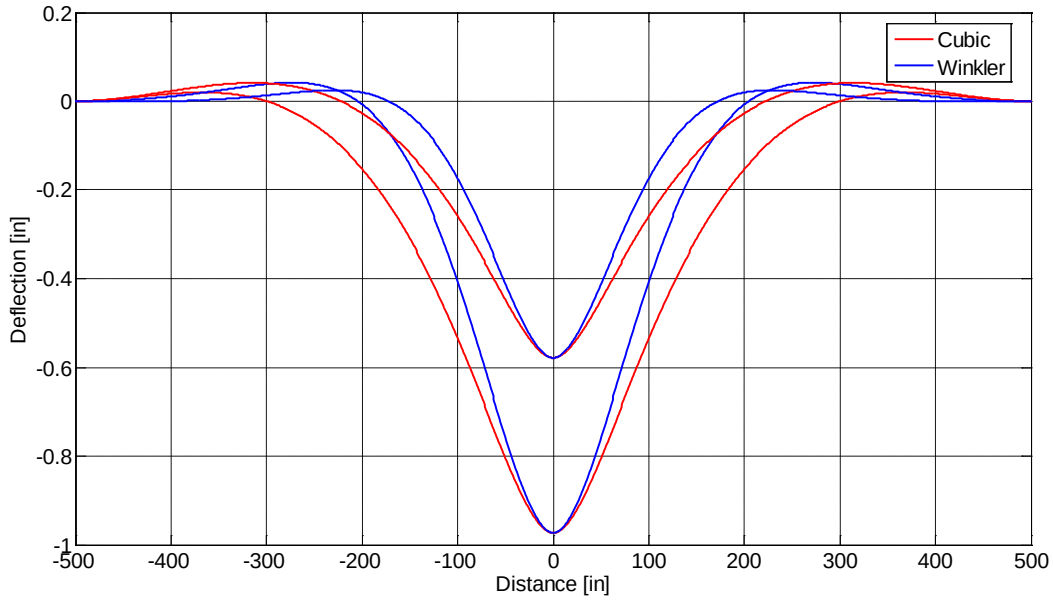

Figure 2-7. Comparison of Cubic and Winkler Models

It is proposed that a good definition of track modulus is the variation in supporting distributed force relative to the variation in deflection near the characteristic load for a given track (Lu et al., 2008). This characteristic load might be defined as the nominal axle load for a given freight line (e.g., 160 kN or 286,000/8 = 36 kips). This can be expressed mathematically as the derivative of the pressure-deflection curve evaluated at the characteristic load *P**:

$$u^* = \left.\frac{\partial p}{\partial w}\right|_{P^*} \qquad \text{Equation 1.2-31}$$

where: u^* is the characteristic track modulus

p is the supporting force per unit length of rail

P^* is the characteristic load corresponding to a given rail line

To evaluate the derivative at the characteristic load, the load must again be transformed to a distributed load. This can be done with the linear assumptions as described previously (the Winkler model). This definition of track modulus has been used in field measurements (Arnold et al., 2006).

Finally, in the nonlinear cubic model described previously, the track modulus at characteristic load can be calculated as:

$$u^* = \left.\frac{\partial p}{\partial w}\right|_{P^*} = \left.\frac{\partial\left(u_1 w + u_3 w^3\right)}{\partial w}\right|_{P^*} = u_1 + 3u_3 w^2\Big|_{P^*} \qquad \text{Equation 1.2-32}$$

This definition of track modulus is compared with the Winkler model as shown in Figure 2-8. In this figure, the load deflection curve is plotted from the experimental data of Zarembski and Choros (1980) shown in Figure 2-6.

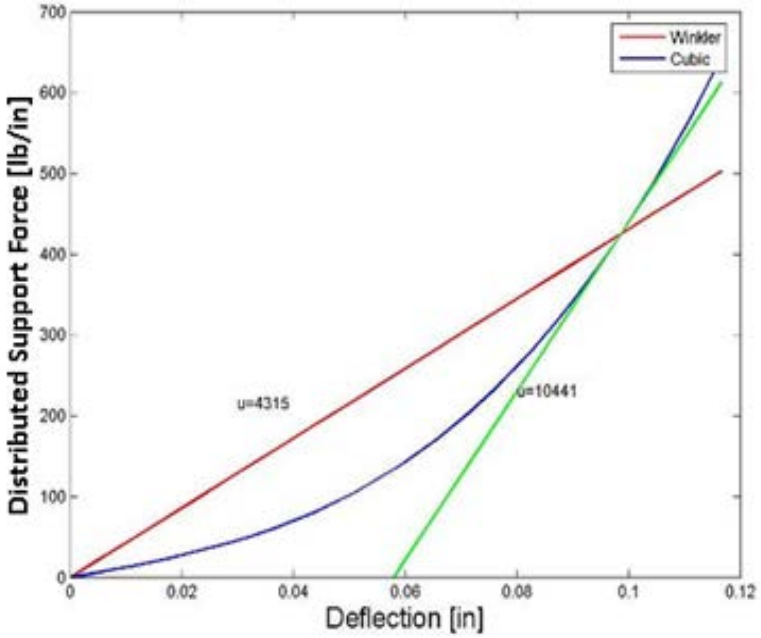

Figure 2-8. Modulus Calculations in Winkler and Cubic Models

It is clear that for single data points at higher loads the Winkler model will always underestimate the actual track modulus (Figure 2-8). As seen in this figure, the line connecting the point of zero load and zero deflection with the point of actual load and actual deflection (red line with slope of 4,315). The Winkler model will also poorly represent changes in deflection with respect to changes in distributed load at these higher values because the slope of the modulus curve is much lower with the Winker model.

3 Overall Approach

The UNL system measures the rail height relative to the line created by the wheel/rail contact points. This measurement of track deflection is combined with an analytical model of the track structure to estimate the track stiffness and track modulus. The system currently operates continuously over long distances and in revenue service.

3.1 The UNL Measurement

3.1.1 Measurement Principle and Methodology

The geometry of the measurement system is shown in Figure 3-1. An instrumented beam is rigidly mounted on the side frame of a hopper car and extends a few feet away from the wheels. A sensor head, which includes a laser/camera system, is attached to the end of the beam. The sensor system has two line lasers and a camera as shown in Figure 3-2. The line lasers intersect the rail surface at an acute angle to create curves across the surface of the rail. Using line lasers allows the system to compensate for lateral movement of the rail relative to the camera and for changes in rail profile. The camera captures images showing two curved laser lines on the rail surface, and the distance between the lines, *d*, is obtained by an image processing program. This distance *d* is then converted to the distance between the beam and the rail surface under the camera *h*. To accomplish this conversion, a calibration method is outlined in Section 4.4.3. A track model is available to convert the measured track deflection to track modulus.

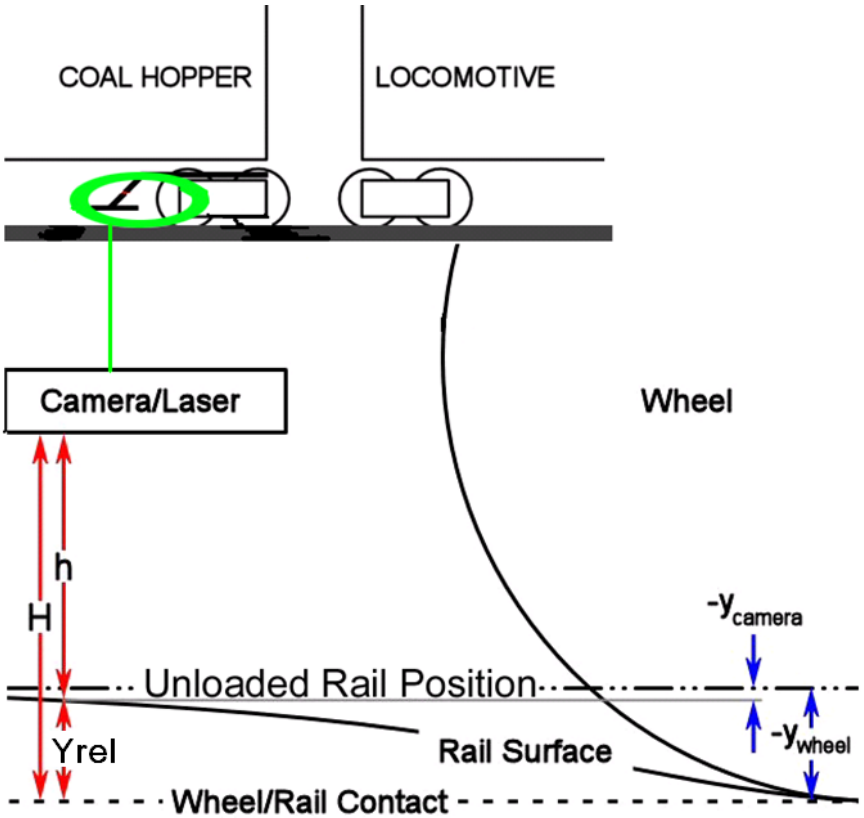

Figure 3-1. Diagram of Measurement Principle

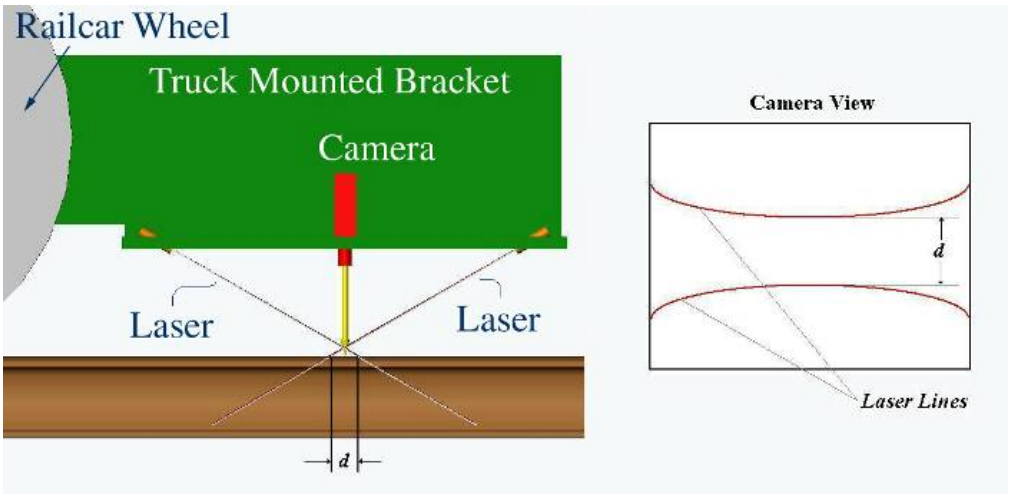

Figure 3-2. Camera/Laser System

Figure 3-1 illustrates that the fixed distance between the wheel-rail contact point and sensor, *H*, relates the relative rail displacement, Yrel, to the measured height of the sensor above the rail surface, *h*. Here, y_{camera} is the deflection of the rail at the location underneath the camera/lasers, and y_{wheel} is the deflection of the rail at the wheel-rail contact point. The deflections are negative in value because the positive axis is defined upwards.

The sensor system measures the distance between the camera image plane and the rail surface, *h*. Then, the displacement of the rail surface with respect to the wheel-rail contact plane, Yrel (Figure 3-1) can be found. The method and mathematics to transform the distance between the laser lines, *d*, to a Yrel measurement is fully described in Section 4.4.3. The displacement, Yrel, can then be related to the absolute rail deflection of the wheel-rail contact point (with respect to the unloaded rail), y_{wheel} (Figure 3-1) by using the Winkler model.

A mathematical model relates the measured distance between the laser lines to the track modulus. The rail deflection measured by the sensor is dependent on the four wheel loads. The sensor will measure the relative rail displacement between the rail and wheel-rail contact point. This measurement can be made if it is assumed that the instrument beam, truck, and wheels are rigid. With this assumption, the distance between the sensor system and wheel-rail contact point can be assumed constant (*H* is constant). This is a reasonable assumption because the instrument beam, side frame, and wheels are all massive, nearly rigid elements, and these elements do not include the suspension of the rail car. Rotation of the side frame could cause this distance (*H*) to change, but this rotation has been experimentally shown to be insignificant (Norman, 2004).

The sensor reading, which is the measured distance between the lasers, is geometrically related to the height of the sensor above the rail. The sensor in effect measures its height above the rail by measuring the distance between the lasers. As the sensor moves closer or farther from the rail surface, the distance between the lasers changes. A schematic of the sensor is shown in Figure 3-3.

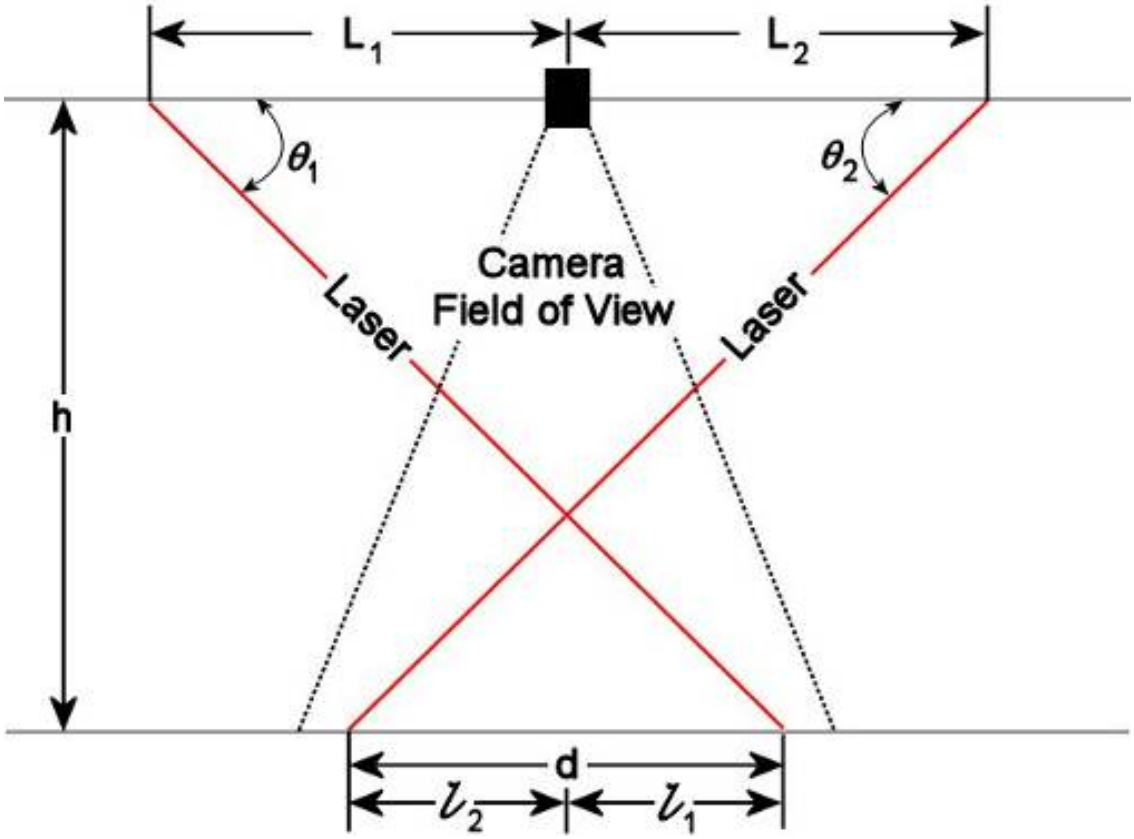

Figure 3-3. Sensor Geometry

From the above figure the following equations can be written:

$$(L_1 + l_1)\tan\theta_1 = h \qquad \text{Equation 3.1-1}$$

$$(L_2 + l_2)\tan\theta_2 = h \qquad \text{Equation 3.1-2}$$

$$d = l_1 + l_2 \qquad \text{Equation 3.1-3}$$

where L_1 and L_2 are the horizontal displacement of the lasers from the camera, θ_1 and θ_2 are the angles between the lasers and the horizontal, l_1 and l_2 are the horizontal distance between the center of the camera and laser-rail intersection, h is the vertical distance between the camera/lasers and the surface of the rail, and d is the distance between the lasers on the rail surface. Solving these equations results in:

$$d = \frac{h}{\tan\theta_1} + \frac{h}{\tan\theta_2} - (L_1 + L_2) \qquad \text{Equation 3.1-4}$$

Combining Equation 3.1-1 with Equation 3.1-4, a sensor reading can be calculated for a value of track relative deflection.

Combining this information with the track model (e.g., Winkler model), the sensor reading d can be related to the track modulus u. On softer track, the rail will rise relative to the wheel-rail contact point, and the laser lines as observed by the camera will move closer together. Conversely, the distance between the lasers will be large for stiffer track.

3.1.2 The Relation between Yrel and Modulus (Winkler Model)

Figure 3-4 shows the rail deflection from multiple loaded axles.

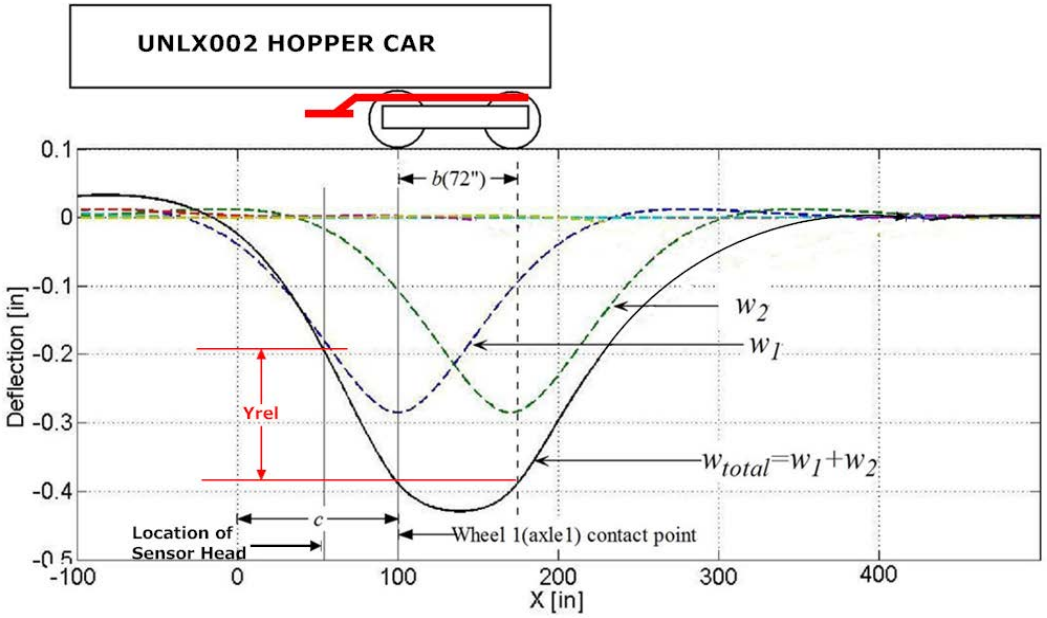

Figure 3-4. Superposition of the Deflections from Two Loads

In Figure 3-4, assuming the loads of wheel 1 (the left wheel) and wheel 2 (the right wheel) are the same (P), w_1 is the deflection of the rail attributed to wheel 1, and w_2 is the deflection of the rail attributed to wheel 2. The total rail deflection is the superposition of w_1 and w_2.

From the Winkler model,

$$w_1(x) = -\frac{P\beta_1}{2u(c)} e^{-\beta_1|x-c|}\left[\cos\left(\beta_1|x-c|\right)+\sin\left(\beta_1|x-c|\right)\right] \qquad \text{Equation 3.1-5}$$

where:

$$\beta_1 = \left(\frac{u(c)}{4EI}\right)^{\frac{1}{4}}$$

when: E is the modulus of elasticity of the rail

I is the moment of inertia of the rail

x is the longitudinal distance along the rail

c is the position of wheel one in the x coordinate (see Figure 3-4)

and $$w_2(x) = -\frac{P\beta_2}{2u(c+b)} e^{-\beta_2|x-c-b|}\left[\cos\left(\beta_2|x-c-b|\right)+\sin\left(\beta_2|x-c-b|\right)\right]$$ Equation 3.1-6

where: $$\beta_2 = \left(\frac{u(c+b)}{4EI}\right)^{\frac{1}{4}}$$

when: *b* is the distance between the two wheel axles (72 in)

(c+b) indicates the position of wheel two in the *x* coordinates

The total deflection of the rail is the superposition of the two expressions which is:

$$w_{total}(x) = w_1(x) + w_2(x)$$

Then, the total deflection at the wheel/rail contact point of wheel 1 is:

$$w_{total}(x)\big|_{x=c} = w_1(c) + w_2(c) = -\frac{P\beta_1}{2u(c)} - \frac{P\beta_2}{2u(c+b)} e^{-\beta_2 b}\left[\cos(\beta_2 b)+\sin(\beta_2 b)\right]$$ Equation 3.1-7

And the deflection of the rail under the sensor head which is 4 ft away from wheel 1 is:

$$w_{camera}(x)\big|_{x=c-a} = w_1(c-a) + w_2(c-a)$$
$$= -\frac{P\beta_1}{2u(c)} e^{-\beta_2 \cdot a}\left[\cos(\beta_2 a)+\sin(\beta_2 a)\right] - \frac{P\beta_2}{2u(c+b)} e^{-\beta_2\cdot(a+b)}\left[\cos(\beta_2(a+b))+\sin(\beta_2(a+b))\right]$$

Then, $$Yrel = w_{total}(c) - w_{camera}(c-a)$$ Equation 3.1-8

Assuming the track is absolutely uniform (i.e., *u* is a constant), then:

$$\beta_1 = \beta_2 = \beta = \left(\frac{u}{4EI}\right)^{\frac{1}{4}}$$

Therefore,

$$Yrel = w_{total}(c) - w_{camera}(c-a)$$
$$= -\frac{P\beta}{2u}\{1 + e^{-\beta\cdot b}\left[\cos(\beta b)+\sin(\beta b)\right]$$ Equation 3.1-9
$$- e^{-\beta\cdot a}\left[\cos(\beta a)+\sin(\beta a)\right] - e^{-\beta\cdot(a+b)}\left[\cos(\beta(a+b))+\sin(\beta(a+b))\right]\}$$

The result of Equation 3.1-9 is shown in Figure 3-5. In this model, 132 lb rail was chosen (I = 87.9 in^4); E is set to be 30,000,000 psi; the load on each wheel is 32,500 lb; and the distance

between the two axles is 6 ft. The typical values of modulus for various main-line track conditions (Kerr, 2003) are listed in Table 3-1 along with the corresponding Yrel value.

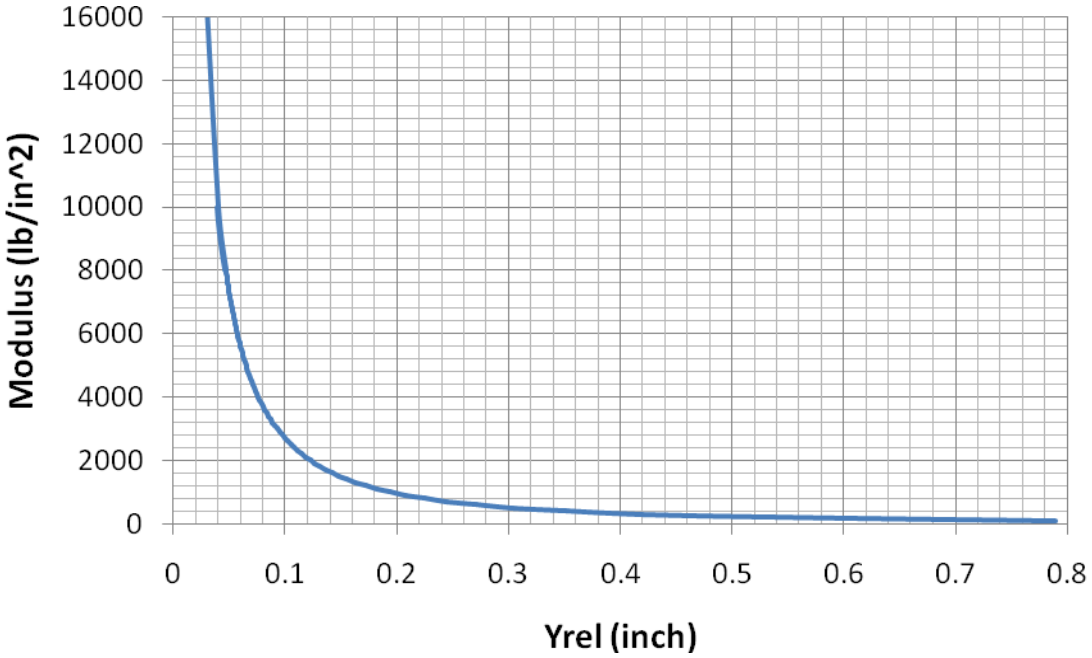

Figure 3-5. Relation between Yrel and Modulus (Winkler model)

Table 3-1. Modulus and Yrel for Typical Track Conditions

Track Condition Description	Modulus (psi)	Yrel (in)
Wood-tie track, after tamping	1,000	0.2
Wood-tie track, compacted by traffic	3,000	0.095
Concrete-tie track, compacted by traffic	6,000	0.058
Wood-tie track, frozen ballast, and subgrade	9,000	0.044

The relation between the rail deflections at the wheel/rail contact point and relative deflection (Yrel) is shown in Figure 3-6. This nonlinear relation is based on the Winkler model and superposition. For relatively small deflections (0~0.2 in), Yrel is approximately 60 percent of the total deflection (deflection at the wheel/rail contact point).

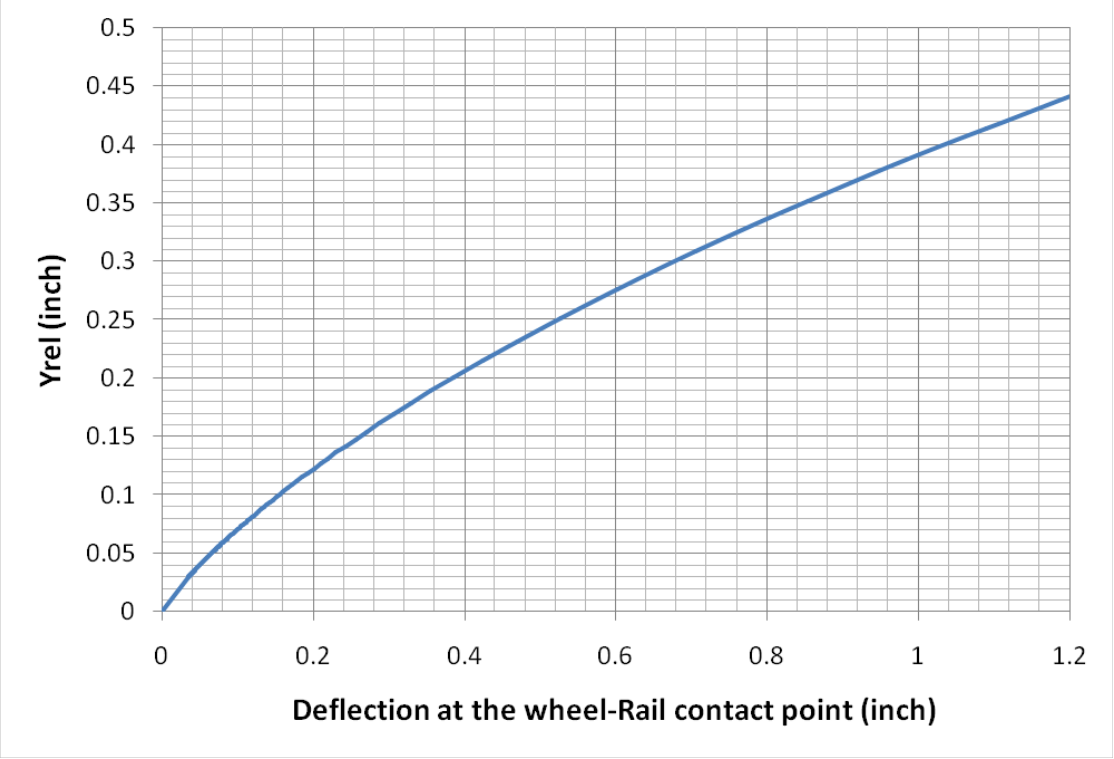

Figure 3-6. Relation between the Total Deflection and Yrel (Winkler model)

3.2 Relationship to Existing Profile Variations

The measurement of relative deflection (Y_{rel}) uses the wheel/rail contact line as a reference as shown in Figure 3-1. The measurement assumes the unloaded rail is perfectly straight. However, if the rail has a significant pre-existing geometry variation over a length comparable to the 4 ft between the measurement point and wheel/rail contact point, the system's measurement will be affected. Large vertical "dips" that occur over a short length of track affect the measurement result.

The relationship between modulus and geometry is complex. In real track, areas of geometry variations often correlate with areas of modulus variations and vice versa. A case study was chosen to investigate this relationship. Figure 3-7 shows a section of track where there is a significant geometry variation and a significant modulus variation. Measurements at the site indicated that the unloaded rail drops by 0.5 in over a length of approximately 16 ft. A geometry variation of this shape is significant and easily visible. The light-colored ballast seen at this site also suggests tie "pumping" and low track stiffness.

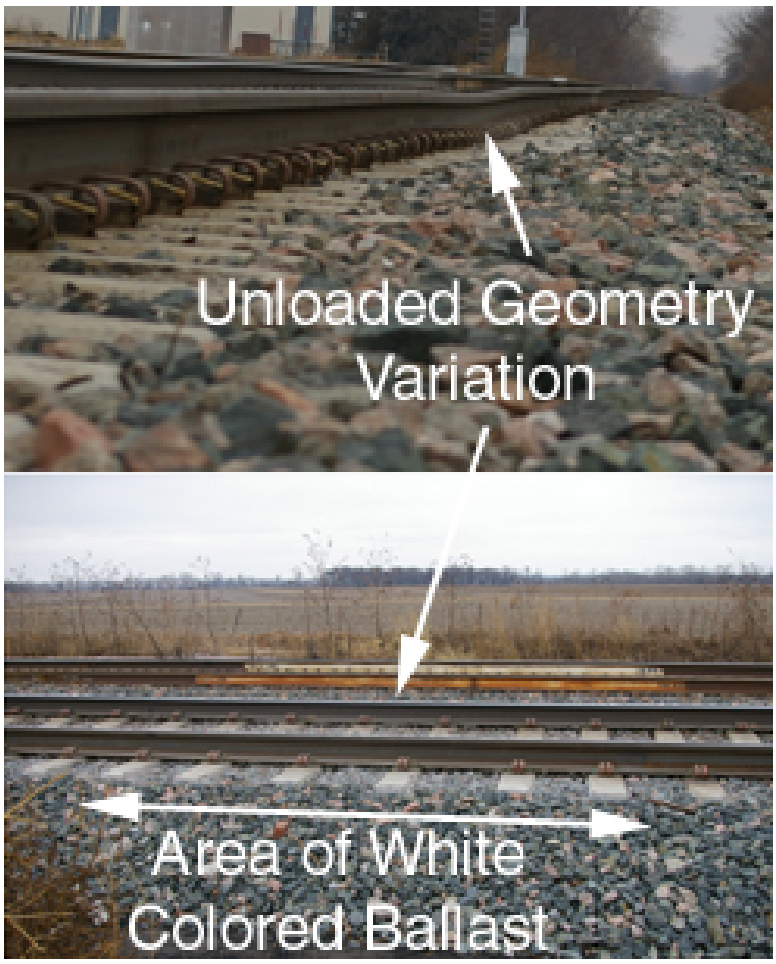

Figure 3-7. An Example Site with Both Significant Unloaded Geometry and Low Track Stiffness

Relative rail deflection (Yrel) from the measurement system at this site is 1.1 in. Simulations, based on the Winkler model, have been conducted to quantify the effects of track geometry on the measurement of relative deflection.

Figure 3-8 shows an example simulation result. In this simulation, a section of track has both geometry and modulus variations. The unloaded track geometry is described in the top subplot in Figure 3-8. It has a maximum "dip" of 0.5 inch in depth, and it occurs over 200 in (between 100 and 300 in) of track.

In the simulation, it was assumed that the modulus over this section of track varies as a cubic curve with a minimum at the center of the geometry variation (the middle subplot in Figure 3-8). The bottom subplot in Figure 3-8 shows the Yrel measurement for this site. Here, the "total" measurement replicates the value of 1.1 in, as it did in the real measurement when the measurement system passed over the location shown in Figure 3-7. To create this value, it was found that the modulus for this location had to drop from 3,000 psi (assumed as a reasonable value for "normal" track) to 800 psi in addition to the unloaded geometry profile. This measurement is then broken into two "elements"—a modulus element and a geometry element. The geometry element is the measurement that would be made if the same unloaded geometry

(top subplot) existed on a perfectly rigid track. The modulus element in the remaining portion is the total measurement minus the geometry element.

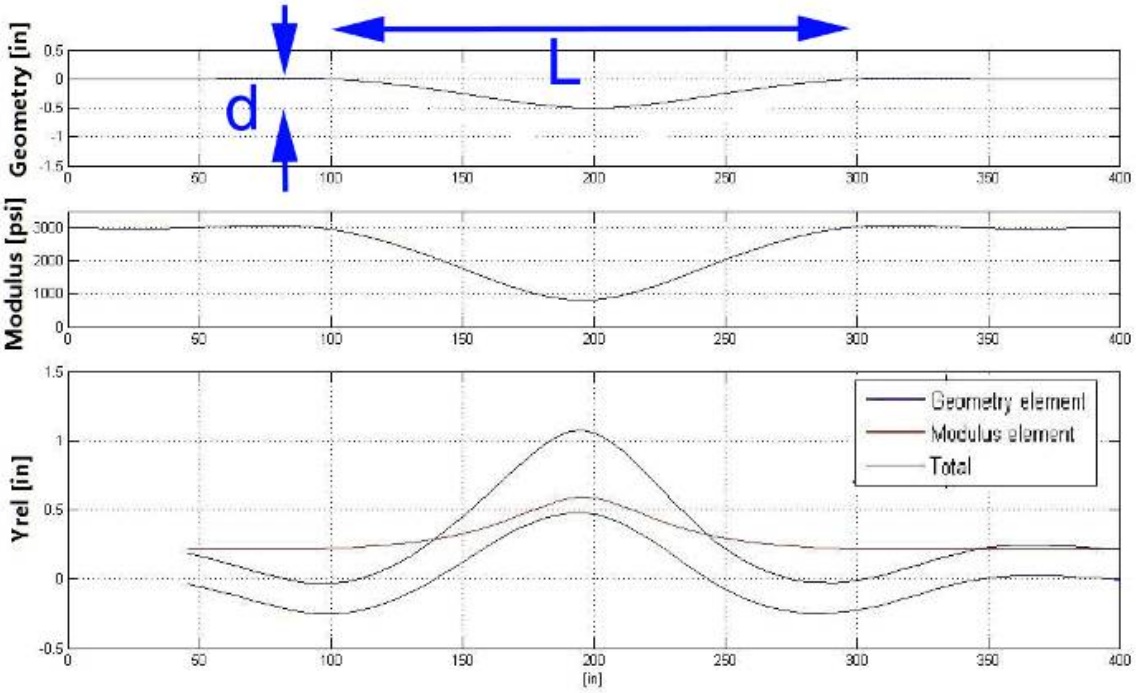

Figure 3-8. Simulation on the Effects of Track Geometry

It can be seen that in this case the contribution of geometry (the geometry element) is about equal to the contribution of modulus (the modulus element). However, both are required to make the measurement large.

Now, the simulation can be used to study the relative contribution of geometry and modulus as the length of the geometry variation (L) and the depth of the geometry (d) vary. The simulation result is shown in Figure 3-9.

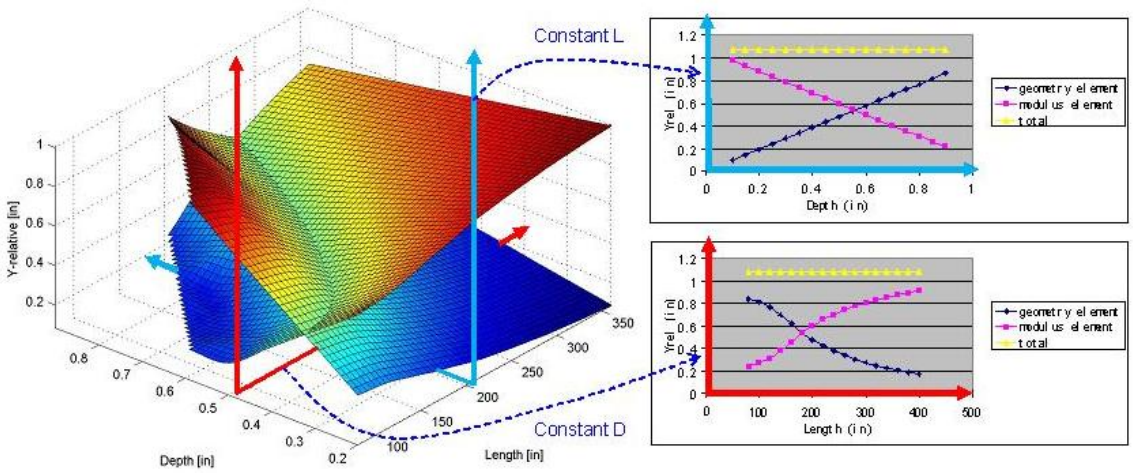

Figure 3-9. Effects of Unloaded Geometry of Various Length (L) and Depth (d)

It can be seen in Figure 3-9 that there is a complex relationship between modulus and geometry and that the effects vary depending on the length (L) and depth (d) of the geometry variation. The three-dimensional plot on the left shows the relative size of the geometry element and the modulus element. It can be seen that there is a curve where the elements are equal in magnitude.

The two graphs on the right show two cross sections of these surfaces. The top right graph shows the effects of variations in the length of the geometry defect (L) at a constant depth (d = 0.5 in). The bottom right graph shows the effects of variations in the depth of the geometry defect (d) at a constant length (L = 200 in).

Again, the conclusions that can be drawn from these simulations are that 1) only large vertical geometry defects occurring over a short distance significantly contribute to the Yrel measurement, and 2) both geometry and modulus problems are generally present where very large Yrel values are measured.

3.3 End-Chord Offset

As seen in the simulation and analysis in the previous section, track geometry can, in some cases, affect the output of the system in terms of measuring rail deflection. To eliminate the effects of track geometry variation and to get the real rail deflection results, track geometry profile data from track geometry measurement vehicles was introduced into the system.

A track geometry vehicle is a rail vehicle used for nondestructive diagnosis of railroad tracks. It measures various parameters including position, curvature, and alignment of the track as it passes by, as well as smoothness and the cross level of the two rails, etc. The space curve channel of the geometry car uses multiple high-precision accelerometers onboard to produce the rail profile that includes effects of relatively long wavelength variations.

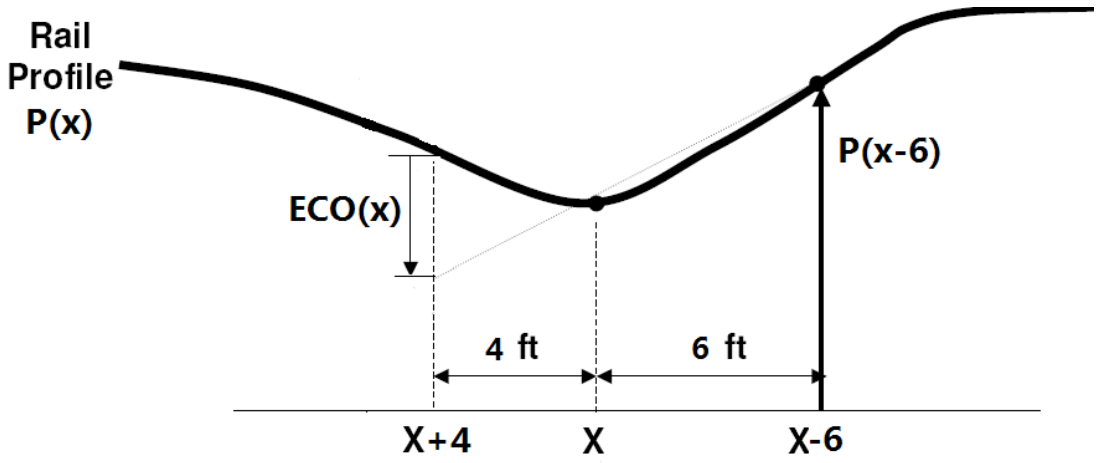

Figure 3-10. 10-Foot ECO Calculation from Rail Profile

As shown in Figure 3-10, *P(x)* is the rail profile from the space curve channel of the track geometry data. The longitudinal position of the track is defined as *x* (unit: foot). ECO*(x)* is the 10-foot end-chord offset (ECO) when the leading wheel's longitudinal position is *x* (ECO is positive if the string is above the rail.) Here, the 6- and 4-foot lengths were chosen because they are the distance between the two wheel axles and the distance from the sensor head to the inboard wheel axle, respectively.

From the geometry relation in Figure 3-10:

$$\frac{P(x-6)-P(x)}{P(x)-[P(x+4)+ECO(x)]}=\frac{6}{4} \qquad \text{Equation 3.3-1}$$

Therefore, $$ECO(x)=\frac{2}{3}\cdot[P(x)-P(x-6)]+P(x)-P(x+4) \qquad \text{Equation 3.3-2}$$

3.4 Relative Track Deflection

Figure 3-11 shows how this calculation can be made. In Figure 3-11(a), a schematic representation is shown. Here, the unloaded rail is shown along with the loaded profile. For the calculation of ECO, it is assumed that the leading and trailing wheel track the same profile. The actual shape of the rail is shown as the loaded rail. Finally, the 10-foot chord is shown with the graphical definitions of ECO, Yrel, and relative deflection.

Figure 3-11(b) is calculated from actual rail measurements made by the test car. *P(x)* is the vertical position of the inboard wheel/rail contact point when the inboard wheel's longitudinal position is *x*. *P(x-6)* is the vertical position of the inboard wheel/rail contact point when the inboard wheel's longitudinal position is *x-6*. If it is assumed the two wheels always have the same space curve, then *P(x-6)* is the vertical position of the trailing wheel/rail contact point when the inboard wheel's longitudinal position is *x*. *P4(x)* is the rail's vertical position 4 ft ahead of the inboard wheel when the inboard wheels longitudinal position is *x*.

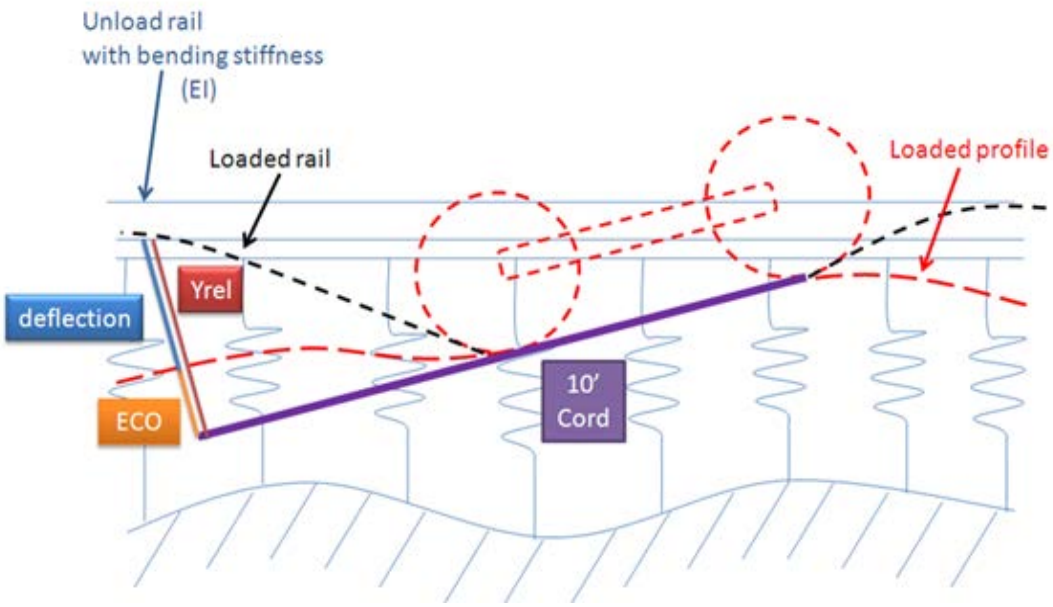

a) Deflection Schematic

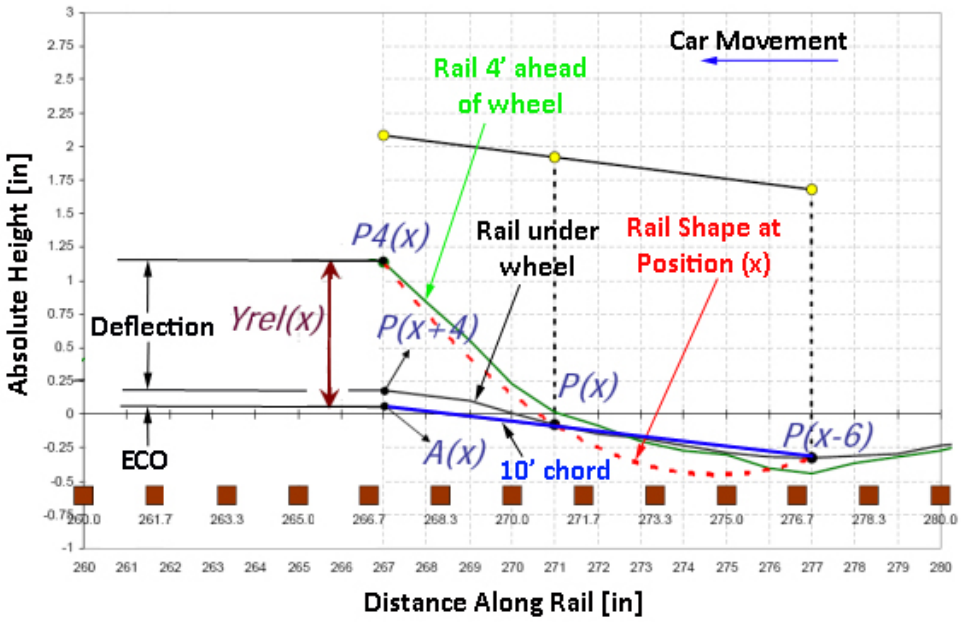

b) Deflection for Actual Measurements

Figure 3-11. Deflection Calculation

Let *A(x)=P4(x)-Yrel(x)*, then from geometry relation in Figure 3-11, we have:

$$\frac{P(x-6)-P(x)}{P(x)-A(x)}=\frac{6}{4}$$

So, $$A(x)=\frac{1}{3}\cdot[5P(x)-2P(x-6)]$$ Equation 3.4-1

Therefore, $$P4(x)=A(x)+Yrel(x)=\frac{1}{3}\cdot[5P(x)-2P(x-6)]+Yrel(x)$$ Equation 3.4-2

The vertical position of the rail at location x+4 may be determined when the inboard axle is at location x. The vertical rail position at the same location may be determined again when the inboard axle is actually at location x+4. Then, the difference between these two measurements (*P4(x)-P(x+4))* may be calculated by:

"Deflection"

$$= P4(x)-P(x+4)$$

$$=\frac{1}{3}\cdot[5P(x)-2P(x-6)]+Yrel(x)-P(x+4)$$

$$=\frac{2}{3}\cdot[P(x)-P(x-6)]+P(x)-P(x+4)+Yrel(x)$$

$$=ECO(x)+Yrel(x)$$

Equation 3.4-3

It should be noted that the so-called "Deflection" calculated above is not the maximum deflection of the rail attributed to the loads. Rather, it is a relative deflection of the rail from partially loaded (when the axle is 4 ft away) to fully loaded (when axle is right at the point).

Therefore, Yrel can be accounted for by two parts. One part is ECO, attributed to the track geometry variations, and the other part is the deflection related to track modulus variations.

4 The UNL Measurement Car

4.1 Early Deployment

During the early years of this project, experiments were conducted on wheel sets and trucks as shown in Figure 4-1. These experiments, which were performed without rolling stock, helped to better understand the load-deflection relation of the wheel/rail interaction.

Figure 4-1. Experiments in Early Deployment

A hopper car was later introduced into the project and a frame was designed, built, and installed on the side frame of the hopper car as shown in Figure 4-2. A few short-distance tests were conducted using this hopper car to help improve the measuring sensors.

Figure 4-2. The Hopper Car Used in Early Deployment

4.2 Caboose

Before the measurement system was upgraded to its autonomous capability, all tests were conducted with onboard crews located in a caboose shown in Figure 4-3. The caboose served as a platform to accommodate the testing personnel. It also hosted the computers and other equipment and provided a power supply to the sensors and other equipment.

Figure 4-3. Exterior and Interior of the Caboose

4.3 Tank Car

After further development, a tank car filled with water was used as the rolling stock carrying the sensor heads as shown in Figure 4-4. The tank car generated the heavy loads needed to create relatively large deflection under the wheels. The tank car was coupled with the caboose during the tests. A number of tests were conducted in this configuration. However, because of the liquidity of the content in the tank car, the dynamic load of the vehicle was distributed more unevenly among the wheels. This kind of imbalance negatively affects the measurement system. Therefore, the system was later upgraded to a refurbished hopper car donated from Union Pacific Railroad (UPRR) and formerly used by FRA in the development of the Gage Restraint Measurement System (FRA GRMS T-6), filled with sand, which is the current testing vehicle in use.

Figure 4-4. The Tank Car Used in Early Stage of the Project

4.4 UNLX002 Autonomous Measurement System

4.4.1 Instrumentation

The measurement system is installed on a refurbished hopper car. The hopper car is filled with sand such that the total weight of the car and sand is approximately 260,000 lb. As shown in Figure 4-5, the system includes two rigid beams attached to the side frames (structural members that connect the axles of a truck) of the hopper car, two sensor heads holding cameras and lasers

at the ends of the rigid beams, a solar panel array, a global positioning system (GPS) antenna on the top of the car and an enclosed box containing the computers, data acquisition (DAQ) boards, and a GPS receiver for onboard image processing and data computation.

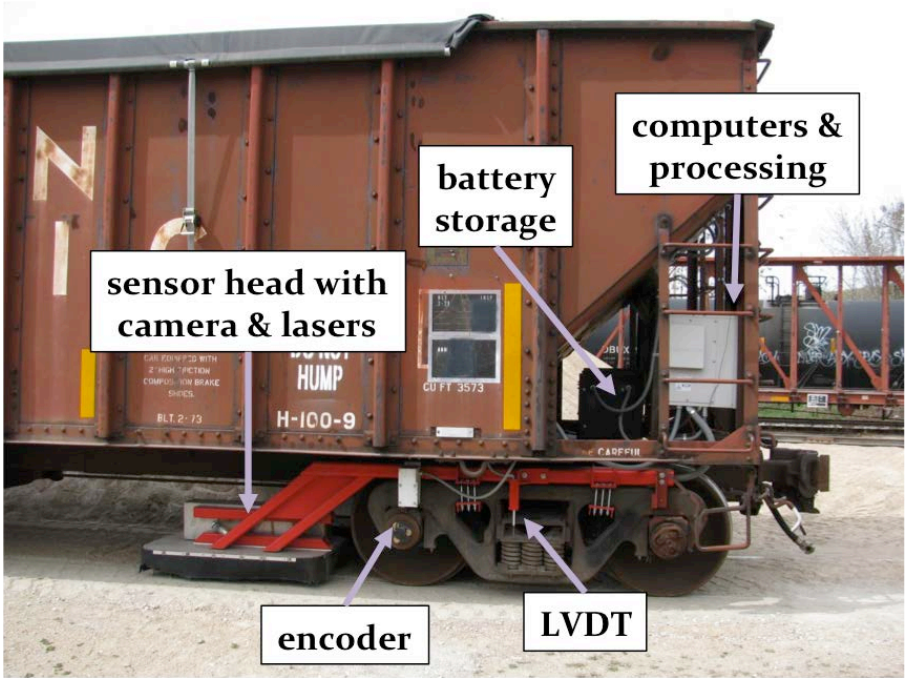

Figure 4-5. System Instrumentation

All of these components will be described in detail in the following sections.

4.4.1.1 Sensor System

The sensor head is attached to highly rigid steel beams that are fastened to the side frames. The beams are bolted to the side frames without modification of the side frames. These beams suspend the sensor heads out in front of the wheel/rail contact point and over the top of rail. Investigations into rigidity have shown that the beams are sufficiently rigid to be considered stationary relative to the side frames (Norman, 2004). Therefore, the measurement will not be affected by the bending or movement of the beams. An actual view of the assembly is shown in Figure 4-6.

Figure 4-6. The Rigid Beam on the Side Frame

A sensor head holds a digital vision system and two line lasers as shown previously in Figure 3-2. The camera and line lasers are rigidly attached to an enclosed sensor assembly, which is mounted at the end of the rigid beam on the side frame. These lasers are projected at an acute angle (~40˚). They cross and create curves (because of the curved profile of the rail head) across the surface of the rail.

The assembly of the sensor head is shown in Figure 4-7. The two laser holders are adjustable to ensure that the lasers project at an appropriate angle. The height of the camera is also adjustable. This ensures that well-proportioned images will be captured.

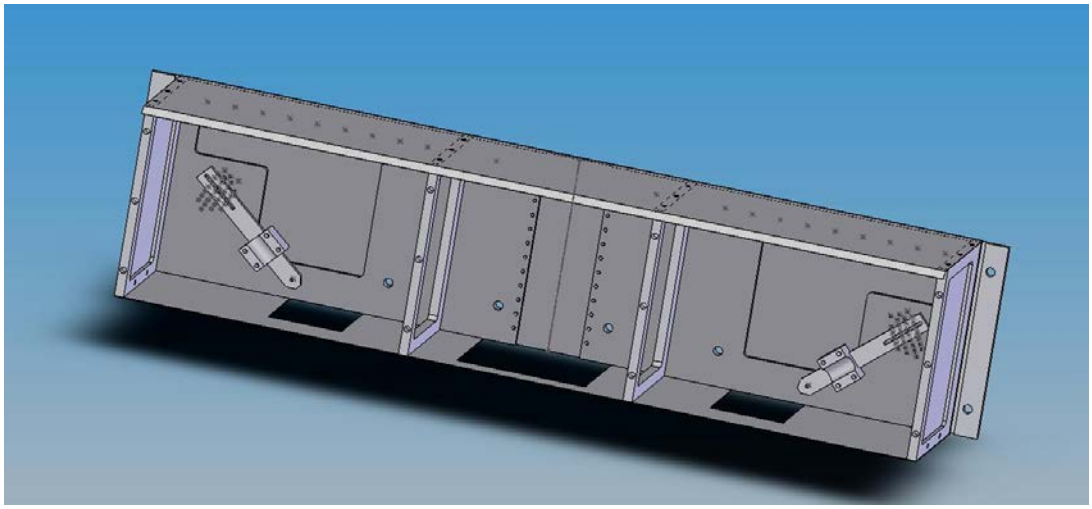

Figure 4-7. Sensor Head Assembly

Ambient light, specifically sunlight, ruins the image of the laser lines across the rail and makes it impossible for the image processing program to distinguish the laser lines. Therefore, a shroud assembly was made to shield the sunlight. The shroud is a light steel frame bolted to the bottom of the rigid beam. Rubber landscaping material is attached along the bottom edge to add further

shading. This material is flexible, making it resistant to rocks and debris, but is also continuously solid making it resistant to wind effects.

A typical sensor image is shown in Figure 4-8. The video image shows the laser beams intersecting the top of the rail. Images are captured and processed in real time to output the distance between the laser lines (*d* in Figure 3-2).

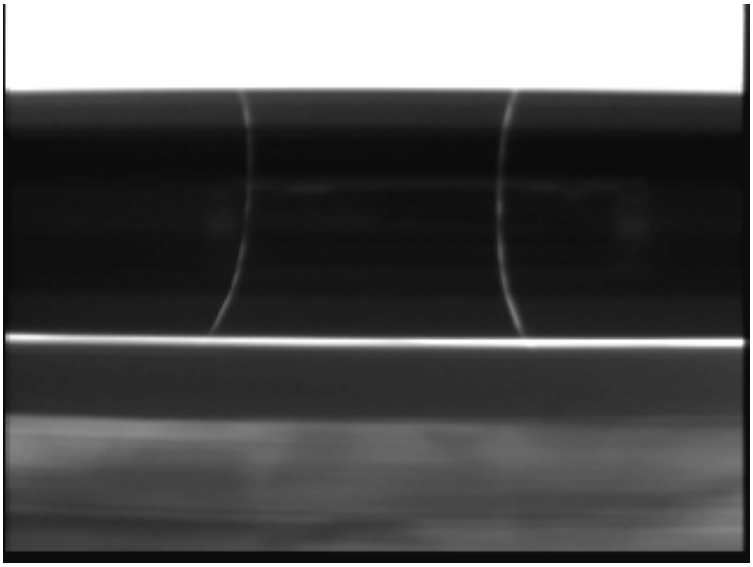

Figure 4-8. Typical Test Image

This measurement is geometrically related to the height of the sensor above the rail (*h* in Figure 3-1). As the sensor moves closer or farther from the rail surface, the distance between the laser lines changes. With the calibration technique, Yrel can be calculated as the systems output. Yrel is the relative displacement between the rail surface under the camera and the wheel/rail contact line. Yrel can then be mathematically related to track stiffness and modulus (Norman, 2004; McVey, 2006; Lu et al., 2007).

The real-time image processing and data management are performed by onboard computers. These computers are installed in enclosed boxes as shown in Figure 4-9. A GPS receiver and two data acquisition boards are also installed in these boxes. All of the cables and wiring for the equipment are routed through flexible conduits. The sealed boxes protect the computers and other electrical equipment from harsh environments.

Figure 4-9. Enclosed Box for Computers

4.4.1.2 GPS and Encoder

The measurement system includes a GPS receiver. The latitude and longitude are reported in real time and recorded in the output data. The GPS data is used to get milepost information by comparing it with Precision Measurement Vehicle (PMV) data and provides accurate coordinates for exception locations.

The GPS receiver used in the system is a NovAtel OEM4 model, which is capable of absolute single-point positioning accuracies of 1.8 meters of Circular Error Probable (CEP) (Geometric Dilution of Precision (GDOP) < 2; no multipath). However, this level of accuracy is only an estimation and may vary widely depending on numerous GPS system biases, environmental conditions, as well as the GPS receiver design and engineering quality.

Because of the GPS error, there may be some stretches in the data in terms of mileposts. An encoder has been introduced into the system to eliminate this stretching problem caused by the GPS error.

4.4.1.3 Power Supply and Management System

Two rugged computers are used to process images in real time and save the data. To reduce power consumption when the testing vehicle is not moving, the whole measurement system enters a “sleeping” mode in which the lasers and cameras are turned off and the computers remain in standby mode. The total power consumption is approximately 50 watts when the system is in full-on testing mode and 10 watts in sleeping mode.

An onboard power supply and management system was developed to make autonomous testing possible. As shown in Figure 4-10, four solar panels installed on the top of the testing vehicle provide the power source for the measurement system. The solar panels are rated at a maximum

of 400 watts. A battery pool consisting of eight deep-cycle marine batteries is used as energy storage and as a buffer to provide stable and consistent power to the system during both day and night. The eight batteries have a total capacity of 400 Amp-hours, which can supply 4 days of continuous testing or 20 days of "sleep" mode without inputs from the solar panels. The batteries are enclosed in the black box as shown in Figure 4-10 along with a solar panel voltage regulator, which manages the battery recharge process and prevents the batteries from being overcharged. Inside the battery box, two watt meters were also installed to provide information about the measurement system's energy usage and energy input from the solar panels.

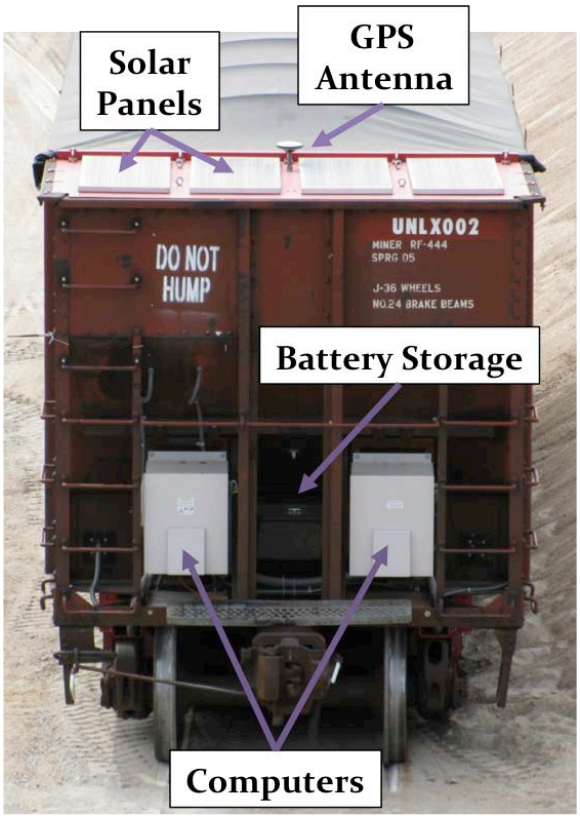

Figure 4-10. Power Supply System

The power supply system has proven to be sufficient and reliable during autonomous tests in several tests over many years under various conditions. In these tests, the batteries were returned fully charged after the 6-day, 1300-mile-long journey.

4.4.1.4 Remote Supervision and Data Downloading

The voltage across the batteries, the current input from the solar panels, and the ambient temperature are monitored by a computer in the white boxes shown in Figure 4-10. This information can be recorded and sent back to a server on the Internet through wireless communication, which enables the power supply system to be remotely monitored.

The data logged and uploaded in real time from the computer onboard to a remote server through the Internet during the test in April 2008 is displayed in Figure 4-11. As shown by the current and voltage traces in this figure, the batteries were charged during the daytime. The output of the solar panels was measured as high as 150 watts. The highest output from the solar panels

usually occurred in the morning to compensate for the power consumption during the nights. While in sleeping mode, the batteries can be fully charged before noon and the voltage of the batteries will remain constant for the rest of the day.

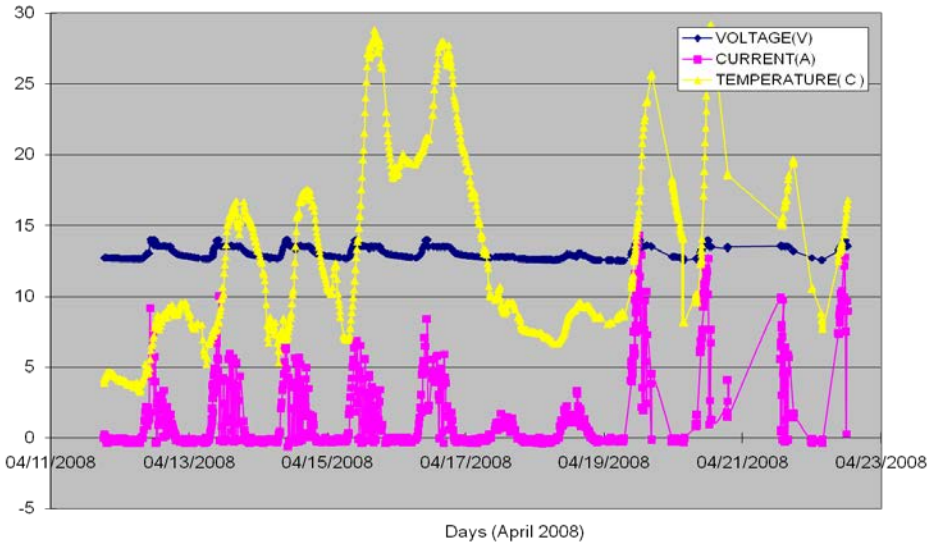

Figure 4-11. Power Supply System Monitoring Information in the April 2008 Test

4.4.1.5 Testing Results Database

The testing vehicle has been tested on thousands of miles of track. As a result, huge amounts of data have been produced from these tests. Therefore, a database was set up to organize and manipulate this data. A Web site was created to search through the database and to develop plots. A screenshot from this Web site is shown in Figure 4-12. The Web site can also produce lists of exception locations from the database and plot them on maps as shown in Figure 4-13.

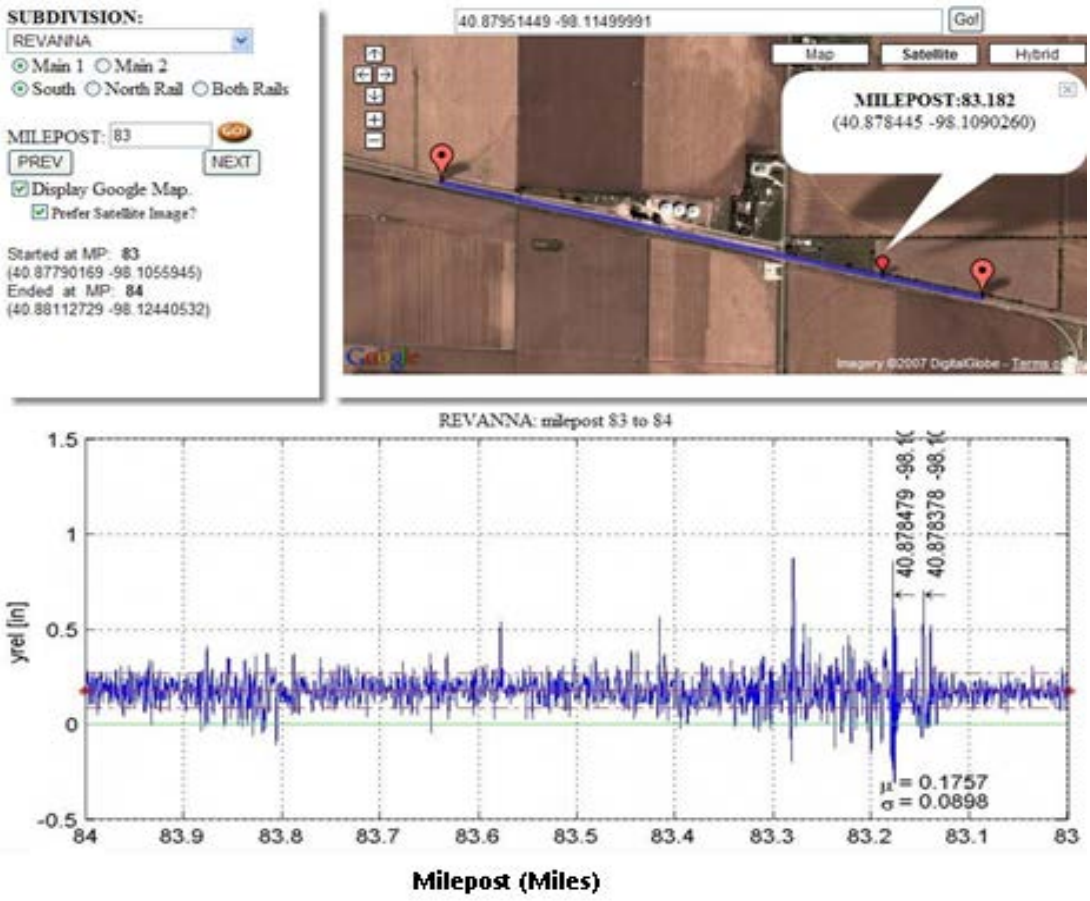

Figure 4-12. Database Web Site Screenshot

	MILEPOST	Yrel-mean	sigma-ratio	sigma	mean	Latitude	Longitude	Track	Rail	Direction
1	58.812	1.210	14.010	0.090	0.070	41.33039474	-102.13791656	2	NORTH	SM-NP
2	142.437	1.210	8.870	0.140	0.170	41.81102753	-103.59835815	1	NORTH	NP-SM
3	114.192	1.180	13.940	0.080	0.160	41.68216324	-103.09439087	1	SOUTH	NP-SM
4	58.813	1.180	12.070	0.100	0.070	41.33039856	-102.13793945	2	SOUTH	SM-NP
5	115.442	1.180	10.450	0.110	0.150	41.68928528	-103.11663055	1	SOUTH	NP-SM
6	115.124	1.160	7.200	0.160	0.200	41.68748474	-103.11096191	1	NORTH	NP-SM
7	105.108	1.140	9.580	0.120	0.090	41.62158585	-102.93901825	2	NORTH	SM-NP
8	115.452	1.100	9.370	0.120	0.120	41.68927765	-103.11681366	2	NORTH	SM-NP
9	93.489	1.060	19.190	0.060	0.060	41.55511475	-102.73339844	2	SOUTH	SM-NP
10	158.126	1.030	12.400	0.080	0.130	41.93171692	-103.86266327	1	SOUTH	NP-SM
11	94.694	1.030	25.110	0.040	0.090	41.56366730	-102.75334930	1	SOUTH	NP-SM
12	105.106	1.020	8.060	0.130	0.060	41.62157822	-102.93900299	2	SOUTH	SM-NP
13	-0.110	0.980	13.720	0.070	0.100	41.16049194	-101.07314301	2	NORTH	SM-NP
14	56.286	0.940	8.520	0.110	0.100	41.31824875	-102.09281158	2	SOUTH	SM-NP
15	137.961	0.930	10.640	0.090	0.130	41.78478622	-103.51911163	2	NORTH	SM-NP
16	123.100	0.920	15.840	0.060	0.140	41.71881866	-103.25904083	1	NORTH	NP-SM
17	142.414	0.910	10.330	0.090	0.150	41.81090164	-103.59796143	1	NORTH	NP-SM
18	147.296	0.910	10.330	0.090	0.140	41.84682465	-103.67591095	1	NORTH	NP-SM
19	145.501	0.900	6.290	0.140	0.150	41.82800293	-103.65322113	2	NORTH	NP-SM
20	55.307	0.880	6.840	0.130	0.100	41.31840134	-102.07398224	2	SOUTH	SM-NP

GOOGLE MAP

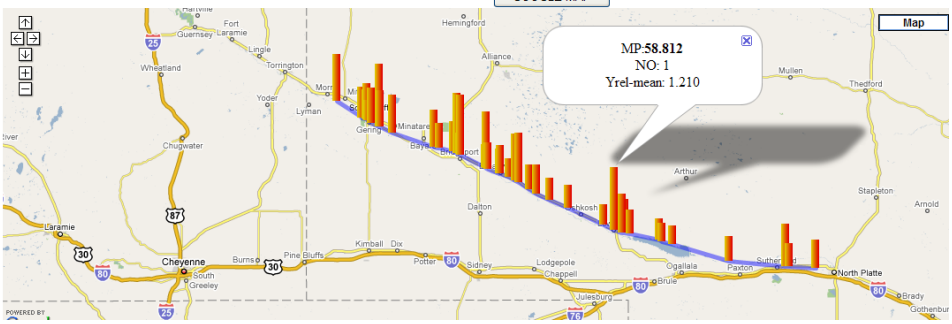

Figure 4-13. Exception Locations List from the Web Site

4.4.2 Real-Time Image Processing

In the typical image captured during the test shown in Figure 4-8, the laser lines are easily identifiable on the top of the rail. The image processing program scans through all the pixels on each horizontal line of the image and locates the peaks of the pixel intensities, which represent the locations of the laser lines. Subsequently, the laser lines can be reproduced as shown in Figure 4-14. After scanning through the image and obtaining the valid points on each laser line, some points may be considered as valid but out of the curve because of the reflection on the rail surface or some distractions captured in the images as shown in Figure 4-15. These outliers are filtered out, and cubic curves are applied to fit the remaining valid points.

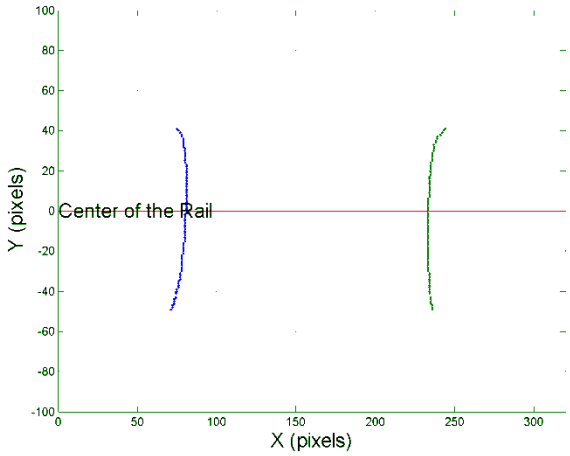

Figure 4-14. Reproduced Laser Curves

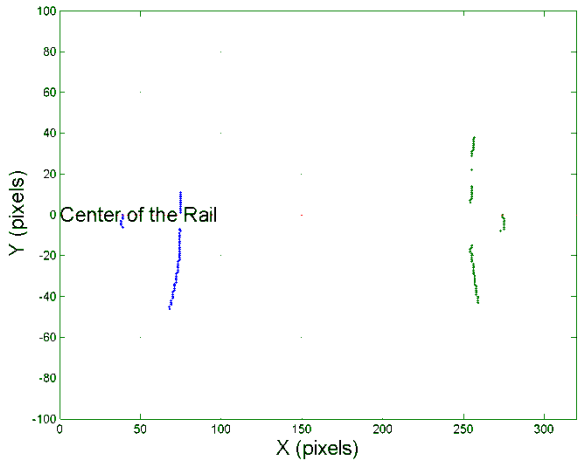

Figure 4-15. An Imperfect Image Example

4.4.3 Calibration Approach and Procedure

As shown previously in Figure 3-1, Yrel is the relative displacement between the rail surface under the sensor and the wheel/rail contact line. Yrel is the measurement systems output.

The system processes images in real time and obtains the number of pixels between the two laser lines in the images. This number of pixels is the system's direct measurement. To convert this number of pixels into the value of Yrel in inches, a calibration must be conducted.

The purpose of the calibration procedure is to obtain the relation between the system's direct measurement (*n*, the number of pixels between the laser lines in images) and the expected output (Yrel).

Figure 4-16 shows how to convert the number of pixels into the actual distance in inches. An image of a ruler on top of the rail was captured. The 6-inch ruler corresponds to 208 pixels in the captured image. Therefore, 1 inch in the image corresponds to 208/6 = 34.67 pixels (i.e., if the number of pixels between the two lines is *n*, the actual distance *d* is *n*/34.67 in).

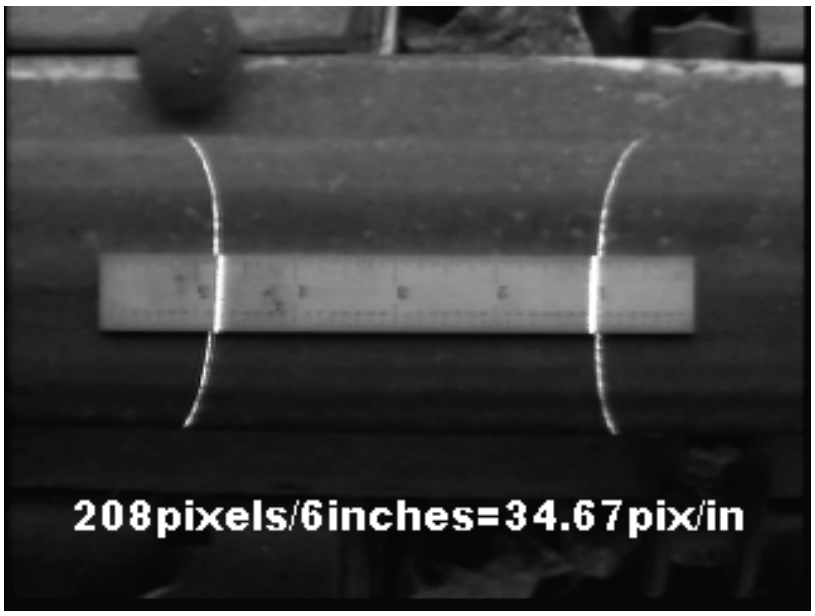

Figure 4-16. Converting Number of Pixels into Distance in Inches

Now the problem consists of finding the relation between *d* and *Yrel*. To do this, imagine a situation where a single measurement of Yrel (that will be called *Yrel**) can be taken that corresponds to a known value of *d* (that will be called *d**). Here, the "*" indicates one specific incidence of *Yrel* and *d*. Therefore, if at one moment, *Yrel = Yrel** and *d = d** are known, and the ratio of *ΔYrel* and *Δd* ($R = \frac{\Delta Yrel}{\Delta d}$) is also known then, the relationship between *ΔYrel* and *Δd* may be determined as follows:

First, *ΔYrel* and *Δd* may be represented as:

*ΔYrel = Yrel - Yrel**

*Δd = d - d**

Then it follows that,

$$Yrel = Yrel^* + \Delta Yrel = Yrel^* + R \cdot \Delta d = Yrel^* + R \cdot (d - d^*) \qquad \text{Equation 4.4-1}$$

Therefore, the calibration problem consisted of finding *Yrel**, *d**, and *R*, which involves the following steps.

4.4.3.1 Finding the Ratio of Δ*d* and *ΔYrel* (*R*)

A special plate was fabricated for this calibration procedure. The device consists of seven steps as shown in Figure 4-17 and Figure 4-18. The lowest step is one-fourth-inch high and the other six steps are one-eighth-inch high. When doing the calibration, this plate is placed on top of the rail under the camera, and the two laser lines project onto the plate. Therefore, an image similar to Figure 4-19 is captured by the camera.

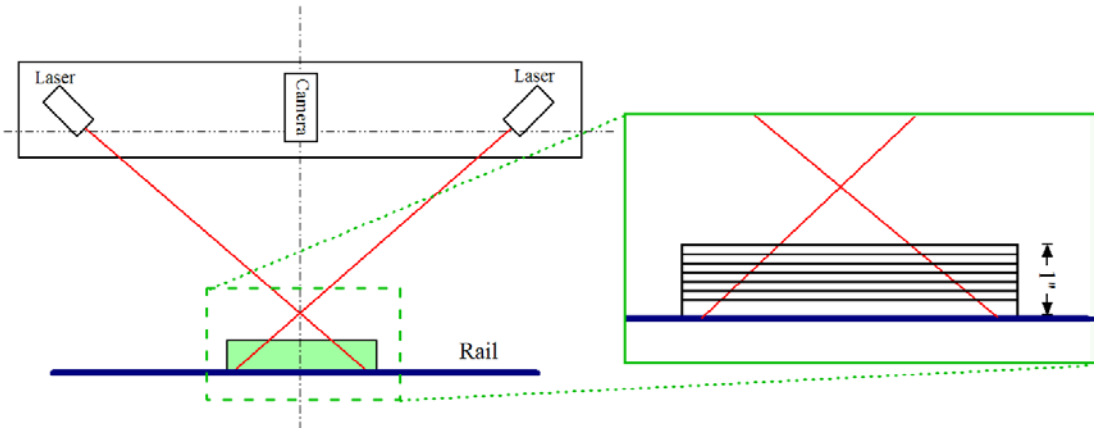

Figure 4-17. Calibration Plate on the Top of the Rail

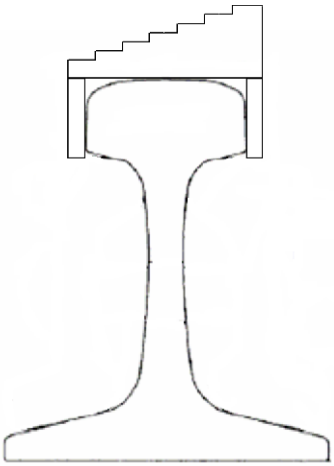

Figure 4-18. Calibration Plate on Top of the Rail (side view)

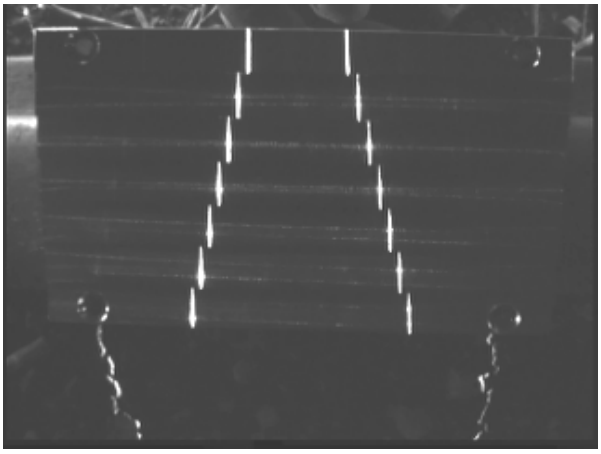

Figure 4-19. Captured Image of the Calibration Plate

The image in Figure 4-19 is then processed. The distances between the laser lines on each step of the plate were obtained and plotted in Figure 4-20 with respect to the step's height above the

rail. As shown in Figure 4-20, a linear line fits the data points very well ($R^2 = 0.9988$). From the line fit, one pixel in the image represents $\frac{1}{84.857} = 0.01178$ in of *ΔYrel.*

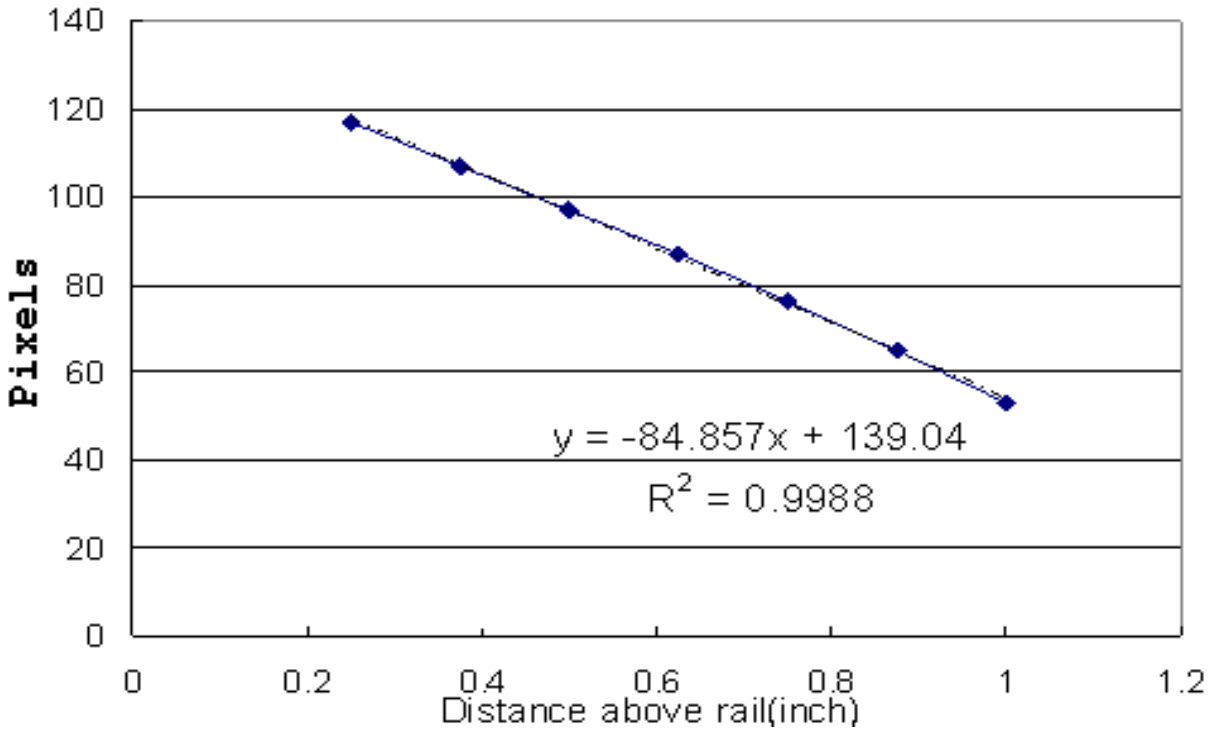

Figure 4-20. Calibration Results

This result verifies the calibration results very well. On the basis of the geometric relation, one pixel in the image was calculated to represent 0.01176 in of Yrel. The difference between the results from the two different methods is (0.01178 – 0.01176)/0.01176 = 0.17%, which is negligible.

This difference may be attributed to many factors including the limited resolution of the captured images, the wide laser lines in the images, measurement error during the calibrations, etc. Some of these factors will be discussed in detail in Section 4.4.4.

4.4.3.2 Finding *Yrel** and *d**

Again, the goal of calibration is to find a single instance where Yrel is known, and the corresponding value of *d* is known. We are calling these known values *Yrel** and *d**. This section describes how these known values can be obtained through measurement.

After calculating the ratio of *Δd* and *ΔYrel*, all that is needed is to find a reference point where both the relative deflection (Yrel) and the distance between the laser lines (*d*) may be determined.

Assuming that a section of track is perfectly uniform and the modulus over the section is a constant, the deflection of the rail under the axles will be identical over the entire section. If a train moves over this section at a very slow speed, the rail deflection at one fixed point as a

function of time can be mapped from the time domain into the space domain so that the static rail profile under the axles can be obtained. The dynamic load factor can be ignored because the train speed is slow.

Figure 4-21 demonstrates the setup for capturing the rail deflection with a video camera. A sticker is placed on the side of the rail head as a marker, while a video camera away from the track captures this sticker in its view. Another marker is placed on the ballast 4 ft away from the sticker.

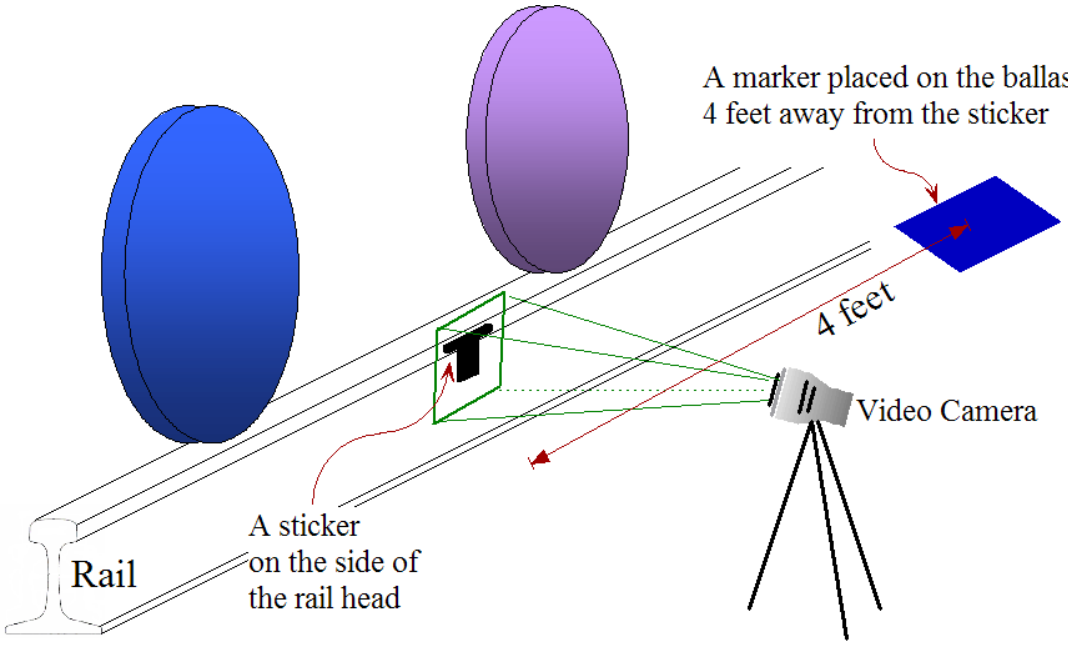

Figure 4-21. Capturing the Rail Deflection with a Video Camera

The measurement vehicle is pulled at a constant speed and passes by the video camera. Meanwhile, the video camera captures and saves the video for postprocessing. An image from the captured video is demonstrated in Figure 4-22. As the wheels of the measurement vehicle move closer to the position of the marker, the deflection of the rail increases and the marker in the camera image goes down. When the wheels move away from the marker, the marker goes up in the video.

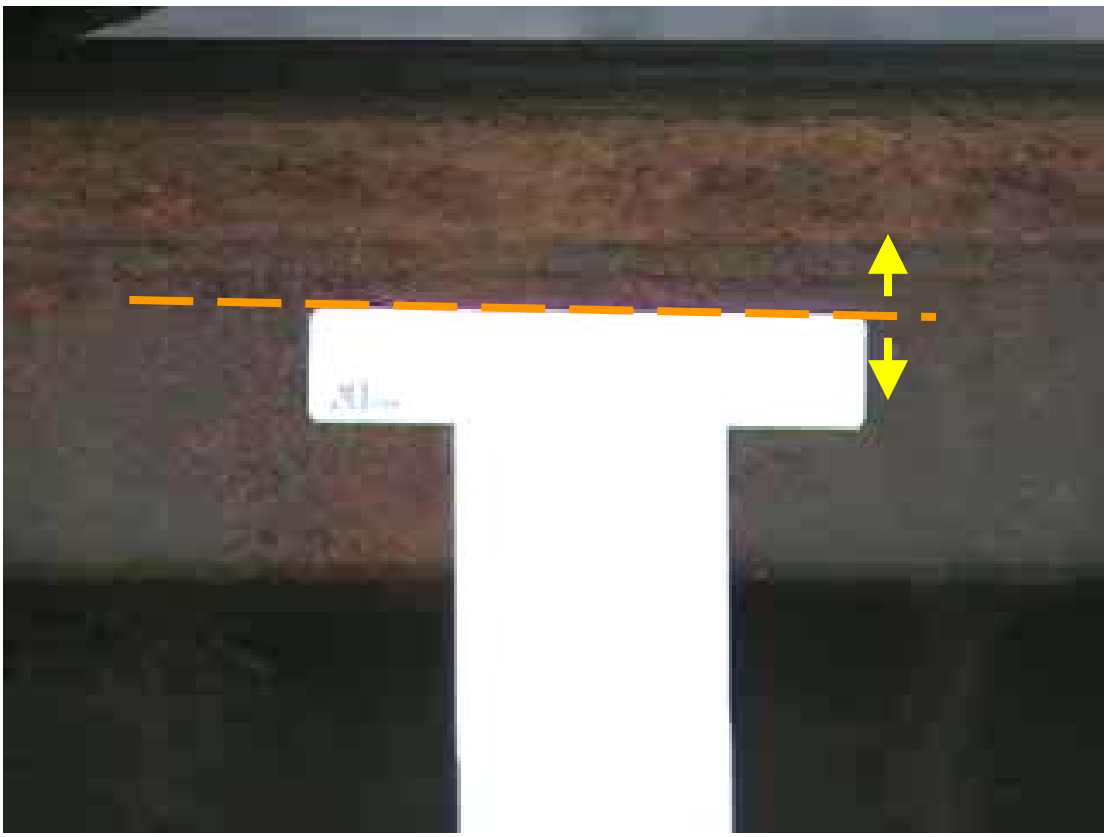

Figure 4-22. Captured Video Showing the Rail Deflection

An image processing program was developed to process the video and determine the vertical position of the top edge of the marker as shown in Figure 4-22. Assuming the deflection of the rail is zero when the locomotive and measurement vehicle are far away from the marker, the vertical position of the marker in the video can then be converted into the actual deflection of the rail, which is plotted in Figure 4-23. Therefore, *Yrel**, the vertical height difference between the rail surface under the camera and the wheel/rail contact plane, is shown in Figure 4-23. From this calibration data, *Yrel** is 0.045 in.

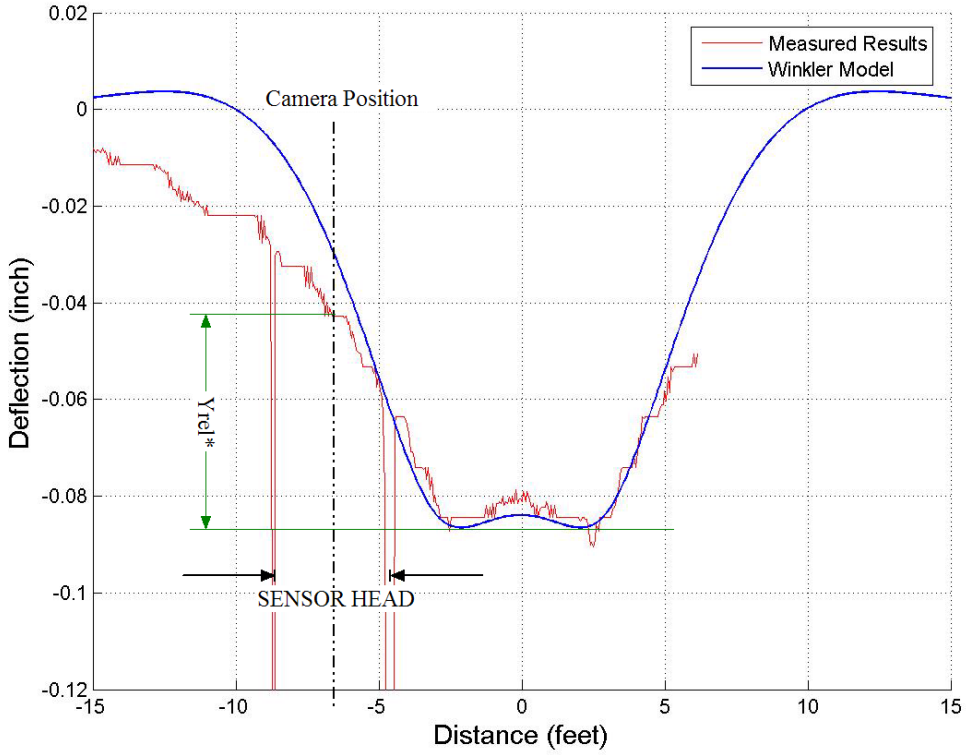

Figure 4-23. The Deflection Curve of the Rail from Calibration

During the calibration procedure, the measurement camera in the sensor head also captures the video of the laser lines on the top of the rail. This video is postprocessed to capture the image of the marker placed on the ballast as shown in Figure 4-24. This marker is simply used to indicate at what point in the video capture the sensor head is directly over the measurement point. From this image, the distance between the two laser lines (d^*) is obtained.

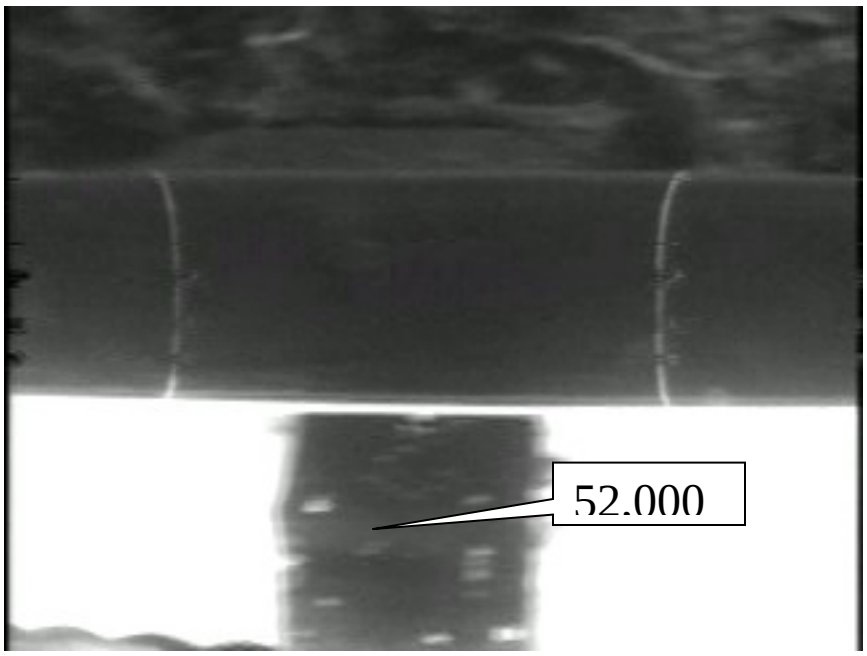

Figure 4-24. Captured Image when Sensor Head Passing by the Marker

This calibration procedure assumes that the section of track (approximately 40 ft around the sticker's position) is uniform. However, track conditions may change from tie to tie. Even though this procedure was done on a section of specially selected quality track, there is no guarantee that modulus over the section is a constant. Therefore, the accuracy of the results is worthy of further examination.

4.4.3.3 Verifying Calibration Results

After obtaining the ratio of Δd and $\Delta Yrel$, $Yrel^*$, and d^*, the distance between the two laser lines in the images can be converted into the measurement results, Yrel, by applying Equation 4.4-1. However, as stated above, it is difficult to accurately determine $Yrel^*$ and d^*. Therefore, another procedure was developed to verify $Yrel^*$, d^*, and the entire calibration results.

A mechanical shop for railroad vehicles is involved in this procedure. The track in this shop is assumed to be absolutely stiff such that no rail deflection will be considered when trains move across this section of track. This assumption is reasonable because the track in the shop is in good condition, and the rail is supported by a structural concrete foundation that limits track deflection.

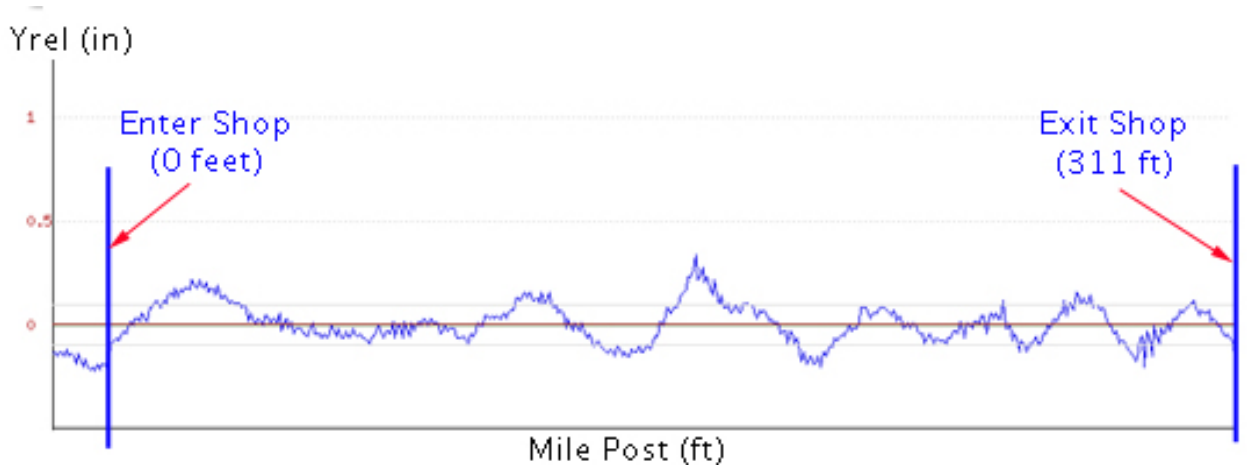

Figure 4-25. Yrel Data from the Mechanical Shop

The results of the Yrel data for this section of track are plotted in Figure 4-25. The average Yrel value is shown (horizontal red line) for the readings in the shop between entering the shop and exiting the shop. The average of Yrel over this section of track is 0.0018 in. This value is extremely close to the expected value of zero. The variations of Yrel, which are relatively small (standard deviation is less than 0.1 in), are attributed to the pre-existing geometry variations of the track.

4.4.4 Error Analysis

4.4.4.1 Errors Caused by Limited Sampling Rate

When the system was first implemented, the cameras used analog video signals in a National Television System Committee standard, which is 30 frames per second. As a result, individual data points were spaced approximately every 2 ft when the measurement vehicle travels at 40 mph. However, Yrel measurements may change considerably within 2 ft because certain track modulus and geometry variations occur over extremely short distances. Therefore, this limited sampling rate led to measurement errors.

For example, 50 ft of data using this older system is presented in 1-foot increments in Figure 4-26. The highest peak within the 50-foot range is point B, which is 0.77 in. If the test is conducted at a speed of 40 mph, the system used to record readings every 2 ft. As a result, the peak at point B could be missed, while only the data points at A and C would be recorded. Hence, an error of 0.04 in (the difference between points A and B) would result. Because the errors, based on limited sampling rate, depend on how the actual data varies over short distances, they were difficult to quantify. Some locations, such as joints, are much more sensitive to this sampling rate issue because the actual Yrel data can change dramatically over a few ties. On the basis of an examination of the data from past tests, the error could be as much as 0.2 in at some locations.

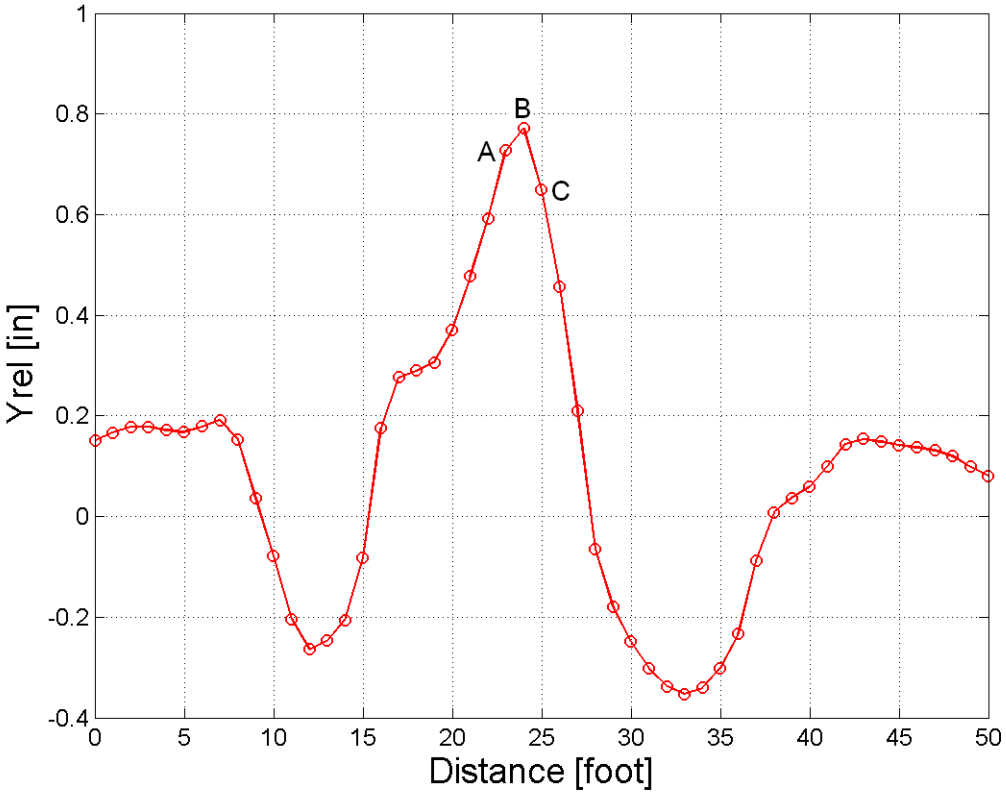

Figure 4-26. Limited Sampling Rate Causing Measurement Errors

To address the problem caused by the limited sampling rate, new higher speed cameras have been implemented to upgrade the system's sampling rate to a maximum of 120 frames per second. The current prototype system uses a sampling rate of 90 frames per second that leads to a measurement at approximately every 8 in at a testing speed of 60 mph. This greatly improved the system's measurement repeatability and accuracy and minimized all the potential errors discussed in this section.

4.4.4.2 Measurement Resolution

The measurement system is based on image processing. The most direct measurement output is the number of pixels between the two laser lines in the images. Therefore, the measurement resolution is directly determined by the resolution of the captured images.

The current system captures images at 90 frames per second with a resolution of 782 × 582 pixels. On the basis of the calibration results, for images of 782 × 582 pixels, one pixel in each image represents 0.00482 in of Yrel. Hence, the measurement system's resolution is less than 0.005 in.

4.4.4.3 Laser Line Width

The image processing program identifies locations of the laser lines by finding peaks of pixel intensities. However, as shown in Figure 4-27, a laser line can be as wide as three or four pixels in a captured image. Therefore, it is difficult for the image processing program to precisely

distinguish which pixel should represent the location of the laser lines, especially when two adjacent pixels have the same intensity. Although the curve fitting algorithm used in the image processing program greatly reduces the error caused by this factor, it is reasonable to conclude that an error of ±1 pixel (±0.0118 in Yrel for this camera system) may result.

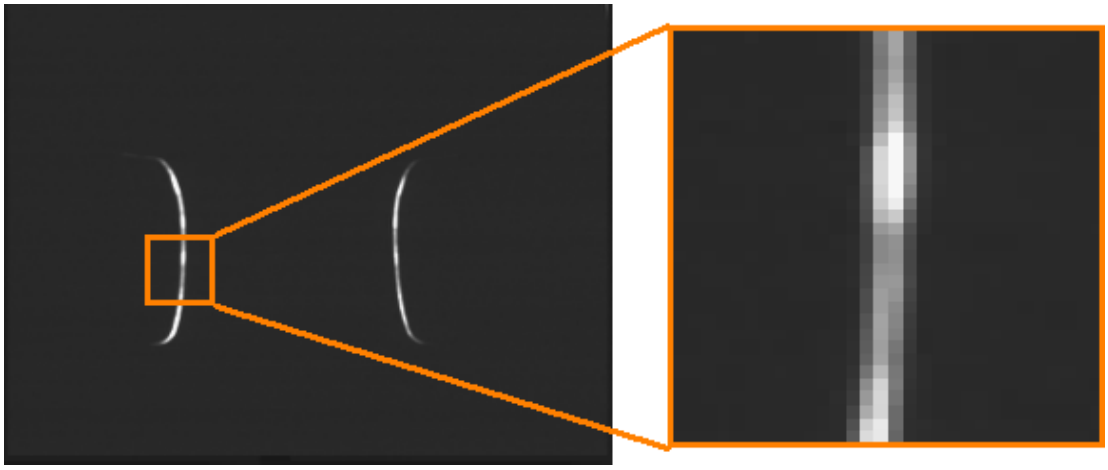

Figure 4-27. Laser Line Width

4.4.4.4 Laser Beam Drifting

The laser line generator's Boresight accuracy is rated at a maximum of 2.5 millimeters per meter. Boresight accuracy, known as pointing accuracy, is a measure of the angular difference between the beam propagating axis (where the laser beam is pointing) and the mechanical axis (where the laser housing is pointing). Because of the nature of the measurement principle and the calibration procedure, the Boresight accuracy has no effect on the measurement result because the measurement is not related to the mechanical axis of the laser housing. The calibration described in Section 3.4.3 shows that the absolute angle of the laser, defined by α in Figure 4-28, is not critical because the value of the angle is found, and confirmed, through the calibration process (from Section 3.4.3). As a result, no measurement error is caused by the Boresight inaccuracy; however, changes in this angle, defined as $\Delta\alpha$ or pointing stability, can lead to errors.

Pointing stability, a measure of how much the laser beam alignment drifts over a period of time, can lead to minor measurement errors. The laser line generator's pointing stability is rated at <50 µrad. The geometry relation between the lasers and the rail is shown in Figure 4-28, where H is the vertical height of the laser generator above the rail, α is the angle between the laser beam and the vertical direction, $\Delta\alpha$ is the drifted angle, and Δd is the drifted distance of the laser line on the rail.

From geometry relation, we know:

$$\Delta d = H \cdot \tan(\alpha) - H \cdot \tan(\alpha - \Delta\alpha) \qquad \text{Equation 4.4-2}$$

From the calibration, we know $H = 13.6$; $\alpha = 50°$; and the maximum $\Delta\alpha$ is 50 µrad. Therefore, Δd is calculated to be 0.0016 in. On the basis of the geometric relation from the calibration, 0.00165 inch in Δd will result in a $\Delta Yrel$ of 0.00165 × 0.853 = 0.0014 in.

Considering the worst-case scenario in which both laser beams are drifting either toward or away from the camera at the same time, the maximum error will be doubled. Therefore, the maximum error of Yrel that the laser beams drifting can cause is 0.0028 in, which is negligible.

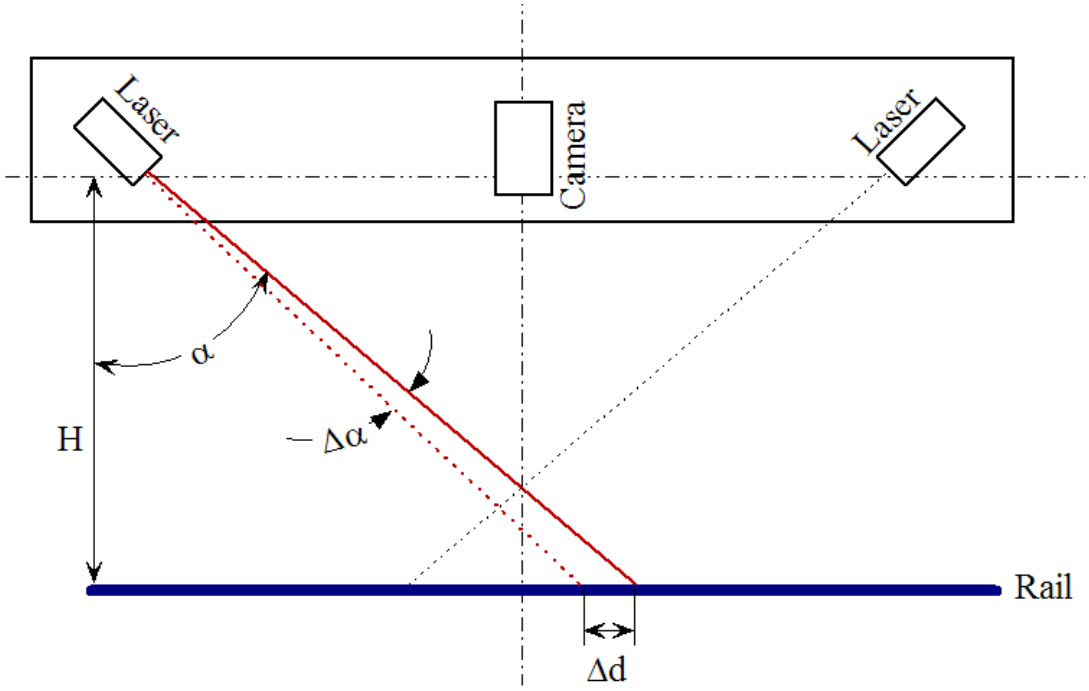

Figure 4-28. Laser Beam Drifting

5 Validation of the UNL System

A validation test was conducted in October 2008 on the UPRR's Yoder Subdivision between Egbert, WY, and Yoder, WY. The purpose of this validation test was to confirm the measurements collected by the system.

5.1 Measurement of Deflection

To validate the deflection measurements of the UNL's system, three verification methods were performed. The results from the three methods show that the measurement is accurate and repeatable as outlined in the following sections.

5.1.1 Stringline Measurements

As described previously in Section 3.1, Yrel is the distance from the rail surface under the camera to the wheel/rail contact plane. Therefore, the method depicted in Figure 5-1 to measure Yrel is very straightforward. Here, a string is pulled to pass the bottoms of the two wheels. Then, the distance from the top surface of the rail under the camera to the string is the Yrel reading at this location.

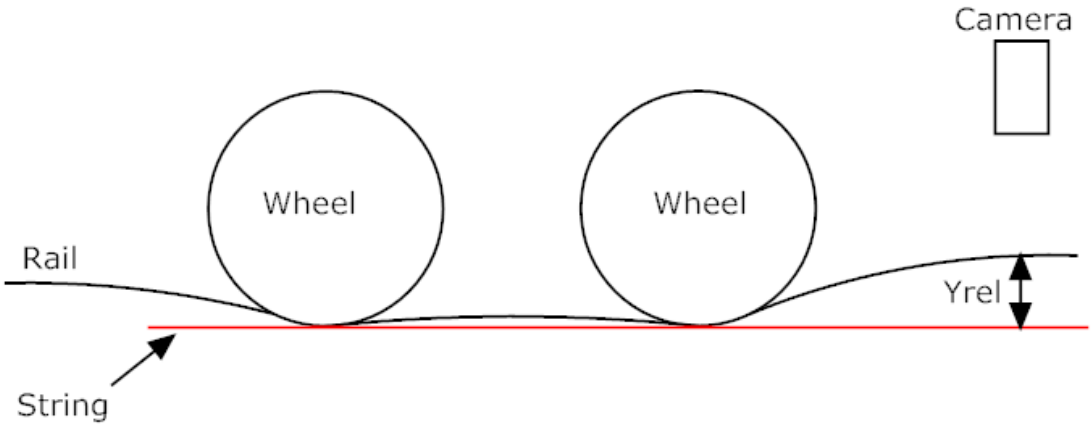

Figure 5-1. String Measurement Diagram

As shown in Figure 5-2, a specially made magnetic ruler is attached to the rail during the field measurement to make the reading process easier. The string is tightly held from the two ends as it barely touches the bottom of the two wheels. The distance from the top surface of the rail under the camera to the string is read to compare against the Yrel reading from the measurement system.

Figure 5-2. Field String Measurement

The string measurement was performed at three locations during the validation test. The measurement results and the Yrel measurements from the testing vehicle are listed in Table 5-1. The field string measurements and the Yrel measurements each differ by less than 0.1 in.

Table 5-1. String Measurement and Yrel Measurement

Locations	Yrel (in)	String Measurement (in)	Difference (in)
MP 192.84	1.000	1.004	0.004
MP 196.94	0.703	0.610	0.093
MP 217.22	0.703	0.669	0.004

The string measurements from these three locations closely matched the Yrel measurements from the testing vehicle, which suggests that the system's Yrel measurements are correct. However, this type of stringline measurement is not very accurate. A significant practical limitation is ensuring that the string perfectly passes the bottom of each of the two wheels—a rather difficult task. This limitation can easily contribute a relatively large error in the measurement results. To provide more accurate results, further methods were used, and they are described in the following sections.

5.1.2 Survey Measurements

This method uses a surveyor's total station as shown in Figure 5-3 to independently measure the vertical deflection of the rail. Such instruments are commonly available with an indicated accuracy of less than one millimeter. In this scenario, rulers used as targets are attached to the side of the railhead by strong magnets as shown in Figure 5-3.

Figure 5-3. Instruments Used in Survey Measurements

Figure 5-4 demonstrates the measurement scenario. Thirteen rulers are placed every 3 ft on the side of the rail so that the total measurement range is 36 ft. This distance is usually enough to cover the entire deflection basin. First, the unloaded profile of the rail is measured by using the total station and a glass Porro prism commonly used in surveying. Next, the total station is used to measure the height of each ruler on the side of the rail while the rail is unloaded. After the measurements are recorded, the locomotive parks the measurement vehicle on this section of the track such that the inboard axle is directly on top of the center ruler as shown in Figure 5-4. The total station is then used to take the height measurement of each ruler a second time. The difference between the two height measurements for the same ruler is the rail deflection at that ruler's location. Adding the deflection measurement to the unloaded rail profile, the loaded rail profile can then be determined. Analyzing the resulting measurements provides for confirmation of the measured Yrel reading.

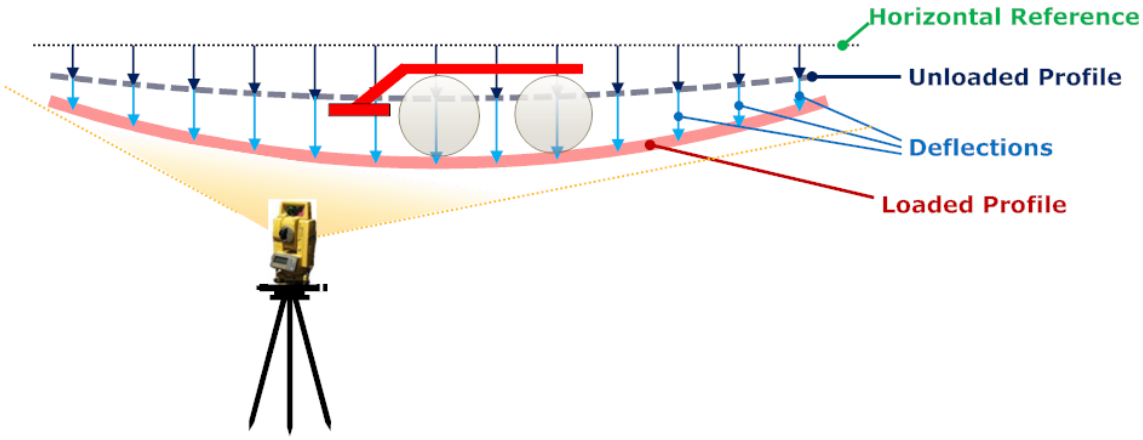

Figure 5-4. Measurement of Vertical Rail Position by Surveying

Survey measurements were conducted at two locations during the validation test. Measurement results from one of these locations are presented in Figure 5-5. The curve demonstrates the loaded profile of the rail with one wheel positioned at the origin and the other at a position of 70 in. The profile points at these two locations are connected with a line that is then extended by –48 inches in the horizontal direction. The distance from the end of the line to the rail at

position –48 in is the Yrel measurement at this location. As shown in the figure below, Yrel measures 0.732 in at this location.

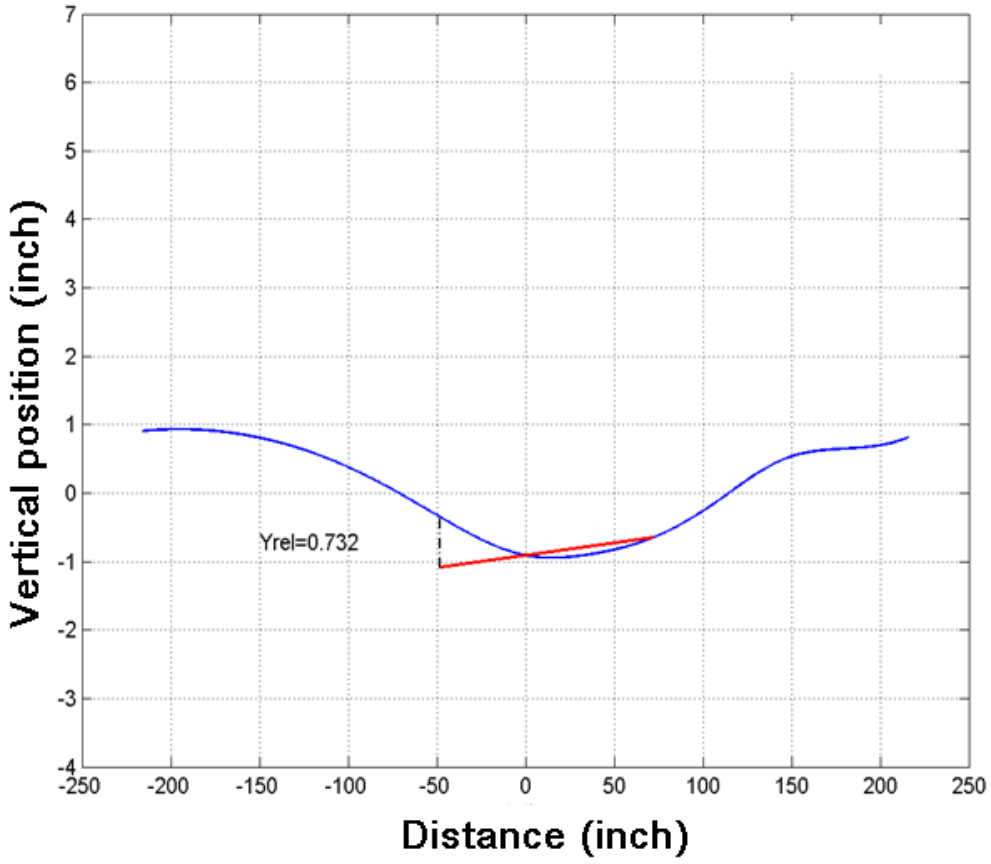

Figure 5-5. Survey Measurements

The testing vehicle's measurements are compared with the survey measurements from each site as shown in

Table 5-2, the two methods produced almost identical results at both sites. This suggests that the testing vehicle's measurements are accurate and reliable.

Table 5-2. Comparison between System Measurement and Survey Measurement

	Measurement from testing vehicle (in)	Measurement from surveying (in)	Difference (in)
Site A	0.738	0.732	0.006
Site B	0.150	0.150	0.000

5.1.3 Absolute Deflection Measurements by Cameras

Similar to the calibration procedure described in Section 4.3.3, a common camcorder is used to observe the vertical displacement of the rail as shown in Figure 5-6. A white magnetic strip is

affixed to the rail to use as a target. The camera records the video of the white strip as the moving train passes the location. The video is then postprocessed to determine the vertical location of the strip over time. This process is much simpler than using LVDT's as described in Section 2.3 and will provide complete information on the passing train. A section of sampled deflection data processed from a video of a coal train is presented in Figure 5-7. In this section of data, a series of coal hoppers causes the rail to deflect about one-half inch and three heavier locomotives at the end of the train to deflect the rail over 0.9 in.

Figure 5-6. Wayside Camera Measurements Setup

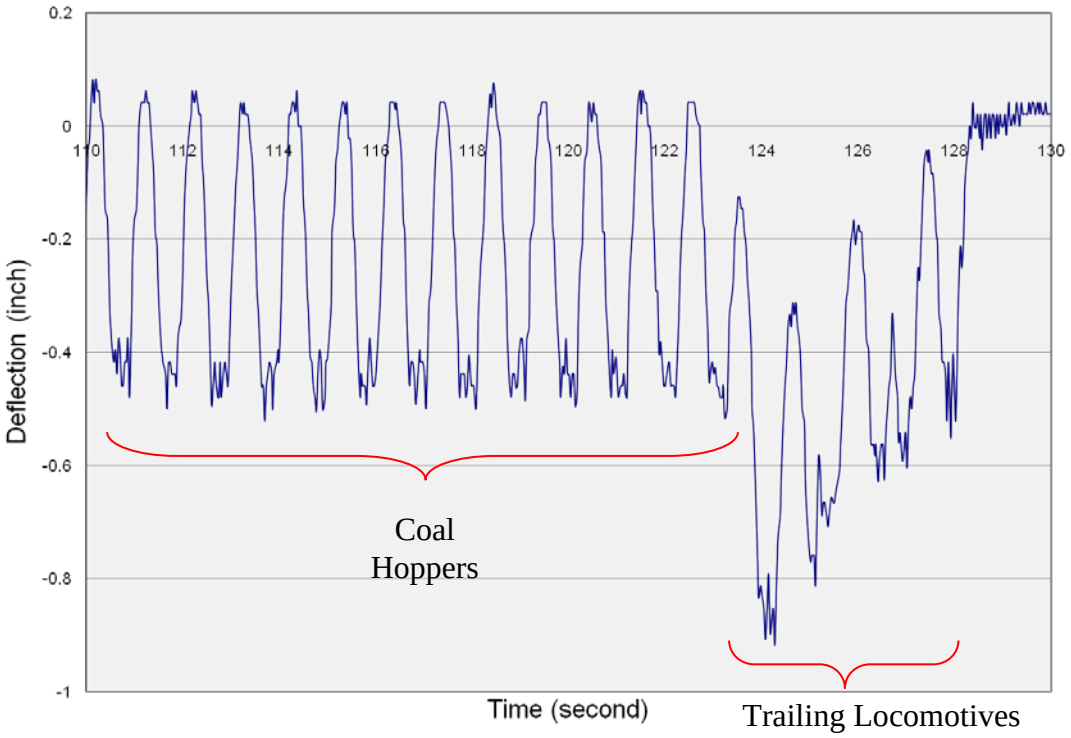

Figure 5-7. Sample Data of Absolute Deflection from Wayside Cameras

During the validation test, this type of absolute deflection measurement was conducted at three locations where survey measurements were also performed. The raw data of deflection over time from one of the locations is plotted in Figure 5-8. Here, the deflection caused by the locomotive, the test vehicle (UNLX002) and the geometry car are identified, respectively. The maximum deflection of the rail caused by the test vehicle load occurred at point A, which is the moment when the axles pass by the position of the magnetic strip. The maximum absolute deflection was determined to be 1.1 in for this location. Similar plots were made for the other two locations and the absolute deflections were evaluated.

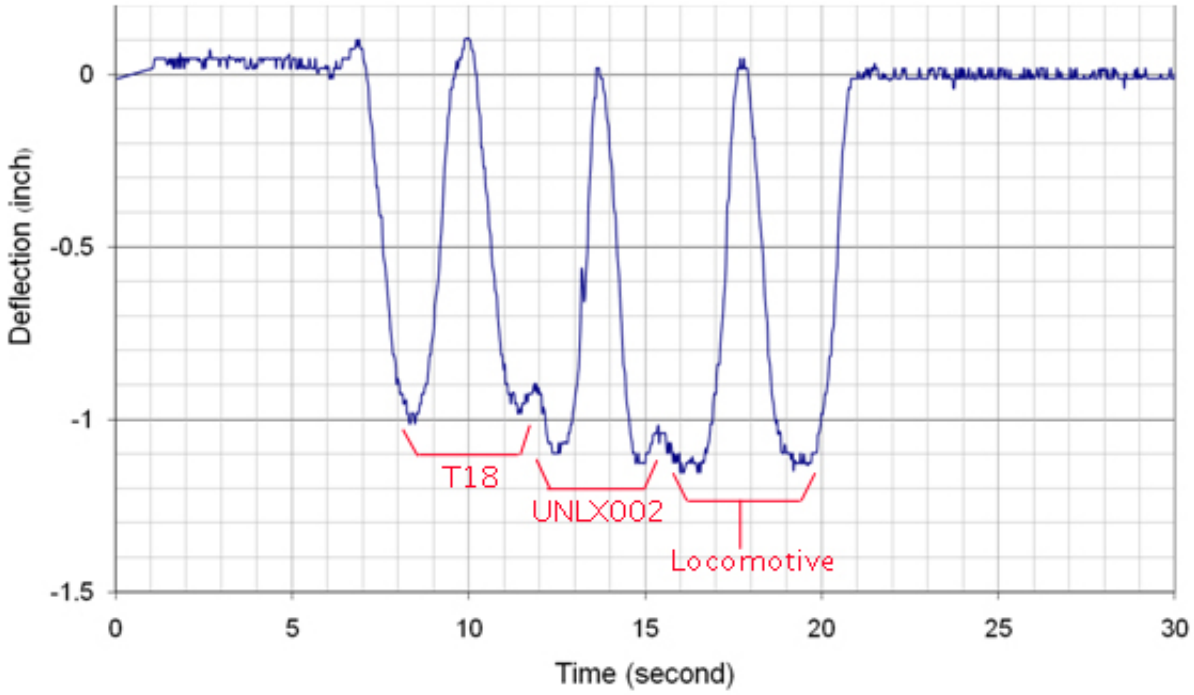

Figure 5-8. Deflection Data from Camera Measurement

Table 5-3 contains all of the deflection data from the surveying measurements and the camera video at the three locations. The three deflection measurements from the camera are very close to the corresponding ones from the surveying technique. The differences are less than 0.1 in at each location, so the two types of measurements support one another.

Table 5-3. Comparison between Measurements from Surveying and Camera

	Deflection from Surveying (in)	Deflection from Camera (in)	Difference (in)
Location #1	0.35	0.34	0.01
Location #2	1.14	1.1	0.04
Location #3	0.7	0.8	0.1

5.1.4 Summary

The string measurements and the survey measurements confirm the systems Yrel measurements accurately. The maximum error from the three locations in string measurements is less than 0.1 in and the survey measurements from the two sites were almost identical to the systems Yrel measurements. Results from these methods confirm that the system's measurement is accurate and reliable.

By comparing the survey measurement to the measurements by the wayside camera and then comparing both to the Yrel measurement, demonstrated accuracy is less than 0.1 in at each of these locations.

5.2 Measurement of Strain

Stress in rail can result from a complex combination of loads. Longitudinal loads can result from temperature-based expansion of the rails, while shear loads can result from tie supports and wheel loads. Rail cant and gage widening can also contribute to unusual loading conditions. However, axial stresses, and particularly cyclic axial stresses, often dominate rail stress and lead to crack growth and fatigue failure. Major contributions to the axial stress come from 1) temperature-based longitudinal rail stress, 2) bending stress associated with the wheel loads, and 3) contact stresses associated with the wheel-rail contact patch, as indicated in Figure 5-9.

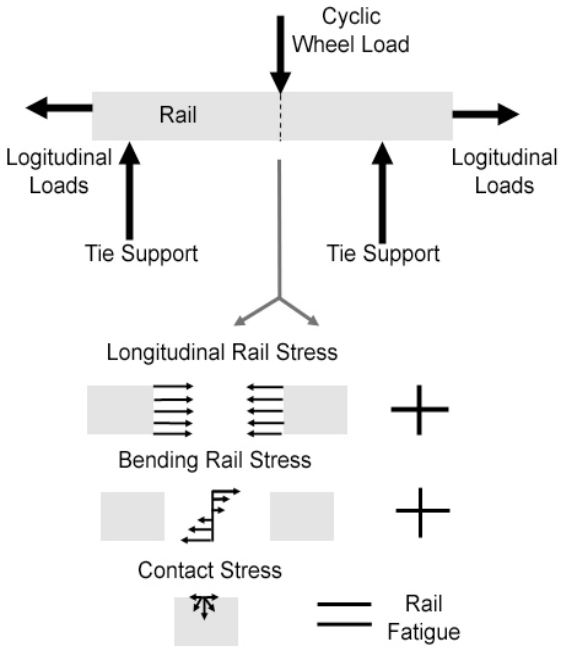

Figure 5-9. Rail Stresses and Fatigue

Each of these three factors can be significant and difficult to measure. Of the three, rail contact stress can be the most predictable because the wheel loads are generally a function of the applied loads and material properties of the rail. However, both temperature-based longitudinal stress and bending stress are difficult to determine. Both can dominate the stress field in the rail and both can independently lead to rail failure. A new method is presented to estimate one of these two important stresses, the rail bending stress. The measurement system is explained, and the mathematical background is presented that allows the measurement to be mapped into rail stress. Field results are presented from two sites on the Union Pacific's Yoder subdivision. These results show that the measured bending stress match the predicted stress to within approximately 12–14 percent.

5.2.1 Mapping Yrel into Bending Strain

The UNL track deflection system measures three points on the rail that partially describes the deflected shape of the rail under load. Because the deflected shape is mainly determined by the applied load, a method was devised for estimating the rail strain induced from the applied load, which could be used to estimate rail stress. Several models can be used, but the classical approach is the Winkler model (Cai et al., 1994; Ebersohn and Selig, 1994). The Winker model is briefly presented here, and it is shown how it can be mapped into rail stress given a value of

Yrel. The model is then confirmed in the following section using field testing and strain gages. Future work may use the cubic model described in Section 2.1.1.3.

When multiple loads are present, the rail deflections caused by each of the loads are superimposed (assuming small vertical deflections) to produce the rail shape under the wheel loads (Lu et al., 2007).

Figure 5-10 shows the rail shape for two axle loads (and other axles of a trailing car to the right not shown in the figure) of the UNL test car. The individual deflections from the Winkler model for each axle (axles 3 and 4) are shown in dashed lines with the solid (blue) line showing the loaded rail shape. A line is then drawn to create the wheel-rail chord and a value of Yrel can be calculated (0.099 inch in the figure). Given that the wheel loads are 70 in apart and the Yrel measurement is 48 in from axle 3, Yrel is calculated as:

$$Yrel = \frac{118}{70} y(0) - \frac{48}{70} y(-70) - y(48) \qquad \text{Equation 4.2-1}$$

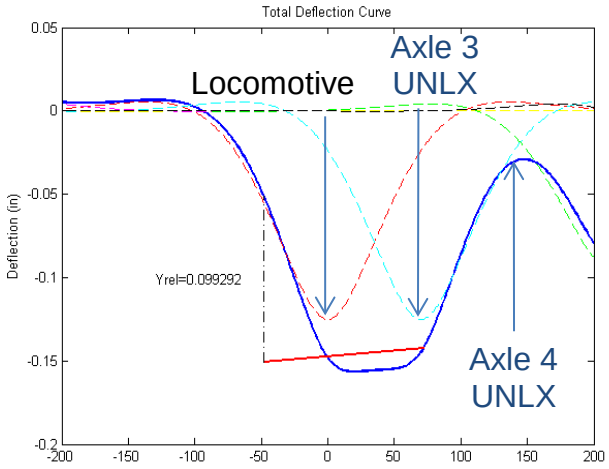

Figure 5-10. Winker Shape of Rail with Yrel Value

The bending moment, *M(x)*, which results from the deflection estimated by the Winkler model, is shown below.

$$M(x) = \frac{P}{4\beta} e^{-\beta|x|} [\cos(\beta\,|\,x\,|) - \sin\beta\,|\,x\,|)] \qquad \text{Equation 4.2-2}$$

The bending moment, M, is calculated for $x = 0$, which corresponds to the location of axle 3. Knowledge of the bending moment allows for the calculation of the bending strain present in the rail due to the application of the axle loads. The strain resulting from the applied bending moment is:

$$\varepsilon = \frac{Mz}{EI}$$ Equation 4.2-3

where ε is the rail bending strain, E is the modulus of elasticity for the rail material, I is the moment of inertia, and z is the vertical distance from the neutral axis of the rail to the strain location.

The preceding calculations used the Winkler model to calculate theoretical Yrel and bending strain values for a known set of loading conditions. For a particular rail profile and set of axle loads, the only variation in the calculations is the track modulus. Varying the track modulus and calculating the corresponding Yrel and bending strain values allows for the creation of a lookup table, which is displayed graphically in Figure 5-11.

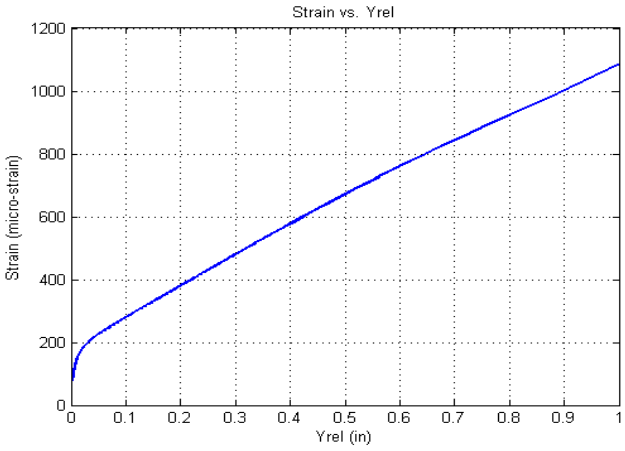

Figure 5-11. Relationship between Yrel and Rail Strain

5.2.2 Field Strain Measurement

Field tests were conducted on the UPRR's Yoder subdivision to verify the theoretical mapping of Yrel measurements into bending strain values. The tests consisted of mounting strain gages on top of the rail's bottom flange and comparing the strain gage value to a value calculated from Yrel with the UNL measurement system. The strain gages were mounted on the unloaded rail, and all measurements of strain were relative to the pre-existing strain state. For example, after being mounted, the strain gages would indicate zero strain, even though there is undoubtedly strain present in the rail (i.e., rail is not at neutral temperature, rail is not perfectly straight, and rail has residual stress from manufacturing). All measurements from the strain gages indicate a change in strain from this initial state. This removes effects from changes in neutral temperature (as measurements were made at approximately the same temperature as the gages were mounted) and the effects of residual stresses so the measurements can focus on the change in bending strain.

The strain gages were placed symmetrically on each side of the rail in a Wheatstone bridge configuration as shown in Figure 5-12, where E_i is the input voltage and E_o is the output voltage. This two-gage bridge configuration is designed to cancel any off-axis transverse loading effects that might be present.

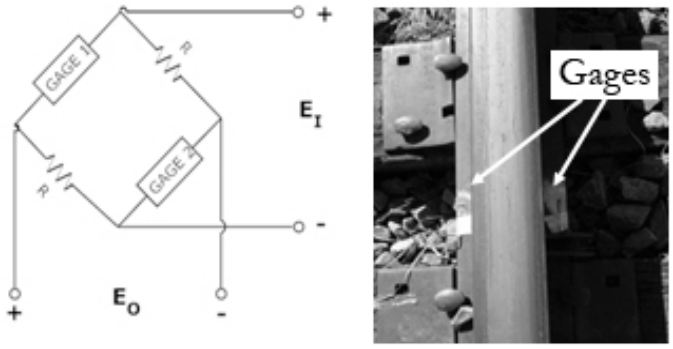

Figure 5-12. Two Gage Wheatstone Bridge Configuration

The output from the bridge was input into a Vishay Model 2150 strain indicator and signal conditioner and then recorded with a standard analog-to-digital USB input card. The strain output from the strain indicator is expressed as:

$$\varepsilon_b = \frac{\varepsilon_q}{k} = \frac{\varepsilon_q}{2} = \frac{2\Delta E_o}{F(E_i - 2\Delta E_o)} \qquad \text{Equation 4.2-4}$$

where:

εb = strain output from strain indicator

εq = strain output for a quarter-bridge Wheatstone bridge

ΔE_o = change in output voltage recorded from strain indicator

E_i = excitation voltage input to bridge (10 volts)

F = gage factor (~2.1 for all gages used in tests)

k = bridge factor (2 for the bridge configuration of Figure 5-12)

The measured strain was then correlated to the Yrel measurement made, whereas axle 3 of the hopper car was spotted on the strain gages. Figure 5-13 shows an example strain measurement as the test car is spotted at a measurement location. Increases in strain are seen as the locomotive passes over the strain gage followed by axles 1 and 2 of the test car. As axle 3 is placed directly over the strain gage, it can be seen that the strain increases from 0 to 290 με.

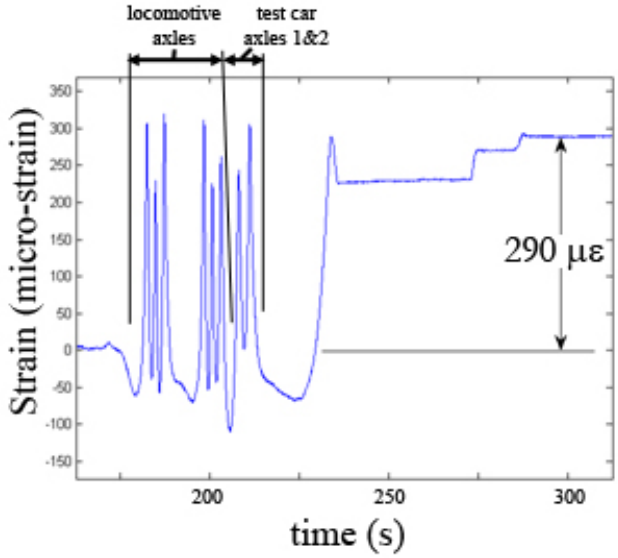

Figure 5-13. Strain as Test Car is Spotted

5.2.3 Field Profile Measurement

Figure 5-13 shows the unloaded strain (before the train is spotted) to be zero. This is because the strain gage was mounted to the unloaded rail. The strain measured by the gages (290 με in Figure 5-13) indicates the change in strain relative to the unloaded profile and cancels out effects of temperature-based axial strain (since temperature didn't change significantly as the train was spotted) and residual stresses. However, it is important to know the initial bending strain present in the unloaded profile since the unloaded profile is not perfectly straight. To accomplish this, a measurement of the unloaded (and loaded) profile was made using an independent measurement system described previously in Figure 5-4.

5.2.4 Strain Measurement Results

Two sites were chosen to compare the strain calculated from the UNL Yrel measurement with strain measured from the strain gage. Both sites were on the Union Pacific's Yoder subdivision in southeastern Wyoming. Measurements were made on October 15, 2008. The track at both locations had 132-pound rail and wood ties. This subdivision receives approximately 2 million gross tons (MGT) per year in traffic.

The first site tested (MP 231.6) was a tangent section of track with good rail support from a visual inspection. The second site (MP 228.6) was near an at-grade road crossing with muddy ballast and visually obvious rail pumping. The strain at the first site was expected to be low with the strain at the second site expected to be higher.

5.2.4.1 Tangent Track with Good Support (MP 231.6)

Figure 5-14 shows the measurement results from the well-supported tangent track at MP 231.6. The Yrel reading at this location was 0.15 in indicating stiff track. Therefore, an absolute bending strain of 332 με is predicted from the lookup graph in Figure 5-11. The strain gage reading relative to the unloaded profile was 290 με. However, there is clearly some initial bending strain as a result of the initial unloaded profile (again, the strain gage was mounted on

the unloaded profile that was not perfectly straight). To match the Yrel indicated strain with the strain gage measurement, the unloaded bending strain must be removed from the Yrel measurement.

To make this correction, Figure 5-14 also shows the results of the survey of both the loaded and unloaded profile. Both the loaded and unloaded profiles are displayed with the values of displacement shown next to the arrows in inches. These profiles are used to calculate a change in Yrel called *ΔYrel*. This new *ΔYrel* is the loaded Yrel from the measurement car minus a Yrel value calculated from the unloaded profile. The strain predicted from the ΔYrel value and the lookup graph in Figure 5-11 can now be compared to the change in strain measured by the strain gage.

In this case, the loaded Yrel value is 0.015 in, and the "unloaded Yrel" is 0.001 in. Therefore, the *ΔYrel* is 0.149 in, and the change in bending strain from loaded to unloaded is 330 με. This calculation differs from the strain gage measurement of 290 μ-strain by only 13.7 percent. In this location, the unloaded Yrel is not significant (only 0.001 in), and the loaded Yrel is nearly identical to the *ΔYrel*.

Given all this, it is believed that the original value of loaded Yrel from the measurement test car is a realistic indicator of bending strain. However, the *ΔYrel* value is used to compare to the strain gage readings and validate the measurement only because the strain gages are not mounted when the rail is strain free. This becomes more important at the following site where there is significant bending strain in the unloaded rail (significant unloaded geometry).

5.2.4.2 Pumping Track (MP 228.6)

Figure 5-15 shows the measurement results from the poorly supported track with muddy ballast and visually obvious track pumping at MP 228.6. The Yrel reading at this location was 0.73 in, indicating softer track. This would predict an absolute bending strain of 868 με. The strain gage at this location measured a 580-με change in strain between the unloaded and the loaded state.

In this location, the unloaded profile has a significant dip. A Yrel reading calculated from the unloaded profile indicates a value of 0.254 in. Repeating the method described earlier, the calculated unloaded Yrel value is subtracted from the measured Yrel value and the result is used to determine a strain value in the look-up table. The Δ*Yrel* in this case is 0.478 in predicting a strain of 651 με.

The calculated strain of 651 με differs by 12.2 percent from the measured strain of 580 με. Again, it is believed that the absolute bending strain is best represented by the original Yrel measurement of 868 με. However, the Δ*Yrel* value is used to compare to the strain gage readings and to validate the measurement only because the strain gages are not mounted when the rail is strain free. The results from both tests are displayed in Table 5-4 below.

Table 5-4. Comparison for Strain Measurement

	MP231.6	MP228.6
Strain from $\Delta Yrel$	330	651
Strain from gage	290	580
% Error	**13.7%**	**12.2%**

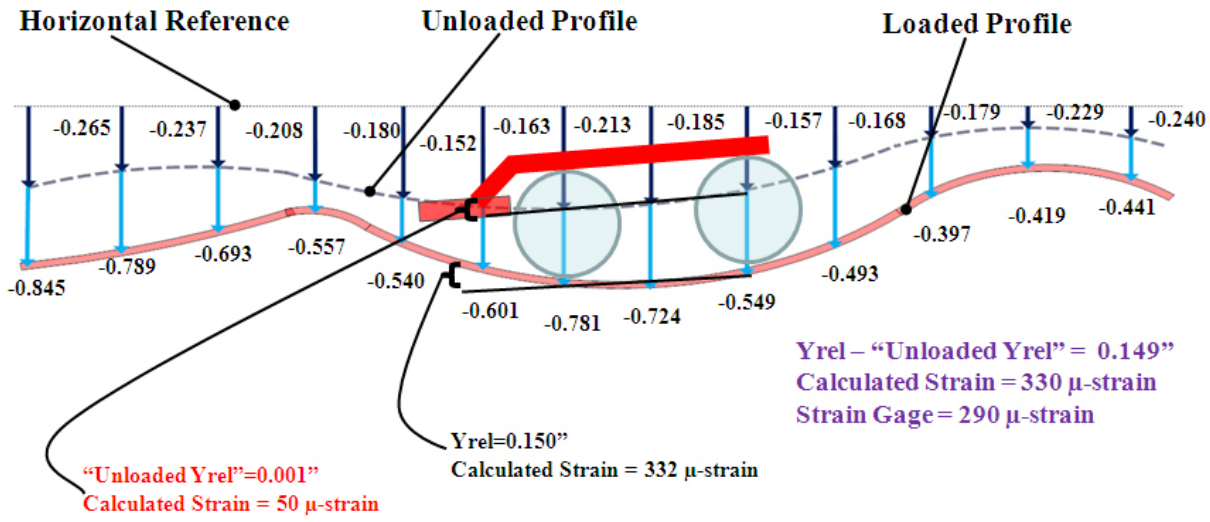

Figure 5-14. Measurements from Tangent Track (MP 231.6)

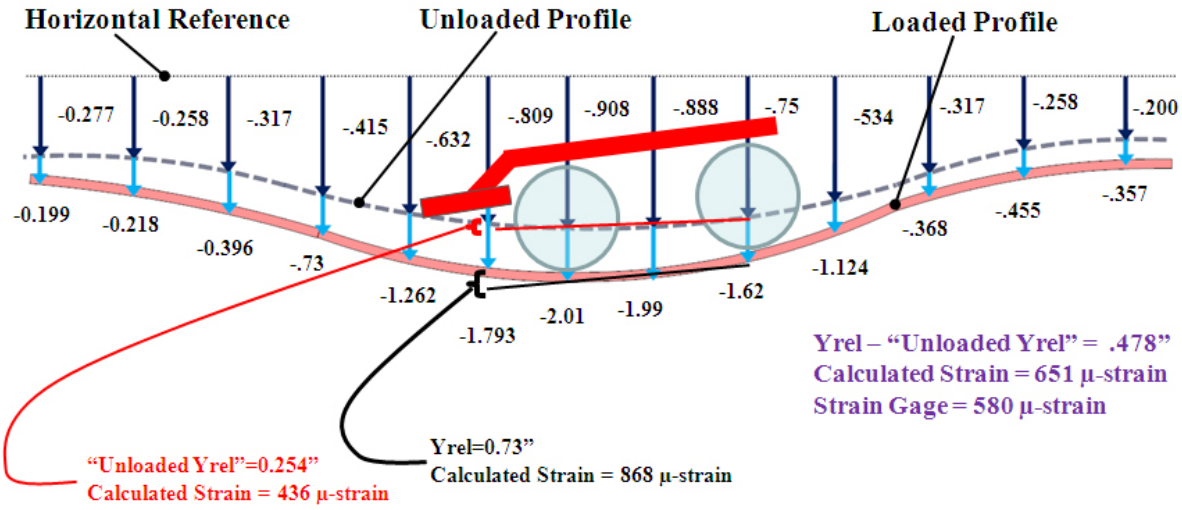

Figure 5-15. Measurements from Pumping Track (MP 228.6)

5.2.5 Summary and Conclusions

The UNL system measures three points of the rail shape beneath the loaded wheels including the location of highest bending stress below the loaded wheels. This direct measurement of the rail shape can then be mapped into rail stress through the curvature of the rail and beam theory.

As verification of the UNL measurement system, results from tests conducted on the UPRR's Yoder Subdivision are discussed. In these tests, bondable resistance strain gages were mounted to the lower flange of the rail at several locations. The track was then loaded by spotting the measurement car over the strain gages and by moving the car over the gages at various speeds. The loaded and unloaded profiles were measured using surveying equipment, and the relationship between the UNL deflection measurement and the measured rail stress was explored.

The field results show a strong correlation between the strain calculated from Yrel and the strain gage measurement. The differences at the two sites of 13.7 and 12.2 percent are well within the modeling errors and the measurement errors present in the field tests. In both instances, the calculated strain was slightly above that of the measured strain. The lower measured value may have resulted from slight misalignment of the strain gages with the axis of the rail. Furthermore, the axle may not have been parked exactly above the strain gages so that the gages did not record the maximum strain present directly beneath the axle.

These results suggest the UNL system is capable of accurately measuring real-time bending stress in the rail given the assumption that the rail would be in a zero bending stress state when the rail is straight. The validity of this assumption is unclear, and the entire process of measuring bending stress needs further examination.

6 Testing on the Union Pacific South Morrill Subdivision

Since 2006, the measurement system has conducted revenue service tests in many locations including the BNSF Railway's St. Joseph subdivision in Kansas, as well as the South Morrill subdivision, Sidney subdivision, Ravenna subdivision, and Powder River subdivision, all of the UPRR. Some short distance tests such as between Lincoln and Ashland, NE, and between Lincoln and Tecumseh, NE, were also conducted.

Recent tests focused on the 160 miles of heavy-axle load freight line of UPRR on the South Morrill subdivision of the North Platte division. The tests were performed on Main 1 (primarily unloaded, empty coal trains returning to the mine with approximately 50 MGT/year) and Main 2 (primarily loaded coal trains with approximately 250 MGT/year) of the subdivision. Repeated tests were conducted on this subdivision in October 2006, December 2006, February 2007, April 2007, January 2008, April 2008, and June 2008. Tests were done at speeds up to 60 mph in a work train consist. The autonomous testing ability of the system made these tests easy to conduct and cost-efficient. These repeated tests were performed in different seasons, under different weather conditions, and at different speeds, providing tremendous amounts of data for analysis. Figure 6-1 shows the measurement vehicle in the consist of a coal train during a test.

Figure 6-1. System in Revenue Service Testing

An example of data recorded over a distance of one mile is shown in Figure 6-2. The plot shows the relative deflection of the rail, Yrel (as defined in Figure 3-1), as a function of GPS coordinates given in degrees of longitude and latitude. The data is overlaid on a satellite image (Google Map). In this figure it is possible to qualitatively trace changes in relative deflection to specific track events such as grade crossings, culverts, and bridges.

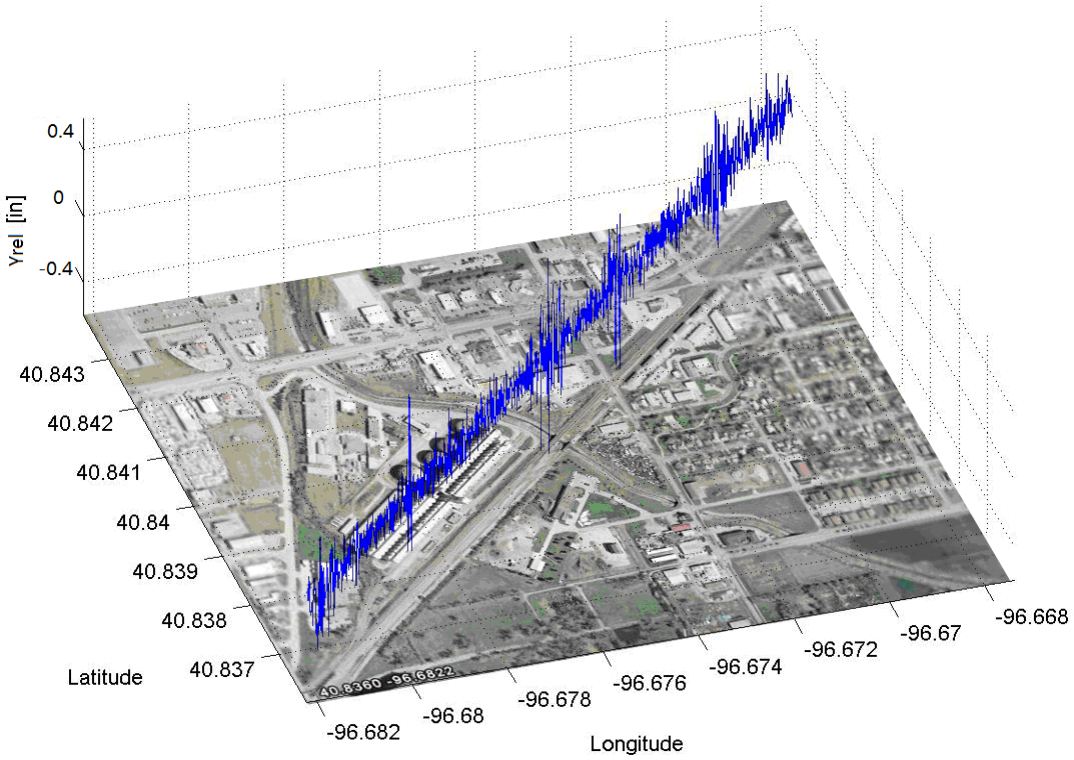

Figure 6-2. Yrel Data Overlaid on a Satellite Map

Figure 6-3 shows data from 1 mile of track. The plot shows the relative rail deflection between the measurement point and the wheel-rail contact point (Yrel as defined in Figure 3-1). Also shown are the mean and standard deviation of the data. The mean represents the average value over the past 0.1 miles of track and the standard deviation corresponds to that mean over the same distance. This distance was chosen arbitrarily as a characteristic length. The mean and standard deviation are therefore dependent on the direction of travel (right to left in this plot).

This section is an interesting example because it corresponds to a high-speed crossover between MP 0.6 and 0.9. A noninsulated joint bar (near MP 0.9) is located at the right end of the crossover. The relative deflection at this point was very large (over 1 in), indicating a very low track modulus. The joint bar failed and caused a derailment only 2 wk after the track modulus measurements were taken. This location represented the second highest relative deflection measurement recorded over the nearly 350 miles of track tested for this portion of the test. This spike in relative displacement obviously caused a jump in both the mean and standard deviation of the data. The other end of the crossover (near MP 0.65) also displayed a rise in the standard deviation, indicating a rough section of track.

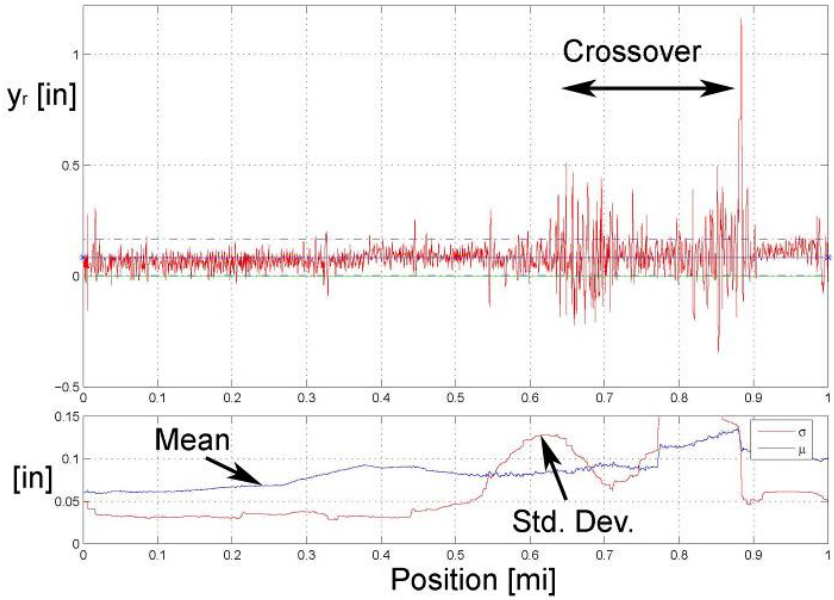

Figure 6-3. A Rough High-Speed Crossover

In contrast to Figure 6-3, an example of 1 mile of quality track is shown in Figure 6-4. Yrel and therefore modulus were both very consistent over this section of track. The consistent mean and relatively low standard deviation emphasize the track's quality.

The results of these tests suggest that information in these measurements may be useful in indicating unsafe sections of track in need of repair. The contrast between the two figures suggests a quantitative method to more rationally schedule and prioritize track maintenance.

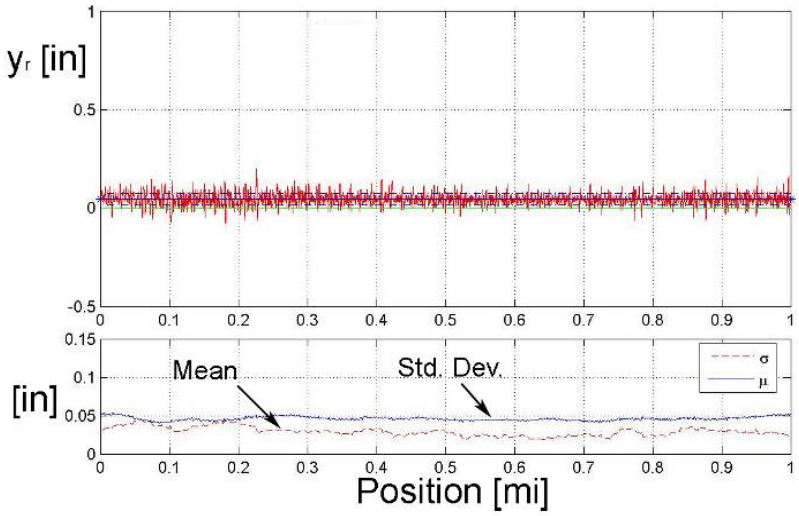

Figure 6-4. Track with Consistent Modulus

6.1 Derailments following the 2007 Test

Postprocessing of the data indicated a correlation with two of the top 10 deflection locations and the location of two derailments. These were within 30 days of the track modulus measurement date.

The exception list was generated, based on the large values of Yrel and large defections (Yrel – ECO) criterion, and was independent of the knowledge of the derailments. The site with the second highest difference exception, MP B.89, coincided with the location of a defective field weld, which caused an eight-car derailment 14 days after the test. The site with the 10th highest exception at MP J.58 coincided with the location of a broken joint bar derailment 30 days after the test.

The site with the second highest deflection was MP B.89. The raw data from that location is shown in Figure 6-5 for 1 mile of track. The exception at MP B.89 is clearly visible with a large peak in relative displacement. The standard deviation is also larger around this turnout. Although no one observed the failure, the assumption of railroad staff is that the poor track support contributed additional stress to the weld under each passing wheel load and the weld continued to degrade until failure 14 days later resulting in a derailment.

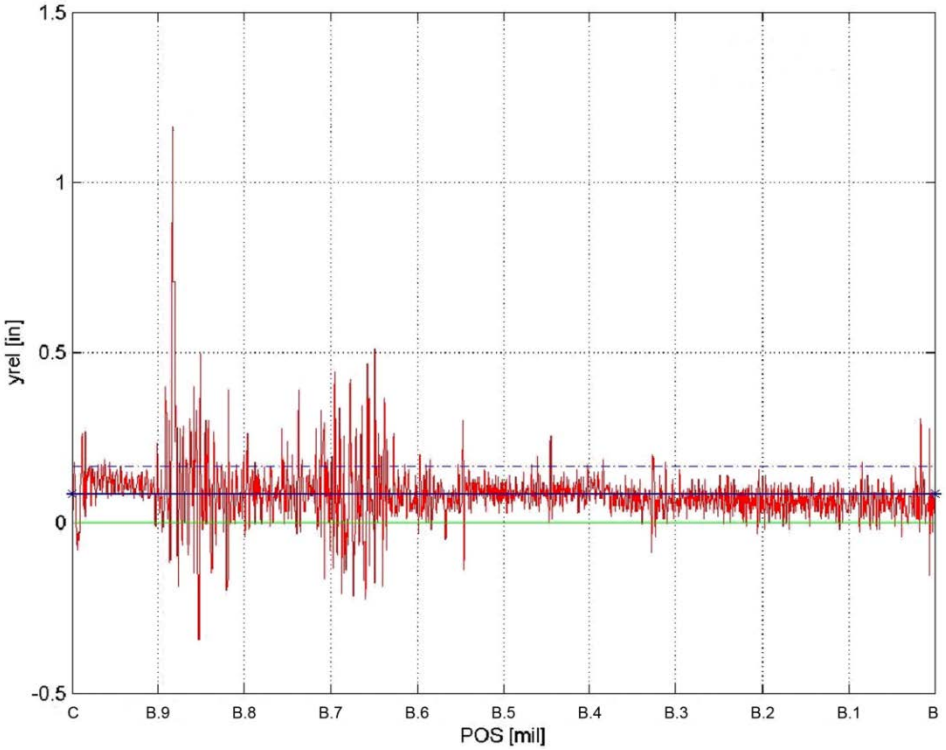

Figure 6-5. Site of Broken Field Weld 14 Days after Test

The site with the 10th highest deflection was at MP J.58. The raw data from that location is shown in Figure 6-6 for 1 mile of track. The exception at MP J.58 is also visible with a large peak in Yrel measurements. The standard deviation is also larger around this turnout with both ends of the turnout clearly visible. Although no one observed the failure, the assumption of railroad staff is that the poor track support contributed additional stress to the joint under each passing wheel load, and the joint continued to degrade until failure of the noninsulated joint.

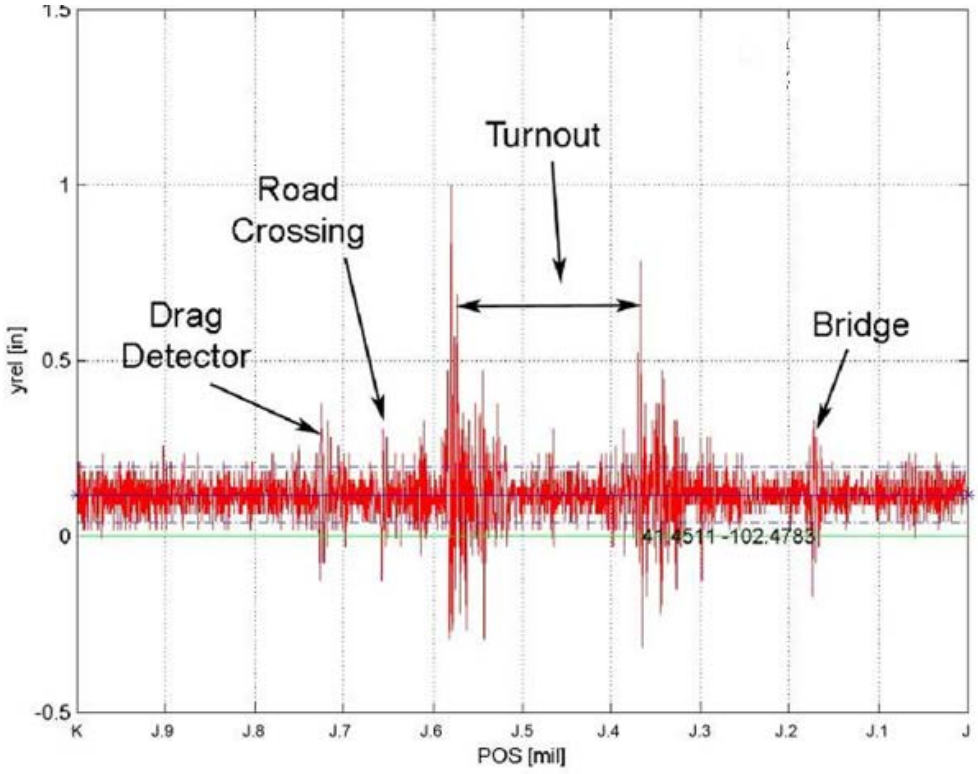

Figure 6-6. Failed Noninsulated Joint 30 Days Posttest

6.2 System Measurement under Various Conditions

6.2.1 Results from Different Train Speeds

The results from multiple tests in South Morrill subdivision suggest that the measurements are not strongly related to the train speed. The average train speed for the 0.1 miles shown in Figure 6-7 are 48, 22, and 35 mph, respectively.

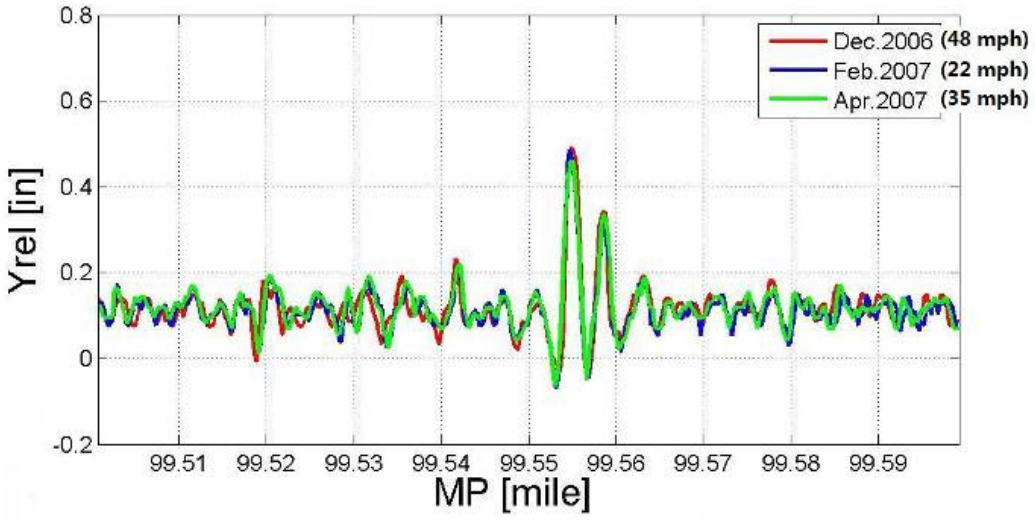

Figure 6-7. Measurements from Different Speeds

Repeated tests over the same section of the track at different speeds were performed during a special validation test on the Yoder subdivision. Four different speeds (20, 30, 40, and 50 mph) were tested. For most of the sections, the measurements from the different speeds are highly repeatable, which indicates that the speed is not a significant factor in the measurements at those locations. However, at some locations, differences do exist between the different speeds. The section shown in Figure 6-8 is an example of these locations. The values of the peaks at MP 224.4685 corresponding to the four different speeds within this short section (21, 30, 40, and 48 mph) are 0.607, 0.687, 0.692, and 0.77 in, respectively. The Yrel measurements increased 0.163 in when the train speed increased from 21 to 48 mph. This can possibly be explained by an increased dynamic load when the train moves at higher speeds.

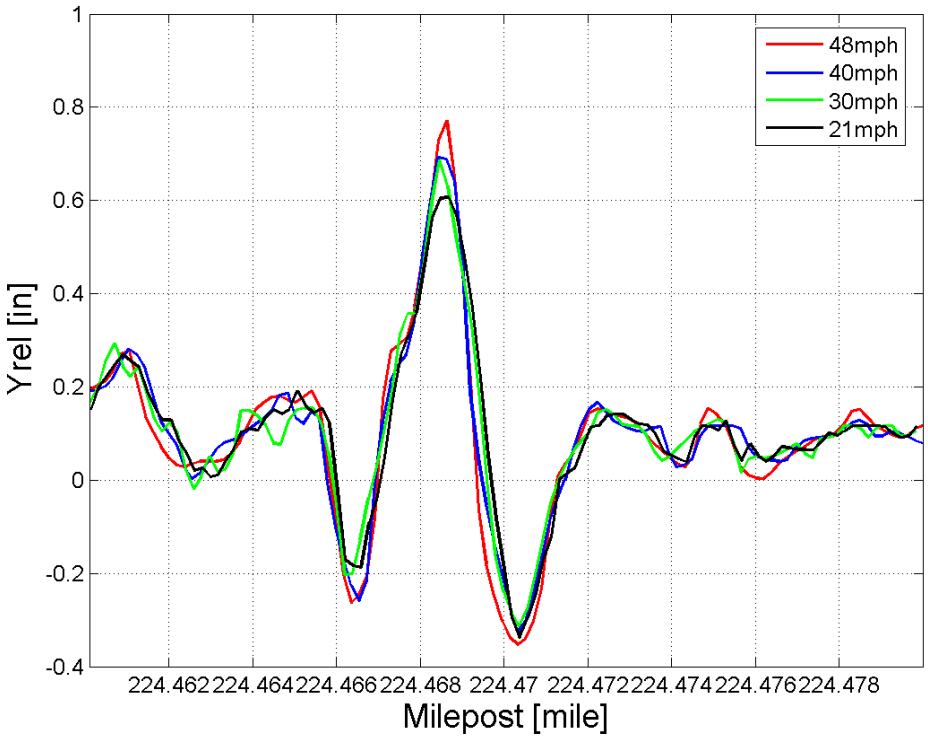

Figure 6-8. Dynamic Loads Affecting Measurements at Different Speeds

6.2.2 Results from Different Seasons

Although most of comparisons between tests showed significant repeatability as shown in and Figure 6-7 and Figure 6-8, there were some variations in certain sections of track. The most noticeable variation is the comparison between the December 2006 test and the other tests. At multiple locations of the track, the relative deflection data (Yrel) from the test in December 2006 has an offset compared with the results from other tests as shown in Figure 6-9. The test in December 2006 was special because it was conducted in extreme weather conditions with falling snow and an ambient temperature around a high of 20°F. Figure 6-9 shows similarity in the shape of the measurements but a shift in the Test 2 measurement. The December 2006 test has a lower mean value, indicating the track is stiffer (smaller Yrel). This could indicate a change in track modulus associated with frozen track that may contain moisture. These results suggest the system could be useful to quantify seasonal variations in track modulus caused by factors such as variations in subgrade moisture.

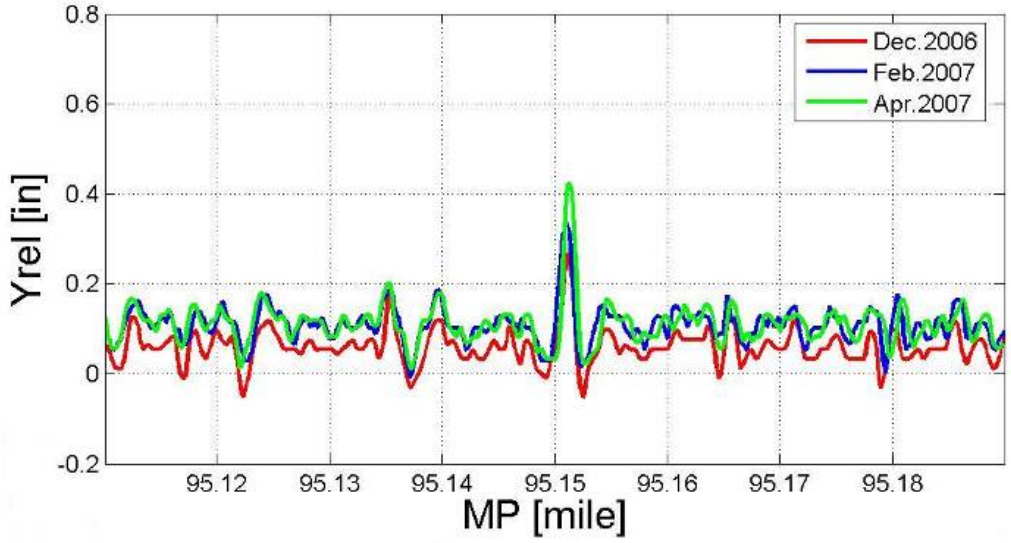

Figure 6-9. Variations of the Measurements

Interestingly, the offset of the measurements shown in Figure 6-9 only occurred at some track sections. Figure 6-10 shows a section of track where only the measurements on the left half of the figure has this offset, whereas on the right half of the figure the results from the three tests are very similar. This could indicate variations of subgrade moisture can lead to greater (or lesser) seasonal variations in track modulus.

The conclusion here is that seasonal variations are significant and measureable with this system. Such absolute seasonal measurements cannot be made with dead-reckoning measurement systems that only measure position relative to the previous position (e.g., acceleration-based profile). These measurements show areas of track that contain significant moisture and therefore have changes in stiffness under frozen and nonfrozen conditions. Areas of track that do not contain significant moisture do not have as much of a change in stiffness or areas that are dominated by geometry variations may not show changes.

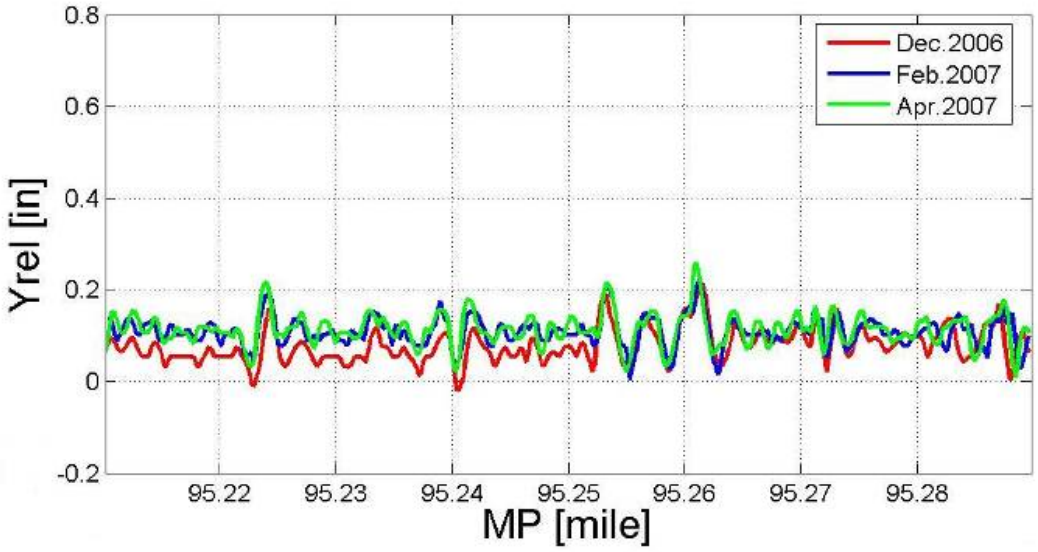

Figure 6-10. Variations in Some Sections of Track

6.3 Trending Analysis

6.3.1 Data Preprocessing

Because of GPS misalignment, data from different tests may not exactly coincide with each other in terms of milepost. Figure 6-11 shows the two sets of data from the same section of track. An offset exists between the two curves.

Measurements from two tests over approximately 0.05 miles of track are shown in Figure 6-11. The figure clearly shows that the measurements from both tests have similar shape. However, the two sets of data have an obvious horizontal offset. The offset represents errors in the milepost location associated largely with GPS error in localizing the data. Despite errors in GPS measurement, the shape of the curve is maintained because the relative GPS measurement (one data point with respect to the next) is much more accurate than two independent absolute GPS measurements.

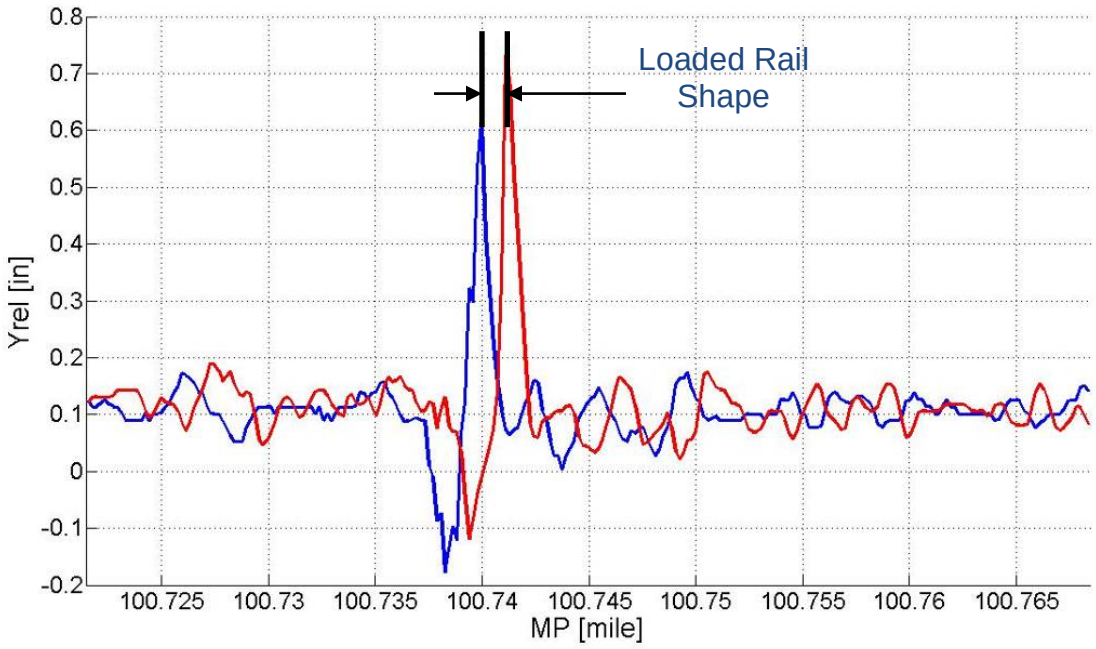

Figure 6-11. The Original Data from Two Tests

For the purpose of trending, it is desirable to remove the offsets so that relative comparisons can be made over short sections of track. The relative comparisons would evaluate one measurement relative to a previous measurement made at the same location at an earlier time.

To remove the offset in milepost, the cross-correlation function is introduced to mathematically quantify the offset. Cross correlation is a standard method of estimating the degree of correlation between two sets of measurements. Consider two series *x(i)* and *y(i)* both of length *N* where *i* = 0,1,2...N – 1. The cross correlation, $\hat{R}_{xy}$, at delay *m* is defined as :

$$\hat{R}_{xy}(m) = \frac{1}{N}\sum_{n=0}^{N-1} x(n)y(n+m) \qquad \text{Equation 6.3-1}$$

where *m* = –(N – 1),…,-2 –1,0,1,2,…,N – 1

For various values of *m*, $\hat{R}_{xy}$ is in the range $-1 \le \hat{R}_{xy} \le 1$. The bounds indicate maximum correlation, whereas 0 indicates no correlation. A high negative correlation indicates a high correlation but where one series is the inverse of the other series.

The results of applying the cross correlation function to the two series in Figure 6-11 at numerous values of *m* (between –100 and 100) is shown in Figure 6-12. This figure shows the cross correlation as a function of offsets. Clearly, the cross correlation reached a maximum when the offset was 8 ft. The value of the cross correlation at this offset is 0.8, indicating a high correlation between the data (this also suggests the measurements are highly repeatable).

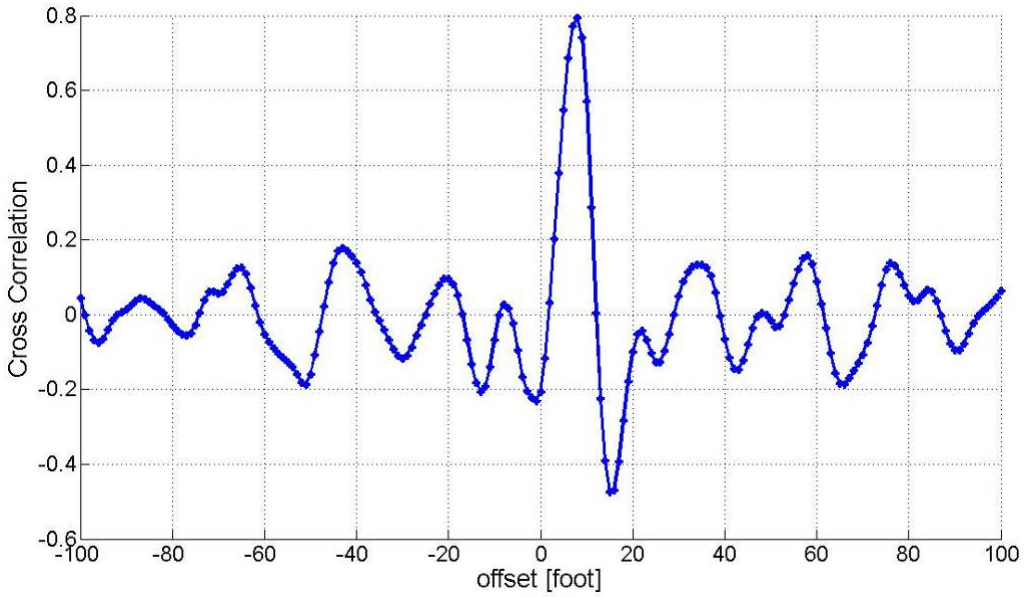

Figure 6-12. Cross Correlation

Based on the cross correlation plot, the second series in Figure 6-11 was shifted by 8 ft, and the new plot is shown as Figure 6-13. Now the two series of data line up well, which is helpful and convenient for further data comparison and analysis.

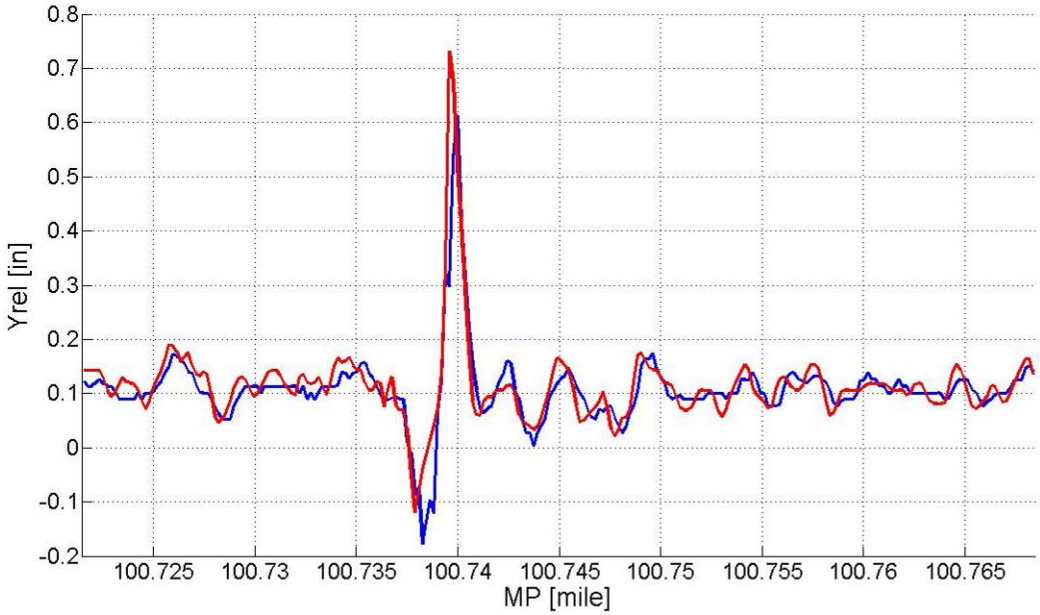

Figure 6-13. The Shifted Data from Two Tests

6.3.2 A Trending Example

Some trending results from the South Morrill subdivision are now presented. Several tests were conducted over the same approximately 160 miles of this subdivision at 3-month intervals. Figure 6-14 shows the relative deflection measurement (Yrel) over 0.1 miles of track from MP

A.70 to A.80 (exact mileposts are removed). Here, the third axis (into the page) illustrates the time interval between the tests in months. Figure 6-14 clearly demonstrates the changes in this section of track as a function of time. Specifically, two locations are singled out over time. It can be seen that MP A.76 is not changing quickly over time, whereas MP A.74 corresponds to a peak in the measurement (soft spot) that is increasing over time (becoming softer).

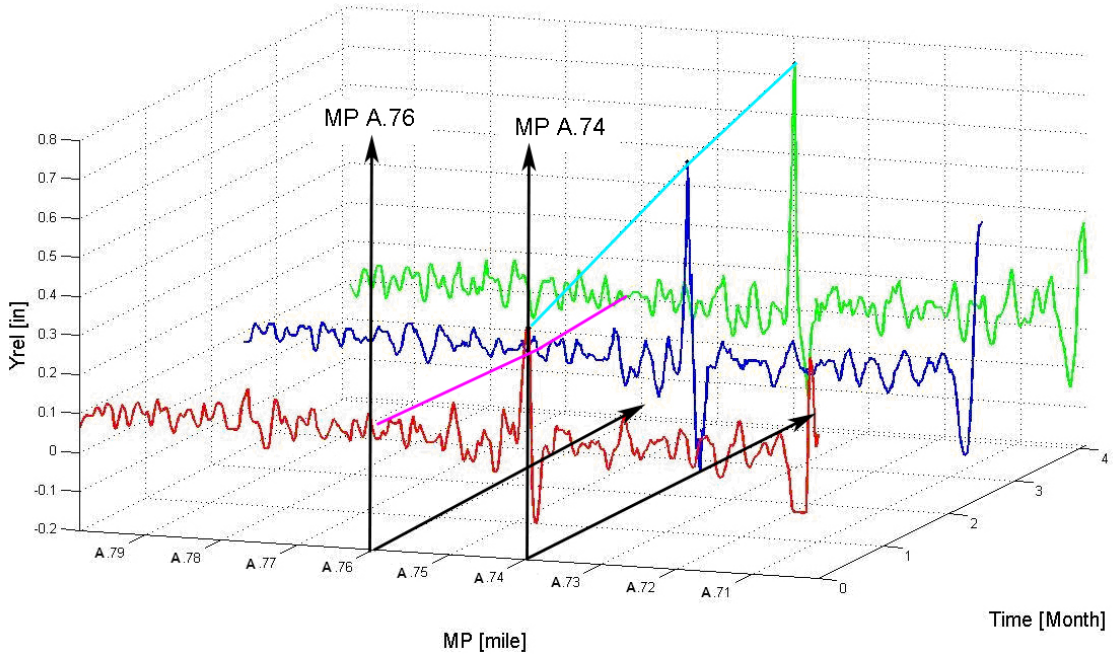

Figure 6-14. Data from Three Tests at MP A.74

From the measurements shown in Figure 6-14, two sections at MP A.74 and A.76 are extracted as an example and shown as a function of time in Figure 6-15. Since three tests were performed, three data points are shown in each of the plots for these milepost locations. Given this data, a prediction can be made based on the trends. In this case, a line is fitted to the data and used as the prediction. A correlation can be produced to indicate how well the line fits the three data points. Having only three points (three tests) of course may not accurately predict the trend and clearly the prediction has uncertainty. More testing will improve the prediction. With more available tests, it may be desirable to use other curves (rather than a line) to improve the prediction.

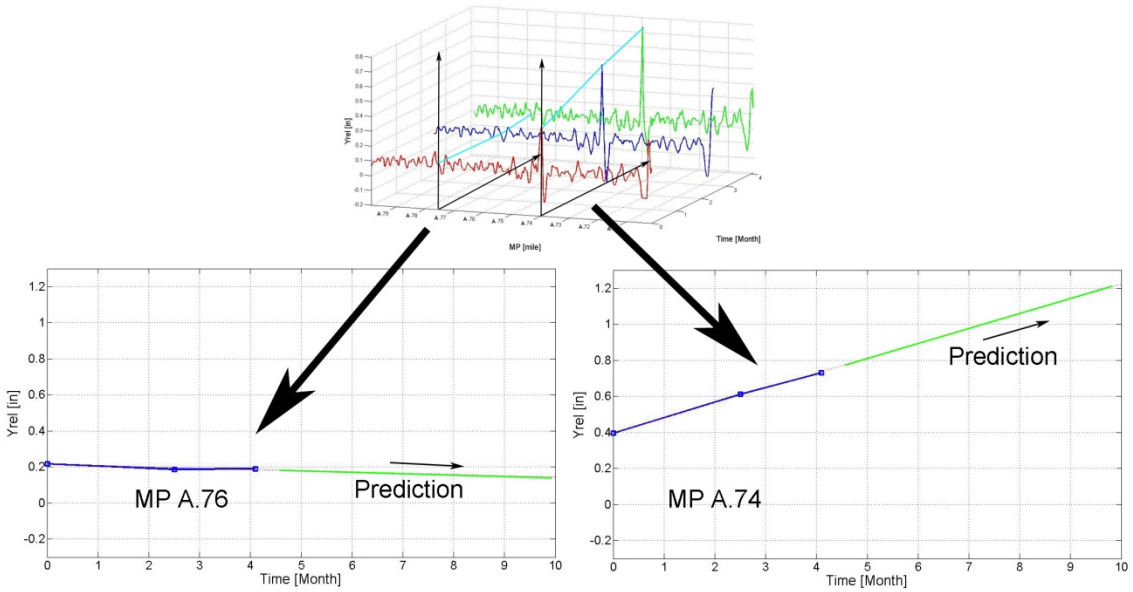

Figure 6-15. Trending at MP A.74 and A.76

To further illustrate the possible usefulness of this technique, MP A.74 is shown again in Figure 6-16. Here, an assumption is made that a given threshold of relative displacement, Yrel, would be undesirable. On the basis of the previous measurements, a value of 1.2 in is chosen and indicated by the red dashed line. Now, the linear prediction can be used to estimate the time required to reach this threshold. In this case, 5.5 months from the last test is the window for maintenance. The accuracy of this prediction is difficult to quantify; however, this is a tool that can be used to prioritize maintenance that is based on actual track data. It is also possible to apply this technique to other track measurements such as gauge, gauge restraint, cross level, and other standard measurements.

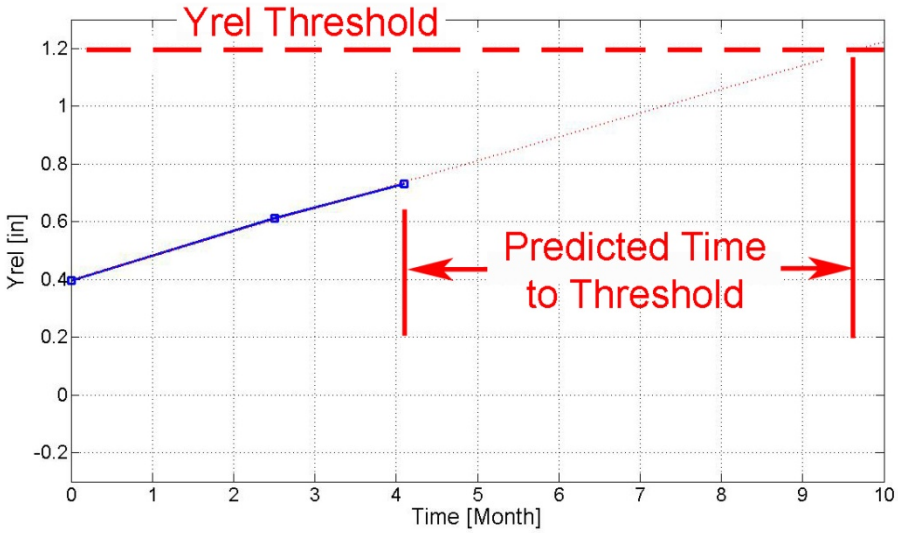

Figure 6-16. Test Data at MP A.74 as a Function of Time

The above approach can now be applied over the entire section of track between MP A.70 and A.80. This range is broken into 12-foot bin lengths, and a curve fit is created for each bin. The Yrel measurements are shown in Figure 6-17 for the three tests. A subplot is created that represents the slope of the trending line (linear curve fit in Figure 6-16). Here, the slope, given by $\frac{\Delta Yrel}{\Delta Time}$ in units of inches per month, is approximated as the difference between the two tests. When both differences are equal, it represents a linear change over time. The figure shows that MP A.74 is changing approximately linearly over time at a relatively fast rate, while the other part of the track in this section shows little change. The location of MP A.74 corresponds to a muddy road crossing, and the needed maintenance schedule can now be estimated (given some amount of uncertainty).

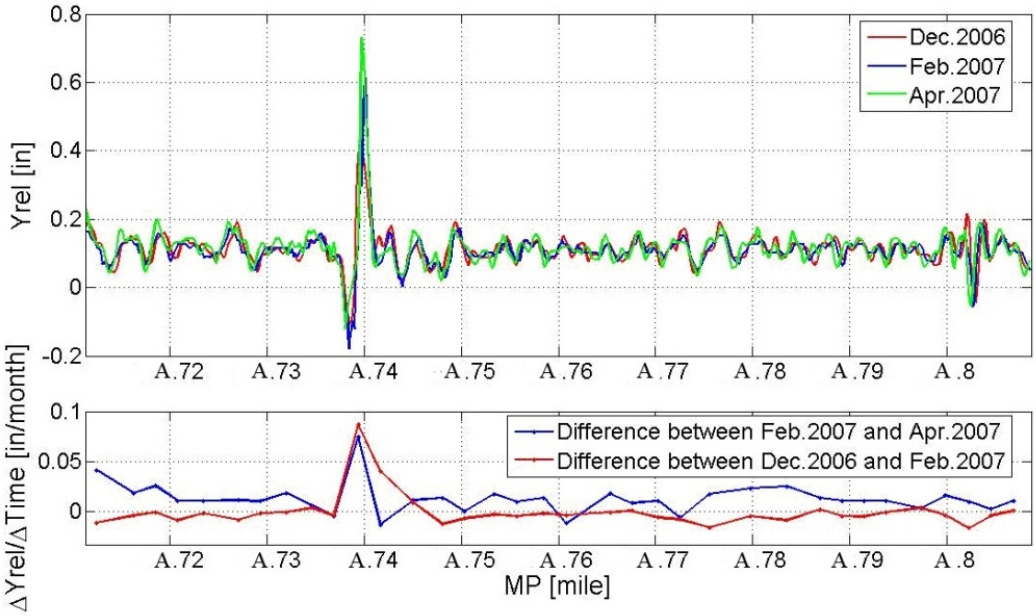

Figure 6-17. Trending from MP A.70 to A.74

6.4 Comparison between Different Measurement Systems

6.4.1 Comparison of VTD with Vehicle Track Interaction

A track quality measurement system known as vehicle track interaction (VTI) is currently in use by UPRR. This system has been successfully integrated into revenue service. The VTI system uses accelerometers mounted on various locations of a railroad vehicle to measure vertical accelerations. The system is used on both locomotives and hopper cars and has been fully integrated into revenue service with sophisticated communication and data processing infrastructure.

Results presented here are from a test conducted on a locomotive that passed over the same section of track (the Powder River and South Morrill subdivisions) 2 days after the vertical rail deflection measurements presented above (Section 5). The relevant VTI results come from an accelerometer mounted to the axle of the locomotive (below the suspension system). The

acceleration data is used (with knowledge of the locomotive's mass and suspension characteristics) to estimate loads between the wheel and rail.

The VTI measurements and the vertical deflection measurements are fundamentally different. For example, a smooth section of track with a low modulus will show no significant difference in VTI measurements as compared to a smooth section of high modulus track. However, this difference will be captured by the VTD system.

6.4.2 Comparison of Revenue Service Results from VTD and VTI

A test of the same section of track (270 miles of the Powder River and South Morrill subdivisions) was conducted using the VTI system on August 11, 2006—2 days after the VTD measurements were made. Some results of this test are shown in Table 6-1 as a comparison between the two measurements. Selections of the ranked results from VTI measurements are shown in the left four columns. The right two columns show how the same measurements appear in the deflection criterion exceptions. Only the locations common to both tables are shown in Table 6-1.

Table 6-1. Prioritized Exceptions of VTI Data

VTI Rank	MP	Acceleration (g)	Estimated Axle Force (lb_f)	Deflection (in)	Rank of Δ
1	X.5	28.15	104,500	NA	NA
:	:	:	:	:	:
5	G.97	24.97	84,800	0.828	7
:	:	:	:	:	:
27	J.58	27.27	69,650	0.083	10
:	:	:	:	:	:
62	B.89	27.78	64,600	0.89	2
:	:	:	:	:	:
123	A.47	22.09	59,000	1.424	1
:	:	:	:	:	:
249	C.97	17.1	52,300	0.973	3

The most important conclusion to reach from Table 6-1 is that the two measurements are fundamentally different. The highest force estimated from the VTI data (at MP X.5) does not appear in the top 12 deflection criterion exceptions. The top VTD exception (at MP A.47) appears at #123 in the VTI measurements. The two derailment locations described above appear on both lists (highlighted in both tables). The derailment that occurred 14 days after the vertical modulus measurements (MP B.89) appears as #2 on the VTD list and #62 on the VTI list. Similarly, the derailment that occurred 30 days after the test (MP J.58) was #10 on the VTD list and #27 on the VTI list. However, an enormous impact load at MP X.5 is not indicated in the

top 12 of the VTD measurements. Clearly, these are different, but complementary, measurements.

6.4.3 Comparison of Revenue Service Results of Yrel and ECO

The relation between Yrel and ECO has been explained in Section 3.4.2. Although high correlations exist between Yrel and ECO, they are fundamentally different measurements. Results from revenue service tests further confirm the fundamental differences.

A test was conducted on the South Morrill subdivision in April, 2007. The VTD system and UPRR's track geometry car (EC5) collected data over the same 160 miles of track on the same day. Exception lists were produced based on Yrel measurements and calculated ECO from the geometry cars space curve data.

Table 6-2 lists the top 20 locations in the VTD list along with their rankings in the ECO list. Among the sites, #4 and #17 in the list are the locations where a derailment occurred 1 week before the testing day. The track was under construction at these locations on the day of the test. The #1 item in the list is the location where another derailment occurred 2 weeks before the test. Again, the track was under construction on the day of the test.

It can be observed that nine of the top 20 sites in the VTD list did not show up on the ECO list (ECO list includes 200 sites). Besides the derailment locations, only four locations (#5, #9, #18, and #20 in VTD list) were identified by both top 20 lists. In addition, these locations rank differently on each list.

Table 6-2. Comparison between VTD and ECO (ranked by deflection)

VTD Rank	Deflection(in)	ECO Rank	ECO (in)	MP	Description
1	1.18	1	1.1954	58.813	Derailment reported
2	1.13	N/A	N/A	11.802	Unknown
3	1.06	N/A	N/A	93.489	Signal
4	1.02	4	1.02	105.106	Derailment reported
5	0.94	7	1.0196	56.286	Road crossing
6	0.92	N/A	N/A	14.37	Signal
7	0.9	N/A	N/A	9.628	Unknown
8	0.88	93	0.625	55.307	Road crossing
9	0.87	28	0.8514	115.447	RR XING
10	0.86	12	1.0038	23.102	Signal
11	0.85	N/A	N/A	38.938	Signal
12	0.84	N/A	N/A	116.774	Unknown
13	0.83	N/A	N/A	147.589	Unknown
14	0.83	NA	N/A	31.294	Signal
15	0.8	43	0.7383	39.228	Road crossing
16	0.78	N/A	N/A	100.149	Switch
17	0.76	25	0.8672	105.152	Derailment reported
18	0.76	9	1.0157	19.508	Road crossing
19	0.75	33	0.793	24.594	Road crossing
20	0.75	3	1.172	53.56	Road crossing

A list ranked by ECO data was also produced as shown in Table 6-3. In this table, 18 of the top 20 locations in the ECO list were also in the VTD list (VTD list includes 90 sites). However, most of these locations have lower rankings in the VTD list. Except for the derailment locations and five unknowns, almost all of the top 20 locations in the ECO list are road crossings.

Table 6-3. Comparison between VTD and ECO (ranked by ECO)

ECO Rank	ECO (in)	VTD Rank	Deflection (in)	Description
1	1.1954	1	1.18	Derailment reported
2	1.1406	33	0.61	Road crossing
3	1.1172	20	0.75	Road crossing
4	1.0976	4	1.02	Derailment reported
5	1.0351	48	0.58	Crossover Switch
6	1.0312	72	0.52	Unknown
7	1.0196	5	0.94	Road crossing
8	1.0196	29	0.63	Culvert
9	1.0157	18	0.76	Road crossing
10	1.0156	22	0.7	Road crossing
11	1.004	82	0.51	Road crossing
12	1.0039	10	0.86	Road crossing
13	1.0001	81	0.51	Unknown
14	0.9961	46	0.58	Unknown
15	0.9687	56	0.55	Road crossing
16	0.9649	52	0.57	Road crossing
17	0.9414	59	0.55	Unknown
18	0.9336	N/A	N/A	Road crossing
19	0.9218	30	0.63	Unknown
20	0.8828	N/A	N/A	Road crossing

6.5 Field Investigations

The VTD measurement system conducted a test in a coal train consist at the South Morrill subdivision in June 2008. About 1 month earlier, UPRR's EC5 geometry car collected track geometry data on the same subdivision. The track geometry data provided by UPRR was then implemented into the system's Yrel measurements so that Yrel and ECO measurements could be compared and relative deflection measurements could be calculated.

On the basis of both the proposed criterion and the calculated relative deflection measurements, 15 sites were selected, and field investigations were completed on July 1, 2008. The track visits identified the reasons for large Yrel and deflection measurements at all sites with varying levels of maintenance urgency. Among them, one site was taken out of service immediately, and two additional sites were scheduled for maintenance. A variety of track problems were identified including poor joints, broken ties, muddy ballast, and crushed rail head, etc. Some of the sites will be discussed in detail in the following sections. The actual mileposts for these sites are concealed in the discussions.

6.5.1 Site 1: A Crushed Rail Head

The data from the first site is plotted in Figure 6-18. The peak in the Yrel data on the north rail measures 0.89 in, whereas the ECO measurement is 0.34 in. As a result, the relative deflection is calculated as 0.55 in.

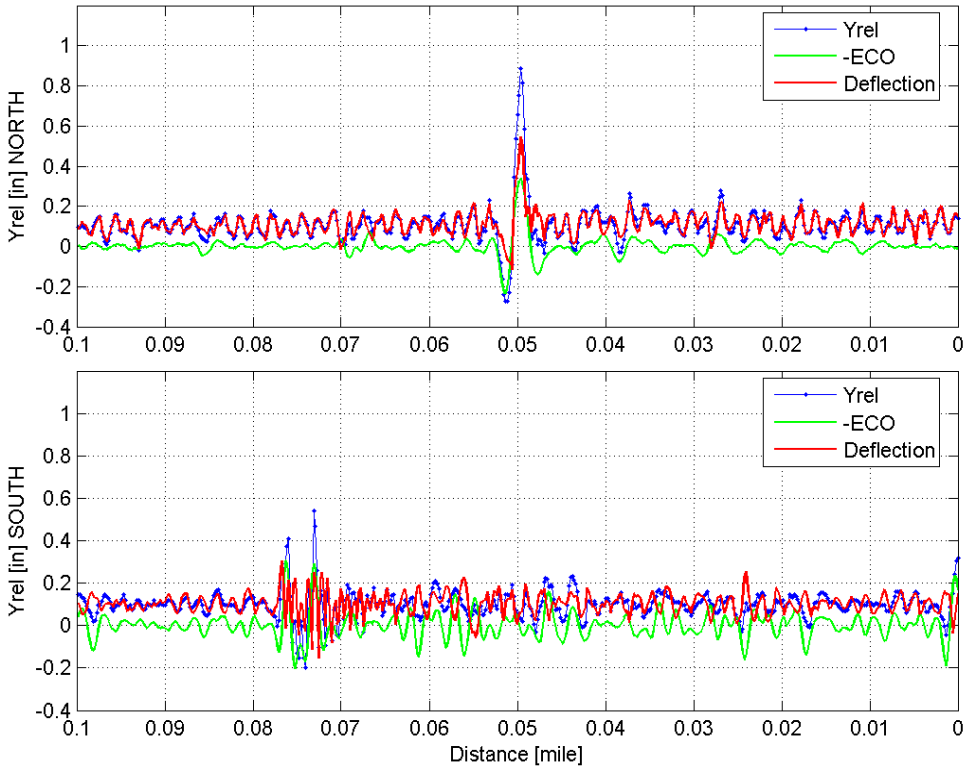

Figure 6-18. Data at the Crushed Rail Head Site

The pictures of this location are displayed in Figure 6-19. The white-colored ballast indicates that strong pumping has occurred. The track director estimated the pumping to be up to three-

quarters of an inch. The rail profile dropped down one-half inch at the crushed spot. This site was investigated 2 weeks after the test. The track director suggested that the weather was damp, and a flash flood warning was issued around the testing time so that the deflection was expected to be large.

Figure 6-19. A Crushed Rail Head

Although the large track deflection itself would not be expected to crush a railhead, the dynamic wheel load and increased rail stress tend to expose any potential weakness. If the rail would tend to fail by railhead crushing, then the additional stress at the large track deflection location will expose this tendency faster than in other track locations.

6.5.2 Site 2: A Muddy Crossing

A number of road crossings are listed in the VTD exceptions list. Most of them exhibited fouled ballast and broken ties. Data from one particular site is shown in Figure 6-20. On both of the south and north rails, two peaks of Yrel data may be observed. They represent the two approaches to the road crossing. The approach at the east side of the crossing appears to be much worse than the west side based on the Yrel data. The deflections at both rails on the east approach are almost 0.6 in.

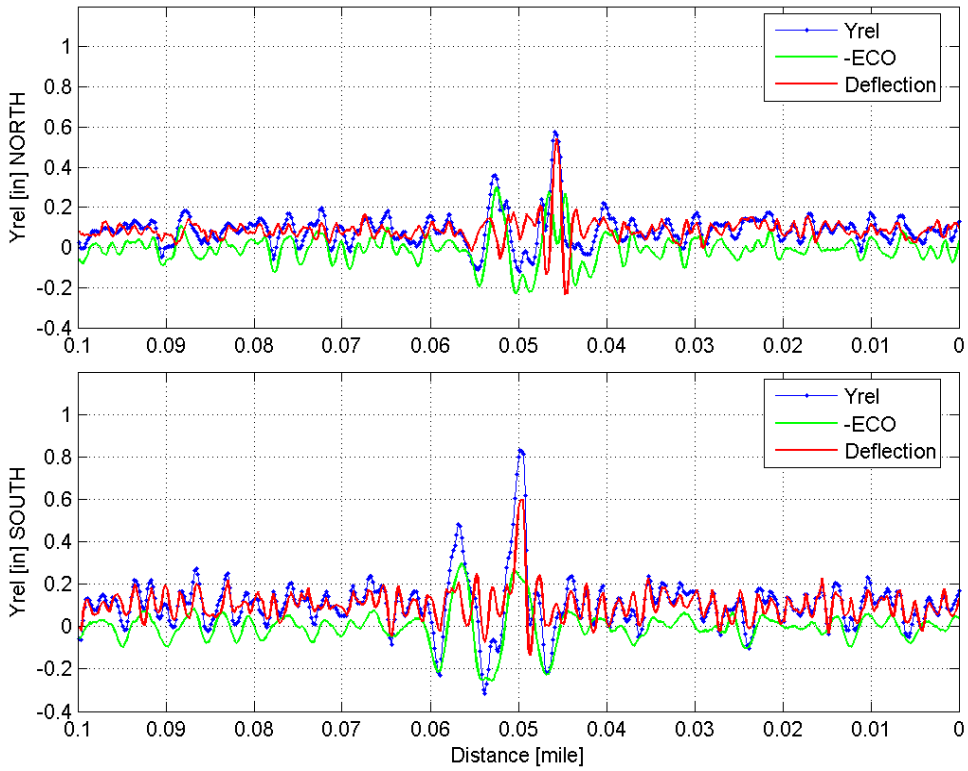

Figure 6-20. Data at the Muddy Crossing Site

At least four ties were center cracked, and some of them appeared to have horizontal cracks at the bottom. The muddy ballast and the tie cavities indicated large movements of the ties. On the basis of this observation, the ties were estimated to have moved by over 0.5 in. This muddy area was located at an approach to a road crossing. The other side of the road crossing was also muddy. This explains the two peaks in the Yrel data. Again, the track was much wetter on the day of the test.

Figure 6-21. The Muddy Crossing

6.5.3 Site 3: A Failing Joint

Approximately half of the sites in the VTD exception list are joints. The measurement system demonstrated a notable ability to identify poorly supported joints, which often deteriorate rapidly once the joint begins to deflect substantially. Figure 6-22 shows the data at one particular joint. In this case, Yrel measured 1.21 in at the joint with an ECO reading of only 0.3 in. Therefore, the deflection is over 0.8 in.

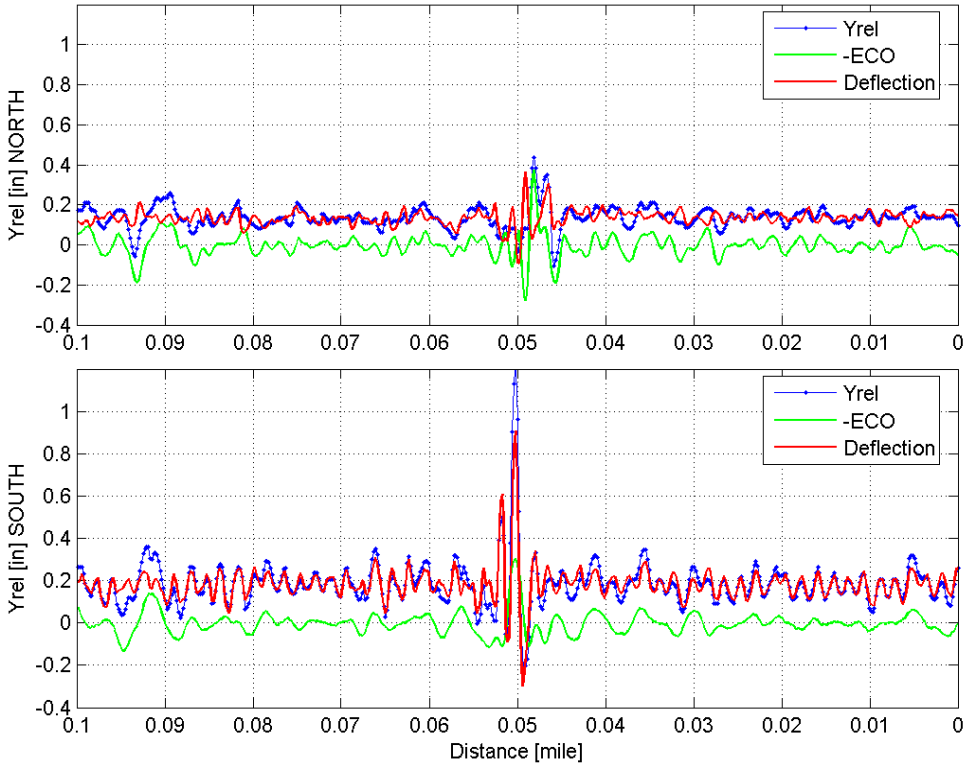

Figure 6-22. Data at the Failing Joint Site

Figure 6-23 shows the condition of the insulated joint. This supported joint is rare in North America where suspended joints are dominant. The supporting tie in the center was in a very poor condition. The tie was split, and a large portion (left part in the picture) was nearly separated from the rest of the tie. Applying pressure with a foot was enough to deflect the tie. The bolts on the joint bars were loose, and one of them would actually rotate as a train passed. The track director commented that this joint was probably among the worst 10 percent of all joints. A wayside camera measurement was taken as a coal train passed the site. The video showed that the deflection at the joint was over 1.2 in under the loads of the locomotives.

Figure 6-23. The Failing Insulated Joint

6.5.4 Site 4: A Series of Broken Ties

The peak in the Yrel data from this site reads 0.95 in, whereas the ECO is 0.41 in. The site is located on a portion of tangent track with no joints or crossings. Field measurements of the mid-chord offset were consistent with the geometry car measurements. As shown in Figure 6-24, the curve of Yrel data from this site has a special shape when compared with the data from other sites. Unlike the sharp peaks in Figure 6-22, the peak here is broader, and high deflections occurred over a relatively long distance.

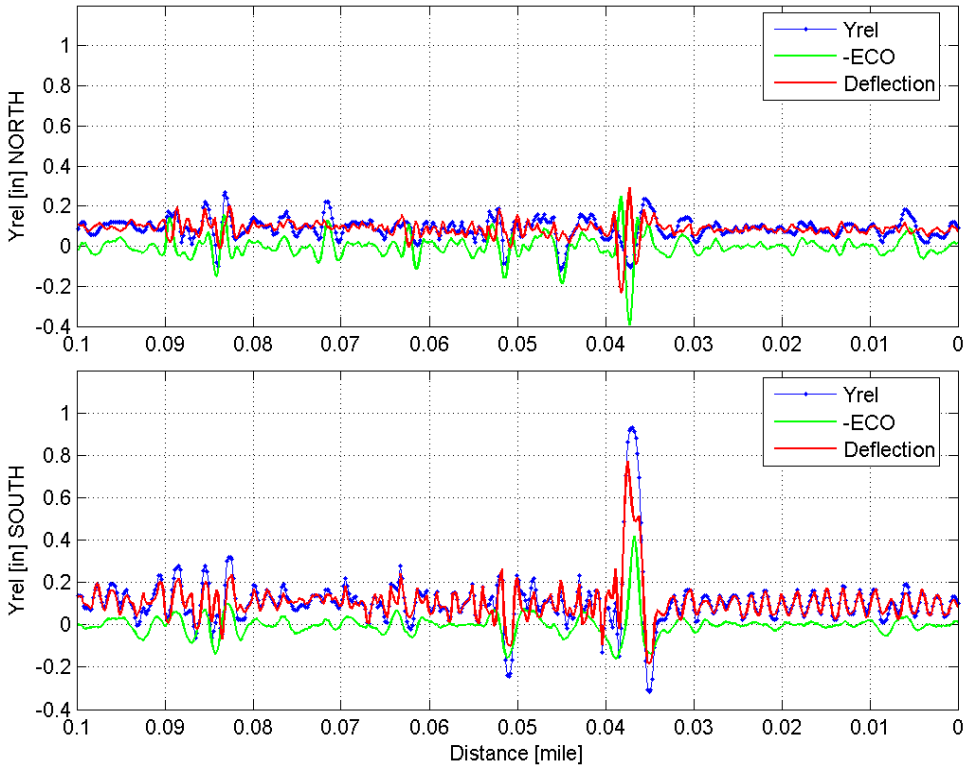

Figure 6-24. Data at the Broken Ties Site

A picture of this site is displayed in Figure 6-25 in which a series of broken ties are clearly visible. The ties barely constrained the south rail. The clips were either missing or unattached to the rail because of the cracks in the ties. The broken parts of the ties could easily be lifted by hand. Recent geometry car tests and VTI tests did not identify an exception at this location. The track director explained that defects like these were difficult for track inspectors to notice. The track director immediately stopped service on the track as shown in Figure 6-26.

This location is one of several sites where measurements from acceleration-based systems do not indicate as significant a reading as measurements by the VTD system (i.e. Yrel >> ECO). The track support conditions where the VTD measurement does not match measurements from other systems are extremely complex. The track behavior in these locations does not follow traditional models and will require site specific observations to fully understand the complex track mechanics leading to the large deflection associated with the Yrel measurement. More importantly, these locations are potentially the most significant locations of track performance problems observed during this research project. To evaluate the track conditions in site inspections associated with this project, many sites were selected where Yrel was larger than ECO. In every instance a specific failure in a track component was identified ranging from cracked and broken ties, to poorly performing switches, to poorly supported joints. These all represent track support related deterioration that is a risk to track safety, but that are not explained using simple track deflection models like beam on elastic foundation theory or even generalized finite element solutions.

It should also be noted that there are several locations where a significant reading is obtained from acceleration-based measurement systems and the VTD system does not show significant

relative deflection. Follow-up visits to these sites confirmed that the track condition was reasonably good and confirmed the Yrel measurement, but raised questions about how to threshold the acceleration data. This confirms the general challenge of thresholding acceleration-based measurements and the associated problems with attempting to interpret acceleration data in terms of deflection or load.

The authors feel it is important to further understand track locations where Yrel values significantly exceed associated ECO. Data that have been associated with the potential for track deterioration should be evaluated to more fully understand the track conditions and associated safety risks. This will require more detailed follow up during site visits to make careful measurements of track, component, support conditions, and, perhaps, instrumentation.

Figure 6-25. Six Broken Ties in a Row

Figure 6-26. Track Taken Out of Service

6.6 Analysis of Bridge Approaches

Further analysis has been made of certain bridges and at-grade road crossings where changes in track stiffness have been problematic. As stated above, the use of track modulus can be problematic because the term is only well defined in situations of linear and uniform track support. Real track is always nonuniform and nonlinear, and therefore, modulus is a difficult term to define. However, modulus is an often used in the rail industry and can be useful in discussions as in the analysis here. Given this, changes in track deflection are discussed below, but these deflections are also related to modulus measurements. The values of modulus are not accurate absolute numbers but instead provide insight and are useful when compared in a relative sense (e.g., how much higher or lower is the modulus on the bridge when compared with the neighboring tangent track or the approach).

To make relative comparisons, modulus values are taken from Kerr (2003). These estimates are shown in Table 6-4.

Table 6-4. Modulus Values from Kerr (2003)

Track Condition Description	Modulus (psi)
Wood-tie track, after tamping	1,000
Wood-tie track, compacted by traffic	3,000
Concrete-tie track, compacted by traffic	6,000

Wood-tie track, frozen ballast and subgrade	9,000

On the basis of a relative deflection measurement from Yrel measurements and ECO measurements, the deflection can be translated into a modulus value using the values from the above table. For example, the difference between wood and concrete ties can be seen in Figure 6-27. Here, the relative deflection measurement, when averaged over long distances (1/2- to 1-mile segments), shows a significant deflection difference using the two types of ties.

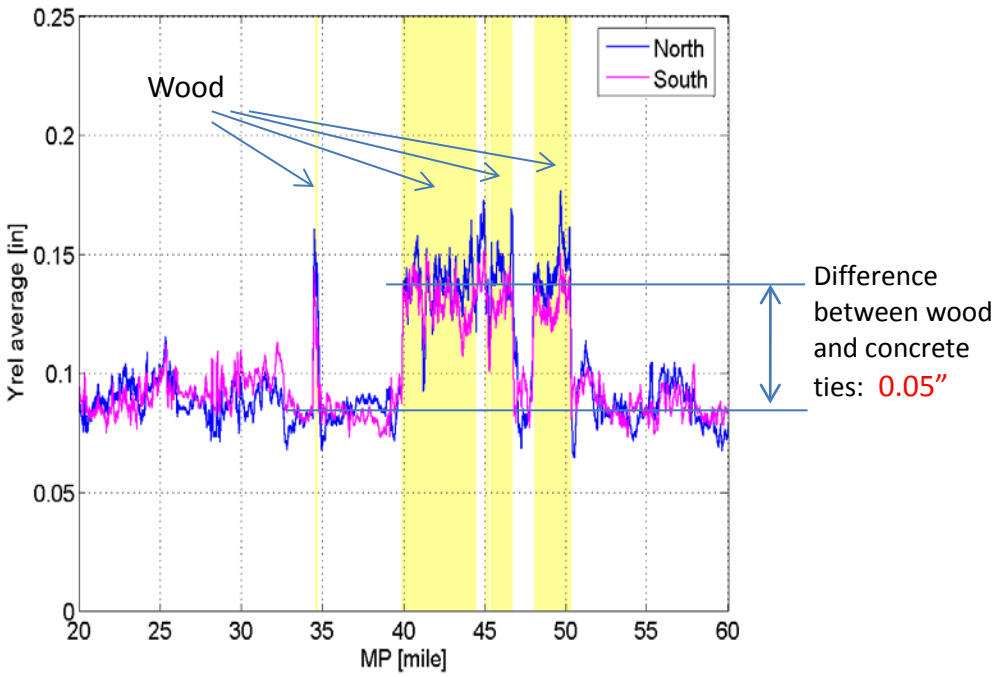

Figure 6-27. Deflection Change Between Wood and Concrete Ties

The first site described here is a concrete box culvert. This culvert has pads bonded to the bottom of the concrete tie over the culvert in an attempt to better match the culvert vertical stiffness to that of the surrounding track. The relative deflection measurements (difference between Yrel and ECO) are shown in Figure 6-28 and summarized in Table 6-5. Here, it can be seen that the deflection over the culvert is on the order of 0.145 in, and the deflection of the surrounding track is lower (maybe 0.105 in). The change in deflection is approximately 0.04 in. This means that the culvert is less stiff than the surrounding track. Again, interpolating from a relative comparison based on the Kerr estimates (Table 6-4), this suggests a culvert modulus of ≈4,400 psi and the culvert is ≈1,600 psi softer than surrounding track.

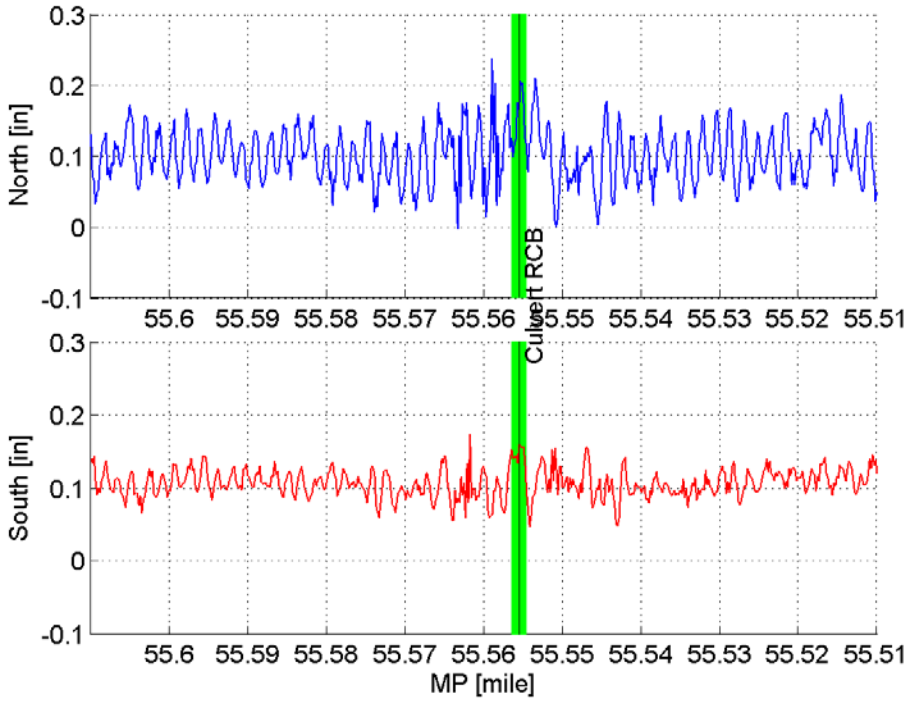

Figure 6-28. Concrete Boxed Culvert

Table 6-5. Average Deflection over and around Culvert

	Average Deflection over 0.1 mile surrounding culvert (in)	Average Deflection over the Culvert (in)	Increment (in)	
South Rail	0.101	0.148	0.047	} δDeflection ~0.04 in
North Rail	0.106	0.142	0.036	

The second site described here is a three-span bridge. This bridge has a "ballast mat," bonded to the steel deck pan of the bridge (under 12 in of rock) in an attempt to better match the bridge vertical stiffness to that of the surrounding track. The relative deflection measurements (difference between Yrel and ECO) are shown in Figure 6-29 and summarized in Table 6-6. Here it can be seen that the deflection over the bridge is on the order of 0.095 in and the deflection of the surrounding track is lower. The change in deflection is approximately 0.02 in. This means that the bridge is less stiff than the surrounding track. Again for a relative comparison based on the Kerr estimates, this suggests a bridge modulus of ≈5,200 psi and the culvert is ≈800 psi softer than surrounding track (again, interpolating from Table 6-4).

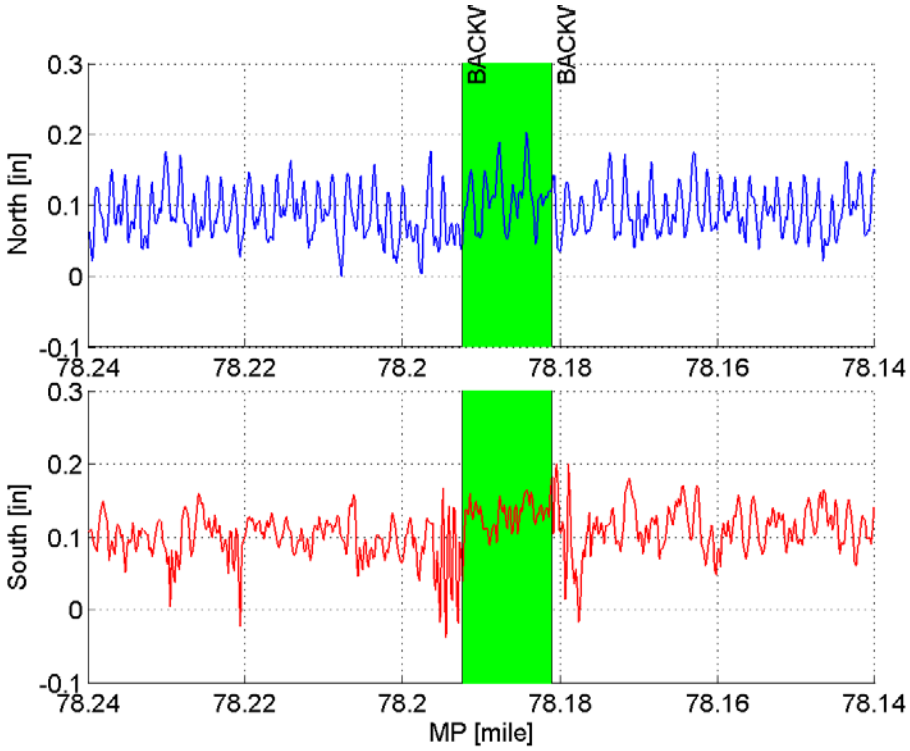

Figure 6-29. Three Span Bridge

Table 6-6. Average Deflection over and around Three-Span Bridge

	Average Deflection over 0.1 mile surrounding bridge (in)	Average Deflection over the bridge (in)	Increment (in)	
South Rail	0.091	0.110	0.019	} δDeflection ~ 0.02”
North Rail	0.097	0.119	0.022	

6.7 Identifying Thresholds for Maintenance

The above analysis and field observations are summarized here as a beginning toward understanding how to interpret the measurements and how to use this knowledge to better schedule maintenance operations. The discussion presented here is empirical and preliminary.

At each of the site visits, host railroad experts provided interpretation of the location and the priority for a maintenance action at the site. These were categorized as red, yellow, or green with red representing an immediate maintenance concern that should be attended to in a short time, and green meaning it is not an immediate maintenance concern with yellow in-between. An example of a test from June 2008 on UPRR is shown in the table below.

Table 6-7. Maintenance Summary

MP	DESCRIPTION	DEFLECTION
A.971	very bad joint, worst 5% of all joints in NPSU	0.91
B.906	pumping joint, but not immediate concern	0.807
C.942	temp fix where rail was cut out, needs work soon	0.79
D.279	big pumping, failing joints	0.725
E.878	Deland: "joint looks like #$%$#" – will replace within 30 days	0.683
F.961	Deland called nearby crew, temp fix where rail was cut out	0.66
G.138	pumping joint, but not immediate concern	0.606
H.054	very muddy crossing-probably much worse during rains when measurements were taken	0.59
I.948	bad joint, loose bolts	0.58
J.04	pumping joint, but not immediate concern	0.57
K.29	crushed head at weld, pumping 3/4 in, probably much worse during rains when measurements were taken	0.545
L.24	taken out of service immediately – data a different shape	0.54
M.458	pumping joint, but not immediate concern	0.496
N.703	has recently been repaired – trending site	0.4082

A second summary from a two different tests on both wood and concrete track and on two host railroads is shown in Figure 6-30. Here, the red, yellow, and green dots each represent a site. The sites are plotted by the magnitude of Yrel and show that most of the red locations have a larger Yrel measurement and most of the green sites have a lower measurement.

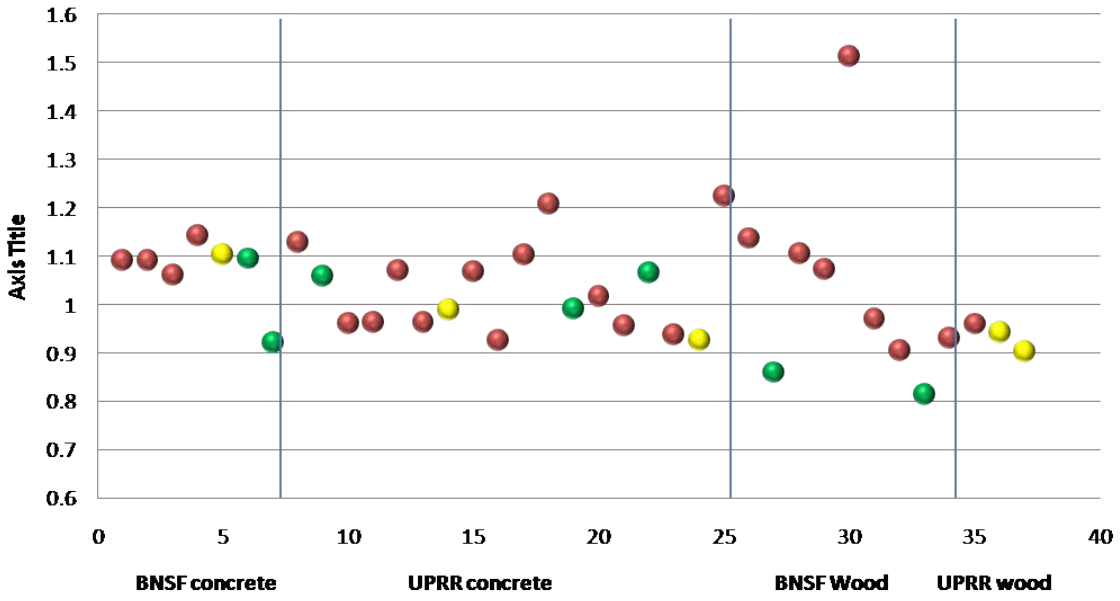

Figure 6-30. Summary of Maintenance Priority of Sites

These results are again extremely preliminary. A problem with the presentation in Figure 6-30 is that it does not show sites that correspond to good track conditions with low Yrel readings. This is because few good sites were visited since the goal of the visit was to identify track conditions at locations of high Yrel to determine whether maintenance or other problems existed. Small Yrel readings represent the majority of the Yrel data, and it is strongly believed that the numerous green dots that this would add at the bottom of this figure would make a strong distinction between green and red to better select a threshold.

Even though this analysis is not yet complete, it does suggest that high Yrel readings and high deflection readings are less desirable. Any future guidelines may include thresholds for wood and for concrete as well as for deflection and for Yrel readings (and of course class of track).

Another exception is that the criteria being proposed and have been used above (Section 6) are the deflection defined by the difference between Yrel and ECO. A table similar to that above can be made using these criteria.

For the measurements shown above, an extremely preliminary suggestion might be that deflection measurements greater than 0.6 in might represent a significant concern (5 of 7 as red in the measurements above) and small measurements would be less of a concern (5 of 7 not red in the measurements above). For Yrel, it might be suggested that measurements greater than 0.9 in (25 of 34 being red) or 1 in (15 of 19 being red) might represent a significant concern with lower readings being less of a concern (2 of 2 not green with readings less than 0.9 in).

Several other site visits have been made (~200) but these are summarized here. Clearly, more work needs to be done to solidify these thresholds.

7 Finite Element Analysis from System Perspective

As described earlier, several analytical models have been developed for use in railroad track design and to characterize the track response under load. Despite the usefulness of some of these models, they lack the complexity needed to fully characterize real track. Most of these models assume uniform support from homogeneous materials, whereas evaluation of problematic track conditions most often occurs in locations of track support variations with variable materials properties. Advancements in finite element analyses (FEA) have provided more realistic representations of the track response. These FEA programs often need to be formulated with a specific objective to minimize computational costs. Therefore, a FEA program suitable for solving one problem may not adapt well to another goal.

Custom FEA programs offer realistic solutions to well-defined problems. One particular FEA program titled GBEAM was developed to better understand track dynamics (Carr, 1999). This program analyzed the motion of a single mass rolling along the track. The track was modeled as a Euler beam resting on a damped, elastic foundation. The results highlighted the importance of measuring track deflection and concluded that track dynamics become important in high-speed simulations (Carr, 1999).

The following sections describe the development and results of a new custom FEA program created to characterize track response from the perspective of the UNL system. Nonlinear foundation characteristics are examined with the commercial FEA software, ALGOR®. The purpose of this analysis is to provide better understanding of the data collected by the UNL system. Improved evaluation of this data would enhance its potential as a resource for maintenance planning.

7.1 FEA Model Development

7.1.1 FEA Objectives and Specifications

The main objective of the FEA analysis in this report is to characterize track response based on the track characteristics that influence the output of the UNL measurement system. This system measures the vertical deflection of the track from a moving reference frame attached to a three-piece truck on a modified hopper car. Variations in the track support and in short-wavelength track geometry affect the UNL measurement. Understanding how these track characteristics relate to the UNL data is important for interpreting the data with the goal of improving maintenance planning.

The UNL system, described previously yields relative track deflection data defined as Yrel. This measurement is used in conjunction with a 10-foot ECO calculated from the vertical track geometry rail profile to compute the track deflection that can identify areas of poor track support. The difference between Yrel and ECO is used as one exception criterion for identifying locations needing further inspection (Lu, 2008). This criterion is used along with relative thresholds for the magnitudes of the Yrel and ECO measurements.

Certain track locations yield identical shapes and magnitudes for both Yrel and ECO as shown in the top of Figure 7–1. Other locations result in large peaks in Yrel data with relatively minor

ECO peaks as illustrated in the bottom of Figure 7–1. This phenomenon is frequently observed in the UNL measurements. Corresponding site visits have shown in almost every case a problematic track support condition or identification of a track defect. Since the source of track support irregularities are generally below the surface, the surface inspection of track involves identification of clues as to the surface manifestation of subsurface problems. In locations where no surface clues are obvious, observation of track load-deflection behavior under passing trains generally shows the nonuniform support that the UNL measurement indicated even though the subsurface failure had not yet progressed to the surface.

It is believed that these special locations have significantly complex track behavior and that FEA analysis, including the work presented here, can help improve the understanding of these locations. However, additional field tests and site visits will also be needed to fully understand the risks associated with these locations.

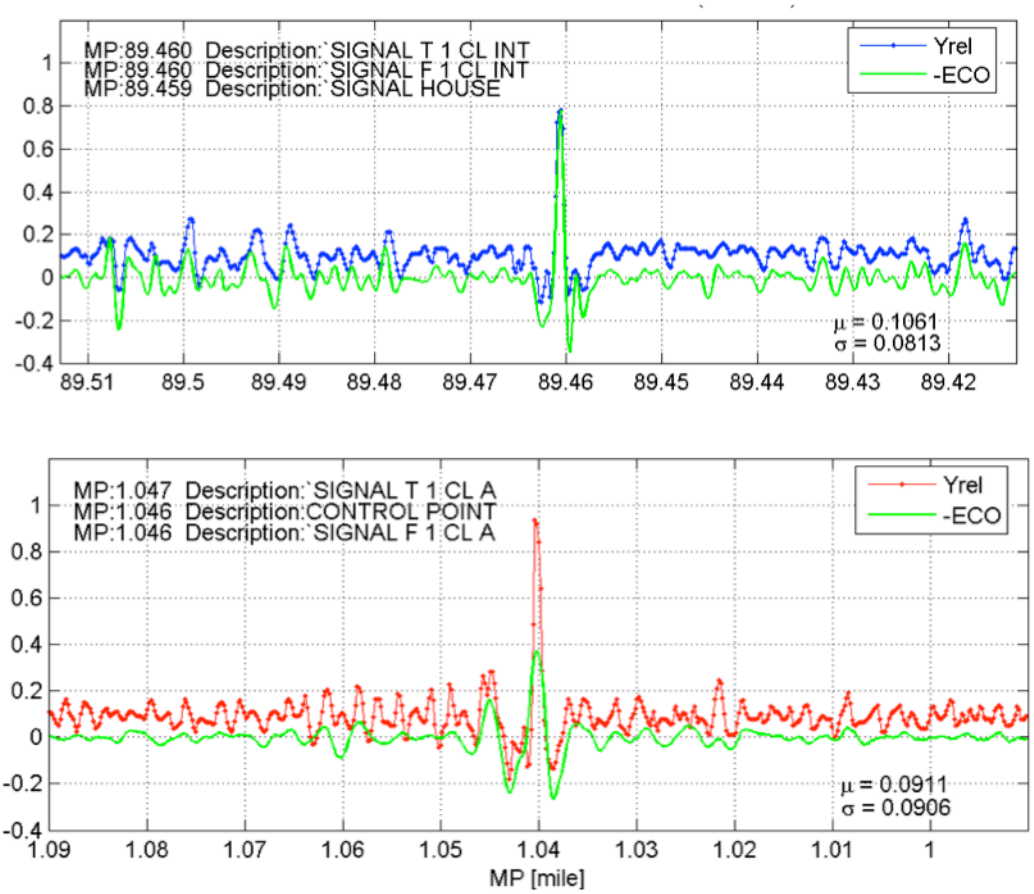

Figure 7-1. Different Shapes in Yrel and ECO Data

Using the FEA program to characterize the track response based on the Yrel and ECO measurements may provide insights into which track features lead to certain measurement results and will be particularly useful for locations where the surface manifestation is limited and might provide the opportunity to conduct preventative maintenance that might otherwise be impossible to efficiently specify. For example, different combinations of poor track support, poor track geometry, and failing joints may lead to either case shown in Figure 7-1 as well as intermediate

situations. Therefore, the particular program developed should have the ability to vary each of these items individually and analyze the corresponding effects on the UNL measurement results.

Several specifications simplify the structure and focus of the FEA program. The FEA program assumes a Winkler foundation. However, the program allows for variation in support modulus along the track. More complicated, nonlinear foundations are examined with ALGOR®. The model is constructed in two dimensions and considers only one rail. Fixed boundary conditions are used, and the length of the model ensures that the boundaries do not affect the deflection results. The dimensions correspond to a standard coal train traveling over 132-pound rail. The elements are only 1 inch in length so that enough nodal deflections are calculated to reproduce the Yrel measurement. Dynamic effects are ignored, and the deflections needed to reproduce the Yrel data are obtained using a quasi-static approach.

7.1.2 Governing Equation and Program Development

The assumption of a Winkler foundation leads to the governing differential equation defined in earlier sections. This equation is rewritten in a form more suitable for the derivation of the necessary finite element equations as displayed in Equation 5.1-1. The equation represents a beam supported by a series of continuous, independent springs. Equilibrium of a differential length of the beam yields:

$$\frac{d^2}{dx^2}\left(EI\frac{d^2w}{dx^2}\right)+uw-q=0 \qquad \text{Equation 5.1-1}$$

The derivation of the finite element equations follows a variational formulation based on the principle of minimum potential energy and the calculus of variations. The following simplifying techniques based on the method in Thompson (2002) are used in the derivation:

1. The governing equation is placed in its "weak" form (from the calculus of variations) rather than directly into the potential energy functional.
2. The general element approximating functions are defined by a local coordinate system with the origin at the element's left end.
3. Equations and calculations are completed in matrix notation more suitable for programming.
4. Known boundary values are included in the calculations as if they were unknowns and only accounted for after the final matrix equation is created.

The governing equation defined in Equation 5.1-1 requires that the fourth derivative of *w* exists. In order to reduce these requirements, the equation is placed in its weak form giving:

$$\int_0^L \delta w\left[\frac{d^2}{dx^2}\left(EI\frac{d^2w}{dx^2}\right)+uw-q\right]dx=0 \qquad \text{Equation 5.1-2}$$

where δw represents a small variation in w

L is the length of a general element

Placing the governing equation in its weak form reduces the requirements for higher order derivatives in the solution. Integrating by parts twice and substituting the expressions for shear and moments found in elementary beam theory yields Equation 5.1-3 (Thompson, 2002).

$$\delta w_L V_L - \delta w_O V_O - \left(\frac{d\delta w}{dx}\right)_L M_L + \left(\frac{d\delta w}{dx}\right)_O M_O + \int_0^L \left\{\left[\frac{d^2\delta w}{dx^2} EI \frac{d^2 w}{dx^2}\right] + \delta w k w - \delta w q\right\} dx = 0 \qquad \text{Equation 5.1-3}$$

where

$$M = EI\frac{d^2 w}{dx^2} \qquad \text{Equation 5.1-4}$$

$$V = \frac{d}{dx}\left(EI\frac{d^2 w}{dx^2}\right) \qquad \text{Equation 5.1-5}$$

On the basis of the weak formulation of the governing differential equation, only the second derivative of *w* is required to exist, as illustrated by Equation 5.1-3. The condition for existing second derivatives requires that the approximating shape functions be continuous and have continuous first derivatives. Hermite cubics are used as the approximating functions to accomplish these objectives. Each function is defined in terms of the nodal values for *w* and *dw/du* at the ends of each element. These functions are expressed in terms of their Gaussian coordinates as displayed in the following equations.

$$N_1 = \left(\frac{1}{4}\right)(u+2)(u-1)^2 \qquad \text{Equation 5.1-6}$$

$$N_2 = \left(\frac{1}{4}\right)(u+1)(u-1)^2 \qquad \text{Equation 5.1-7}$$

$$N_3 = -\left(\frac{1}{4}\right)(u-2)(u+1)^2 \qquad \text{Equation 5.1-8}$$

$$N_4 = \left(\frac{1}{4}\right)(u-1)(u+1)^2 \qquad \text{Equation 5.1-9}$$

where: *u* defines the Gaussian coordinates

With respect to the nodal values and matrix notation, the approximation becomes:

$$w(u) = \lfloor N_1(u) \;\; N_2(u) \;\; N_3(u) \;\; N_4(u) \rfloor \begin{Bmatrix} W_a \\ dW_a/du \\ W_b \\ dW_b/du \end{Bmatrix} \qquad \text{Equation 5.1-10}$$

where: *a* and *b* represent the left and right nodes, respectively

u defines the Gaussian coordinates

Gaussian coordinates are used since Gaussian quadrature is the numerical integration method used to solve the finite element equations. Gaussian quadrature is a method of determining an

integral by using a weighted average of the integrand evaluated at specific sampling points (Thompson, 2002). In this case, four-point Gaussian quadrature is used since four points are needed to exactly integrate a cubic polynomial.

The approximating shape functions are depicted graphically with respect to the Gaussian coordinates as shown in Figure 7-2.

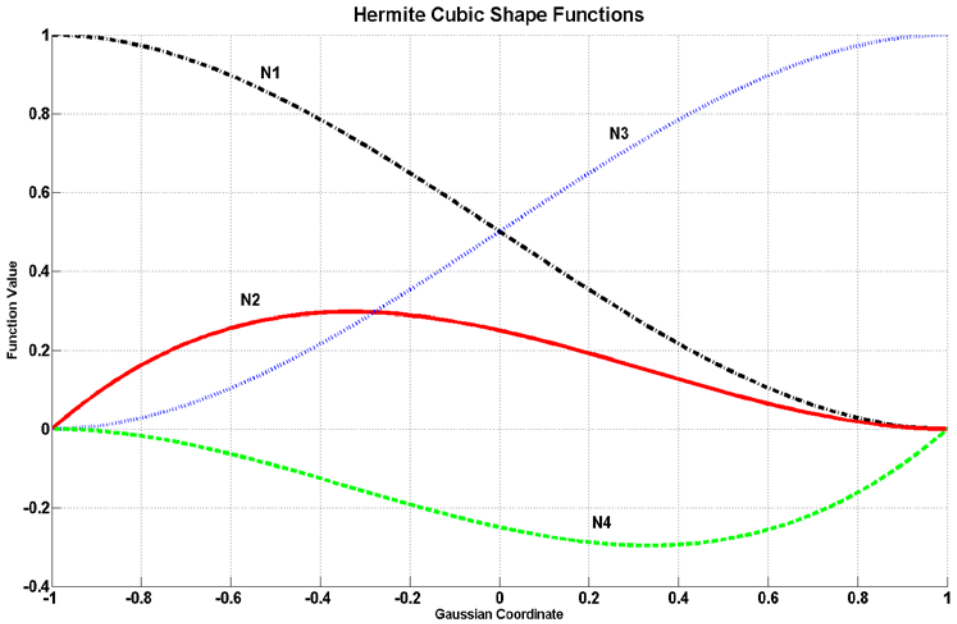

Figure 7-2. Hermite Cubic Shape Functions

Since the shape functions are expressed in Gaussian coordinates, the integration limits of ±1 do not correspond with the *x*-axis of the elements. A change of variables is needed to map the functions and their derivatives into the *x*-axis of the element coordinate system. This mapping is completed with the following linear transformation:

$$x = \left(\frac{a+b}{2}\right) + \left(\frac{b-a}{2}\right)u \qquad \text{Equation 5.1-11}$$

$$dx = \left(\frac{b-a}{2}\right)du \qquad \text{Equation 5.1-12}$$

$$du = \left(\frac{2}{b-a}\right)dx \qquad \text{Equation 5.1-13}$$

where: a and b represent the left and right nodes, respectively

u represents the Gaussian coordinates

The actual transformation for each shape function and its derivatives is formulated by Thompson (2002) and used in the FEA program code. The solution and its variation can then be expressed in terms of the shape functions as follows:

$$w = \lfloor N \rfloor \{W\} \qquad \delta w = \lfloor N \rfloor \{\delta W\}$$
$$w' = \lfloor N' \rfloor \{W\} \qquad \delta w' = \lfloor N' \rfloor \{\delta W\}$$
$$w'' = \lfloor N'' \rfloor \{W\} \qquad \delta w'' = \lfloor N'' \rfloor \{\delta W\}$$

Equation 5.1-14

where: W and δW represent the arrays of nodal values

Substituting the expressions in Equation 5.1-14 into the integral term of Equation 5.1-3 yields the following integral expressions for each element:

$$[S_1]_e = \int_0^L \{N''\}^T EI \lfloor N'' \rfloor dx$$
$$[S_2]_e = \int_0^L \{N\}^T k \lfloor N \rfloor dx$$
$$\{f\}_e = \int_0^L \{N\} q dx$$

Equation 5.1-15

where: $[S_1]_e$, $[S_2]_e$, and $\{f\}_e$ correspond to the first, second, and third terms of the integral in Equation 5.1-3

These expressions are evaluated and assembled for each element. The shear and moment terms appearing in Equation 5.1-3 are used to define the boundary conditions. The $[S_1]_e$ and $[S_2]_e$ terms define the stiffness matrices and the $\{f\}_e$ term represents the loading. After collecting the element matrices into a global matrix, the resulting expression shown in Equation 5.1-16 can be solved for the nodal deflections. The matrices that result from this model are banded and symmetric allowing for a compact storage arrangement. The FEA program written in MATLAB® uses Gaussian elimination to solve the overall matrix equation.

$$[SK]\{W\} = \{Q\}$$

Equation 5.1-16

where: [SK] is the global stiffness matrix

{W} is the array of nodal deflections

{Q} is the forcing vector

The FEA program constructed in MATLAB® completes the integrations specified in Equation 5.1-15 over the array of elements, assembles the global matrices and solves for the nodal deflections in Equation 5.1-16. A flowchart illustrating the execution of this program is displayed in Figure 7-3.

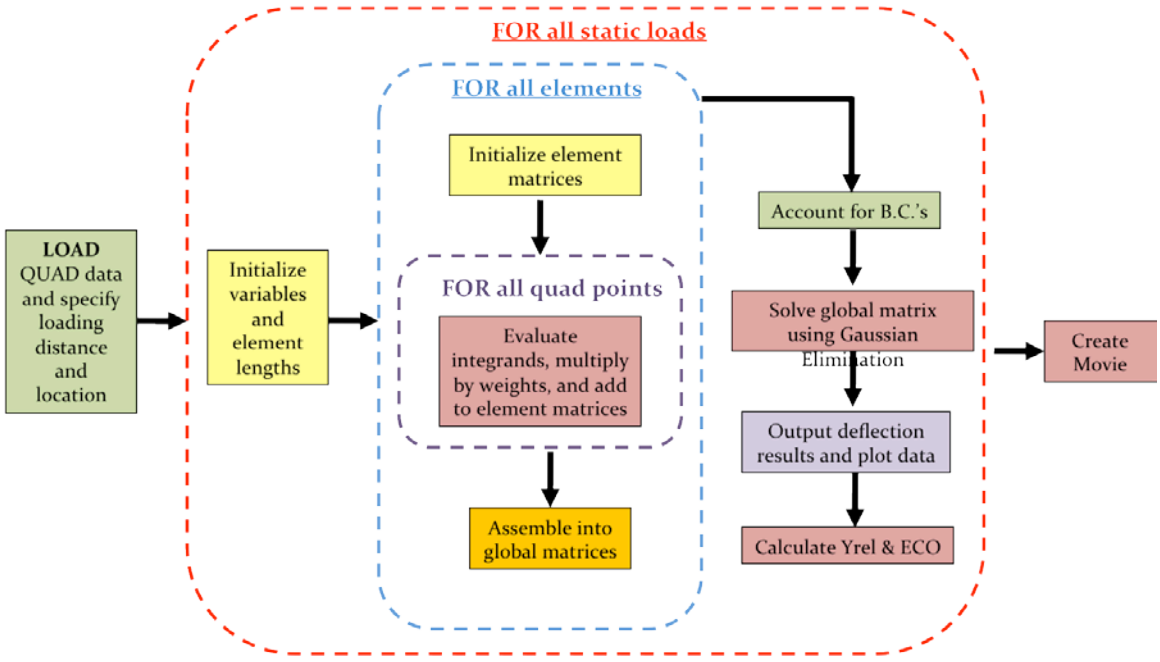

Figure 7-3. Flowchart of Custom FEA Computer Program

The FEA program is an extension and adaptation from similar programs developed in Thompson (2005). The actual code is divided into four separate MATLAB® files designated as `FEM.m`, `INITIAL.m`, `SF.m`, and `sGAUSS.m`. The main file, `FEM.m`, controls the program flow, integrates the element matrices, and plots the results. The execution of the program begins by loading the quadrature weights and points from a separate text file, `QUAD`, stored in the program directory. The loading is defined in the file `INITIAL.m`, which also specifies the model dimensions and initializes all variables. A program loop is used to traverse through a series of static loads as specified by the diagram in Figure 7-3. This method of quasi-static loading is described in the next section and allows for a simple calculation of the Yrel measurement found with the UNL system.

Within each loading cycle, the element matrices are constructed and then integrated within the main program using the `SF.m` file. This file defines the approximating shape functions and their derivatives. The element matrices are successively assembled into the global matrix. Once the global matrix is constructed, the boundary conditions are taken into account, and the nodal deflections determined using the `sGAUSS.m` file. The main program displays deflection plots of the track for each loading cycle. These plots include graphics of the Yrel and ECO measurements and the data that would be found by the UNL system. After the specified section of track has been traversed, a movie is created by merging together the individual plot frames.

7.1.3 Quasi-Static Loading and Yrel Computation

The main goal of the FEA program is to analyze the track response from the perspective of the UNL measurement system. The data is collected from a moving rail car and expressed by the Yrel measurement defined previously. To simulate the movement of the railcar along the track, a quasi-static, rather than a dynamic, approach is used. Placing static loads at specific locations along the track and computing the corresponding nodal deflections completes this method. The

static loads are then translated a specified amount (12 in), and the deflections are recomputed. This process is repeated until the static loads have traversed far enough to cover a particular track feature allowing for the calculation of the corresponding Yrel and ECO data.

The quasi-static approach significantly simplifies the FEA model. To capture the resolution needed to compute Yrel and ECO data, the elements need to be small (1-in length). In addition, a relatively large number of elements are needed to capture realistic track features. Therefore, the quasi-static simplification is expected to significantly decrease computation time compared with a dynamic model.

7.1.4 Model Parameters and Visual Representation

The FEA model is visually represented by the diagram shown in Figure 7-4. Deflections occur along the *y* direction while the track extends along the *x* direction.

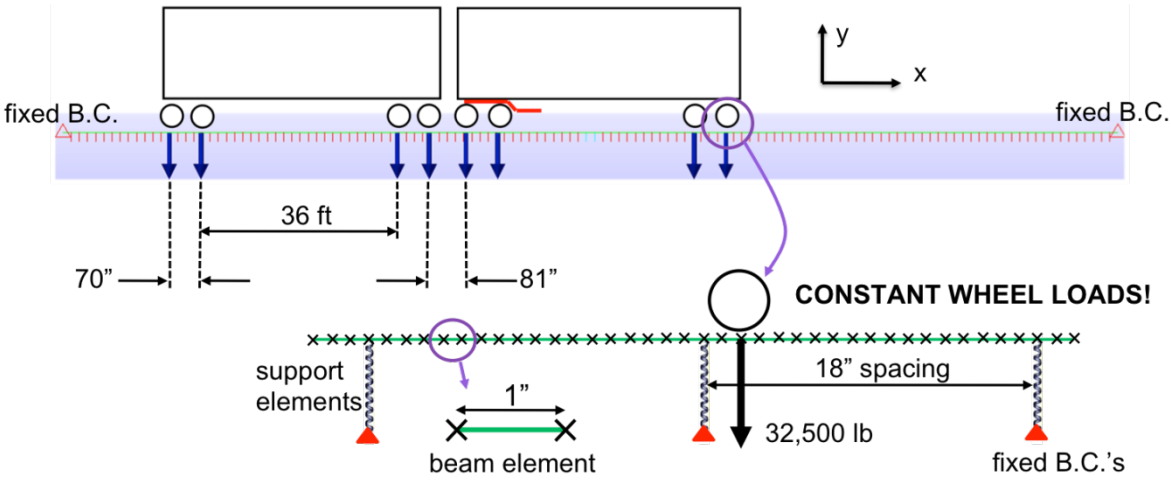

Figure 7-4. Visual Diagram of FEA Model

Each beam element is 1 inch in length. The element length was chosen through experimentation to ensure a fine enough resolution in the deflection curve to capture short-wavelength peaks in the Yrel and ECO data. The model encompasses 193.5 ft of track resulting in a total of 2,322 beam elements. This length makes certain that the loads are applied far enough away from the boundaries so that the fixed boundaries do not influence the deflection results. The beam element properties represent the 132 RE rail often found on heavy-haul coal lines as shown in Figure 7-5.

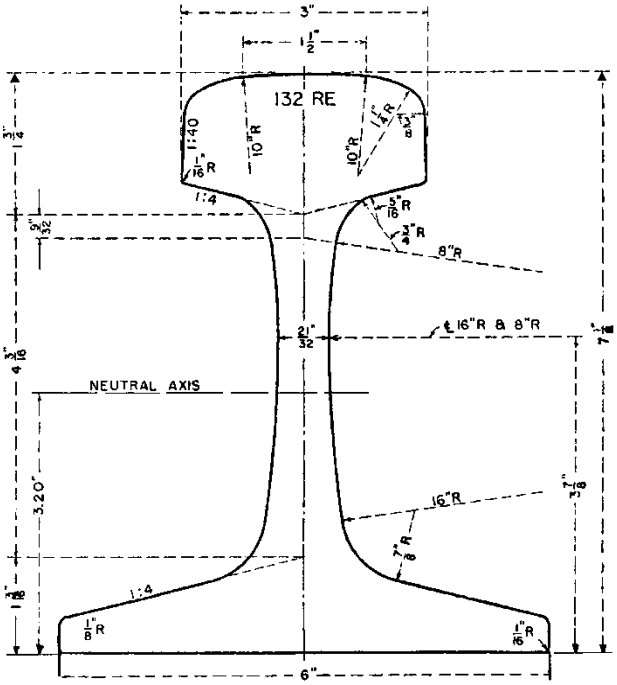

Figure 7-5. 132 RE Rail Section Properties

The static loads are configured to represent two adjacent hopper cars with the dimensions displayed in Figure 7-4. Constant load magnitudes of 32,500 lb are applied for each static load. To collect enough data to traverse typical track features, 72 static load groups are applied. The loads are translated 12 in between each cycle. Therefore, the closest any load will be to a fixed end boundary is 60 ft.

The support elements shown in Figure 7-4 are located 18 in apart to simulate the tie spacing of real track. Stiffness, rather than modulus, is defined in the FEA model. To simulate the correct stiffness, the desired modulus is multiplied by the distance between the support elements. The support stiffness for the beam elements between the support elements is set to zero. Each support element can have a unique stiffness value along the track.

The custom FEA program written in MATLAB® is applicable for linear elements only. More complicated nonlinear support elements and support elements used to represent voids are simulated in the commercial FEA software ALGOR®. The advantage of the custom FEA program is a significant reduction in computation time as well as automatic calculation and plotting of the Yrel and ECO results for each simulation. When ALGOR® is used for a simulation, the deflection results must be manually exported to text files. These text files are then imported into MATLAB® for the analysis of Yrel and ECO. The overall process is much less cumbersome with the custom program.

All of the parameters defined in Figure 7-4 are adjustable within the custom FEA program. The element dimensions, element properties, load magnitudes, and support stiffness can all be varied between individual simulations. A schematic of all possible simulation variables and combinations using either the custom FEA program or ALGOR® is illustrated in Figure 7-6.

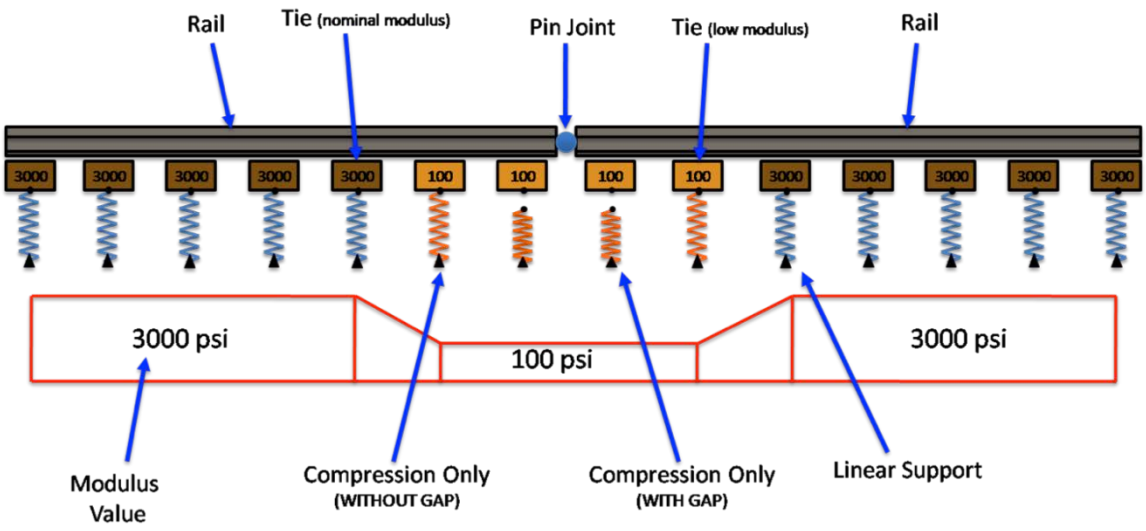

Figure 7-6. Schematic Representation of Model Input Variables

The diagram in Figure 7-6 illustrates all of the simulation possibilities but does not characterize one particular simulation. This type of diagram is used to visualize each simulation in the sections that follow. The blue springs signify linear stiffness elements. The dark brown ties correspond to a nominal modulus of 3,000 psi, whereas the lighter ties indicate areas with a softer supporting foundation. The orange springs represent nonlinear support elements. The gaps between some of the springs and ties denote areas of track with voids where some deflection occurs before the foundation provides support. The modulus profile is shown at the bottom of the figure with the specific values listed.

Another feature that can be included in the model is the pin joint shown in Figure 7-6. This element represents a joint that transfers shear forces but cannot transfer any bending moment. The pin joint is modeled using a feature known as a "beam end release" in ALGOR®. In the custom FEA program, the pin joint is modeled by creating a very small beam element (1.0E–10 in). Then, the flexural modulus and stiffness for this element are set to zero. The deflection of the nodes are kept equal by assigning a large value (1.0E+12) to the (1,1), (1,3), (3,1), and (3,3) elements of the $[S_1]$ beam-element matrix. The other values in the $[S_1]$ matrix are set to zero, which allows the slopes of the adjoining elements to be decoupled. This procedure is outlined in Thompson (2002).

7.2 Verification of FEA Model

Before proceeding with more complicated simulations, the finite element programs are verified by comparing them with the traditional Winkler model. First, the simulation of a single load in the custom FEA program is compared with the Winkler model as illustrated in Figure 7-7. In this case, a 32,500-pound load was exerted on a foundation modulus of 3,000 psi. As shown by the main figure and in the enlarged inset, the FEA results closely match the Winkler model.

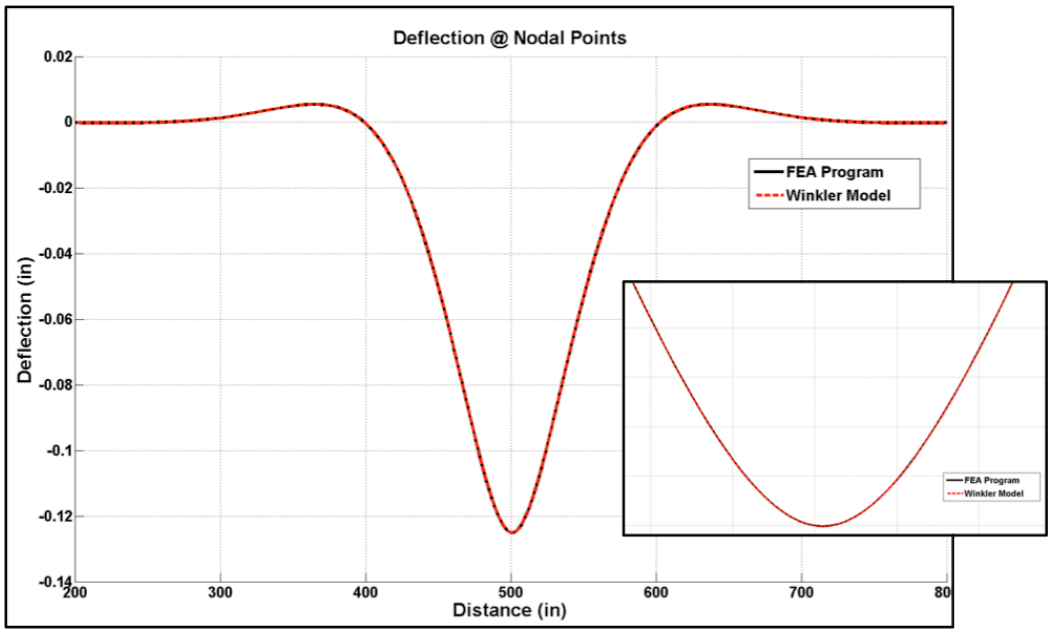

Figure 7-7. Single-Load Simulation with FEA Program Compared with Winkler Model

Next, two 32,500-pound loads were simulated in the custom FEA program, representing adjacent axles of a hopper car. Again, the results correspond very well with the deflections found using the Winkler model as displayed in Figure 7-8.

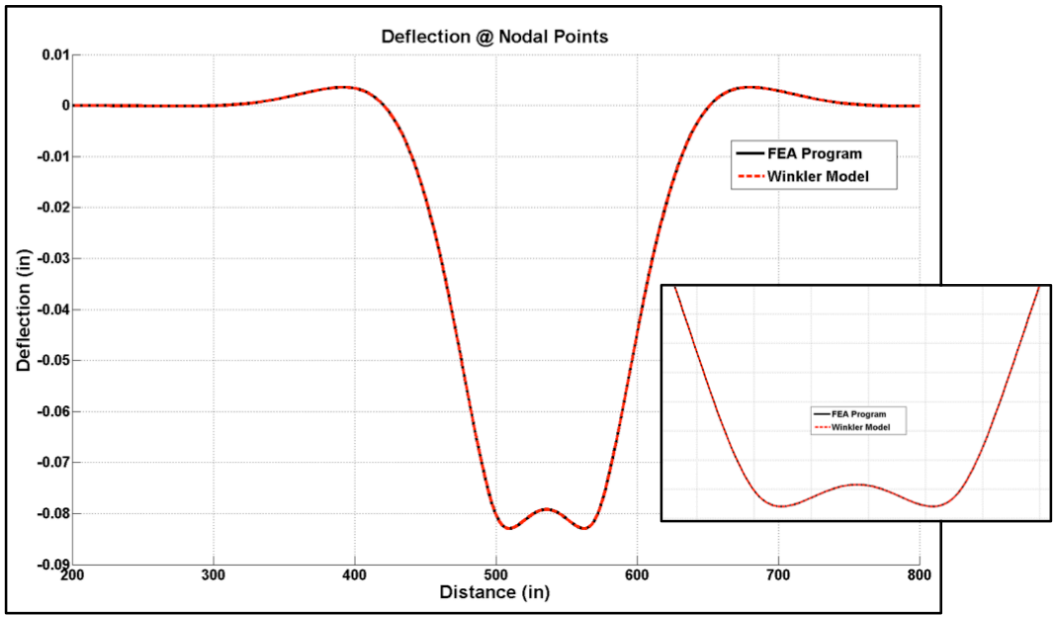

Figure 7-8. Two-Load Simulation with FEA Program Compared with Winkler Model

Verification of the custom FEA program's more advanced features is not possible using the Winkler model. For example, the Winkler model is unable to simulate varying modulus, pre-existing geometry, or joints in the rail. However, these features are precisely why the model was created. More complex simulation results are presented in the following section.

Another simulation was performed using the commercial FEA software ALGOR® and the results compared with the Winkler model. In this case, nonlinear gap elements, rather than linear elements, were used as the supporting elements in the foundation. These elements provide linear support in compression only and cannot be loaded in tension. The effect is that the foundation does not "pull down" on the rail in the areas where the track lifts up from the foundation. The results of the simulation are shown in Figure 7-9.

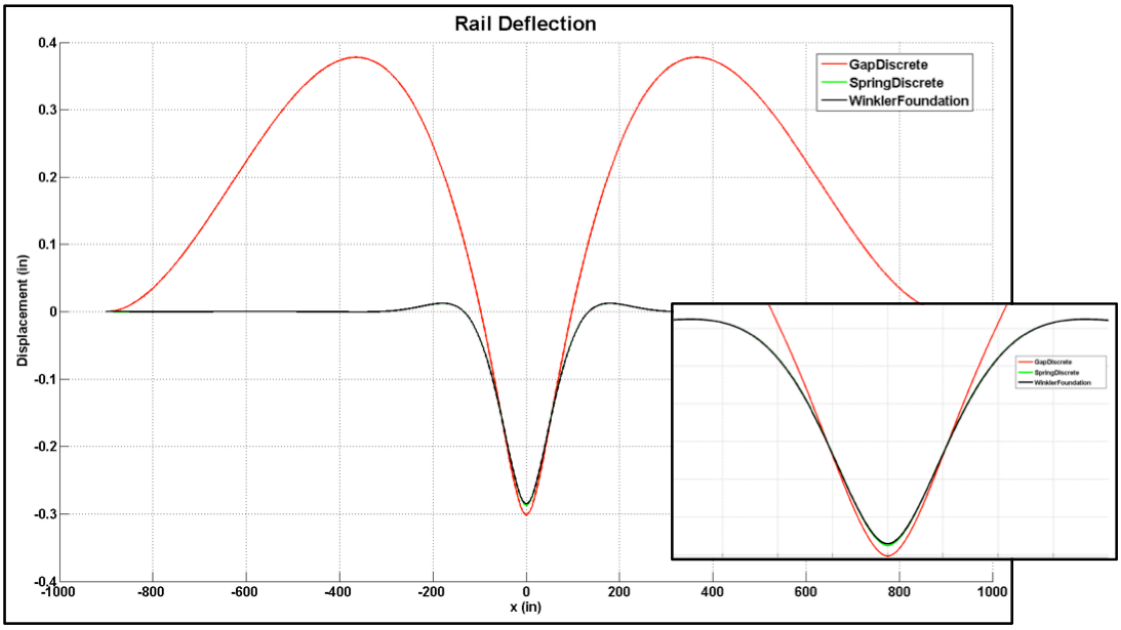

Figure 7-9. Gap Element Simulation in ALGOR® Compared with Winkler Model

Within the vicinity where the load is applied, the results match closely with the Winkler model. However, beyond approximately 5 ft on either side of the load, the track lifts up with a much steeper slope than in the Winkler model. An important fact to note is that the weight of the rail has not been included in this simulation. Rather, the simulation was completed to observe how the nonlinear gap elements compare with a linear foundation. Because of the slightly larger peak deflection and the increased track lift, more advanced simulations using these elements are expected to help explain differences observed between Yrel and ECO in field testing with the UNL track deflection measurement system. Simulations using these elements are described in the following section.

7.3 FEA Analysis and Results

This section describes several simulations performed with the custom FEA program written in MATLAB® as well as some nonlinear simulations performed in ALGOR®. The purpose of each simulation is to examine how a particular track feature or combination of features affects the shapes and magnitudes of Yrel and ECO data. The features simulated include pin joints, soft foundation support, pre-existing geometry, voids, and several combinations of the parameters.

7.3.1 Pin Joint

The custom FEA program was used to simulate a single pin joint as illustrated in Figure 7-10. In this case, the pin joint transfers shear loads but not bending moments. Therefore, this model represents the properties of a failing joint (Kerr, 2003). The foundation is modeled using linear support elements with a modulus of 3,000 psi. The length of the model (193.5 ft) is not represented in the diagram of Figure 7-10 or any of the other simulation schematics to follow. These diagrams are intended for visualization of the specific track feature modeled, in this case the joint, and these schematics are not of the complete model.

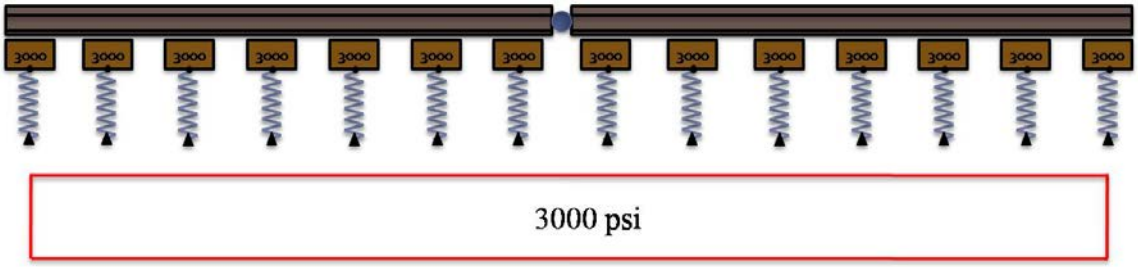

Figure 7-10. Schematic of FEA Model with Pin Joint

As mentioned earlier, the custom FEA program loops through a series of static loads to obtain the data needed to compute Yrel and ECO. The nodal deflections due to each load are plotted in individual frames and compiled into a movie for visualization as shown in Figure 7-11. The movie illustrates the loads moving from right to left along the track and plots the Yrel, ECO, and loaded-profile curves. The Yrel data is computed from the instantaneous rail deflection, whereas the ECO data is determined from the loaded profile. The loaded profile is calculated from the deflection of the leading axle (the inboard axle beneath the red beam on the UNL hopper car).

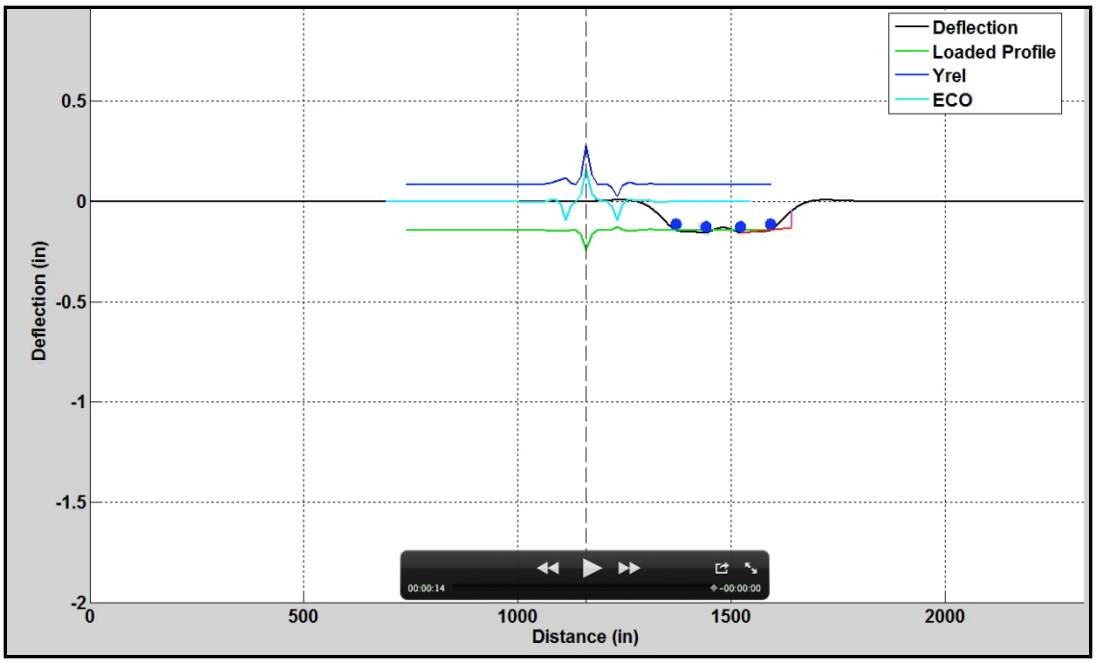

Figure 7-11. Movie Frame from FEA Simulation with Pin Joint

The final Yrel and ECO results are shown in Figure 7-12. The ratio of ECO to Yrel is 0.54 with a maximum Yrel peak of 0.25 in and the maximum ECO at 0.15 in. The shapes of each curve closely match those measured in the field by the UNL system (e.g. Figure 6-23).

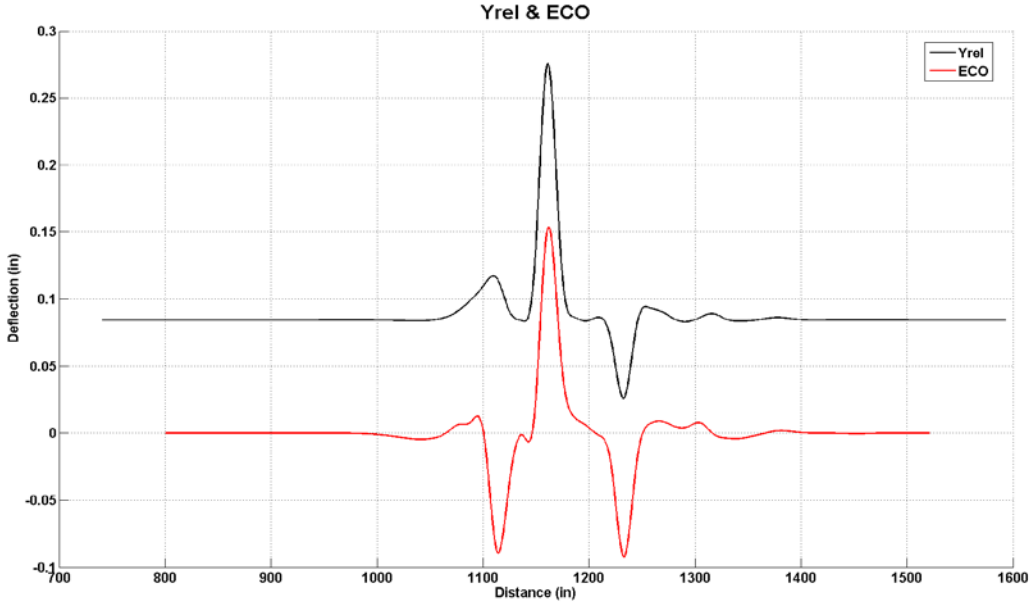

Figure 7-12. Yrel and ECO Results from FEA Simulation with Pin Joint

The results in Figure 7-12 reveal an interesting point concerning failing joints. Field measurements with the UNL system include large Yrel peaks (1 in or more) at the location of very poor joints. Certainly, a joint that does not transfer any bending moment would be considered to be in very poor condition. However, this feature that represents a joint bar with

loose bolts alone did not produce the magnitude of peak expected. To analyze this phenomenon further, the following simulation was completed.

7.3.2 Pin Joint with Bad Ties

The custom FEA program was again used to simulate a pin joint but with the addition of two poorly supported ties. The linear foundation support was reduced to 100 psi for each tie on either side of the joint as displayed in Figure 7-13.

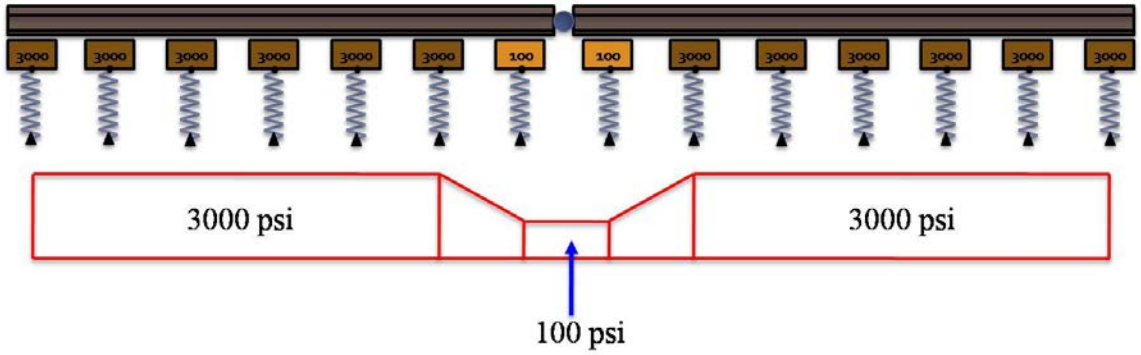

Figure 7-13. Schematic of FEA Model with Pin Joint and Two Bad Ties

As before, a movie was plotted during the simulation to visualize the results. The movie frame shown in Figure 7-14 was plotted shortly after the leading axle traversed the pin joint. This image reveals the usefulness of the custom FEA program. The deflection of each axle is apparent in the movie along with the chord used to compute Yrel. The image provides a way to correlate the axle deflections and Yrel chord with the Yrel and ECO data for a particular location.

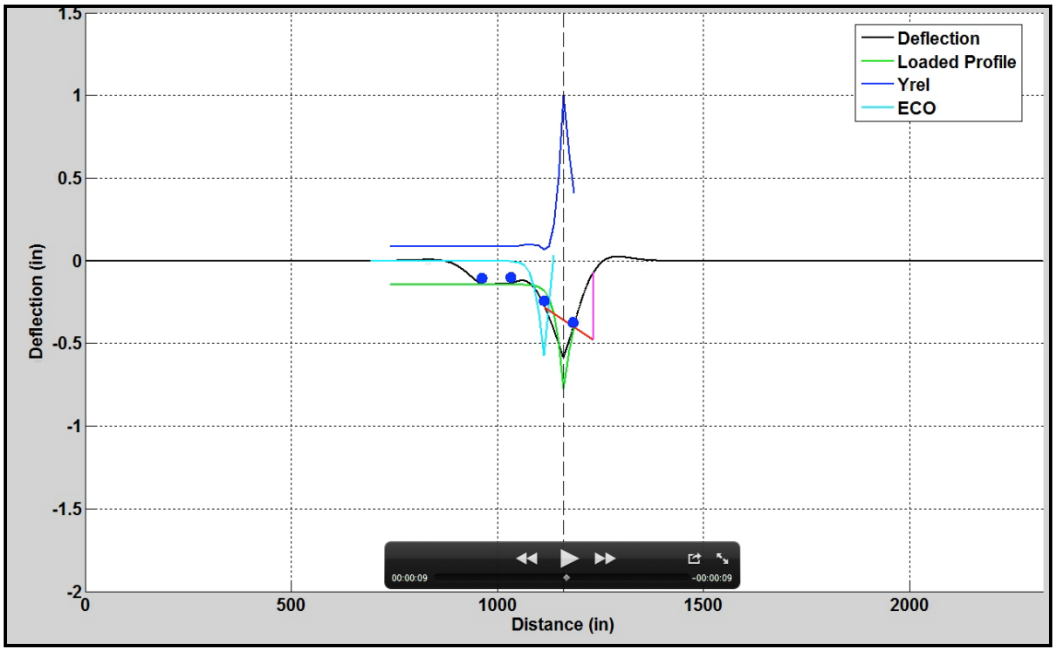

Figure 7-14. Movie Frame from FEA Simulation with Pin Joint and Two Bad Ties

The final Yrel and ECO results are shown in Figure 7-15. The ratio of ECO to Yrel is 0.91 with the maximum Yrel peak of 1.0 in and the maximum ECO peak of 0.91 in. Obviously the addition of two poorly supported ties around the joint led to significantly higher peaks in the Yrel and ECO data. The sharpness and magnitude of the Yrel peak is similar to data measured in the field at the location of failing joints. However, the peak in ECO, which nearly matches the one in Yrel, is not always expected as displayed in the bottom portion of Figure 7-15. In fact, as described in earlier sections, pre-existing unloaded geometry is expected to be the main contribution in the calculation of ECO. Yet, this simulation did not include any unloaded geometry effects. This result is discussed in more detail at the end of the section.

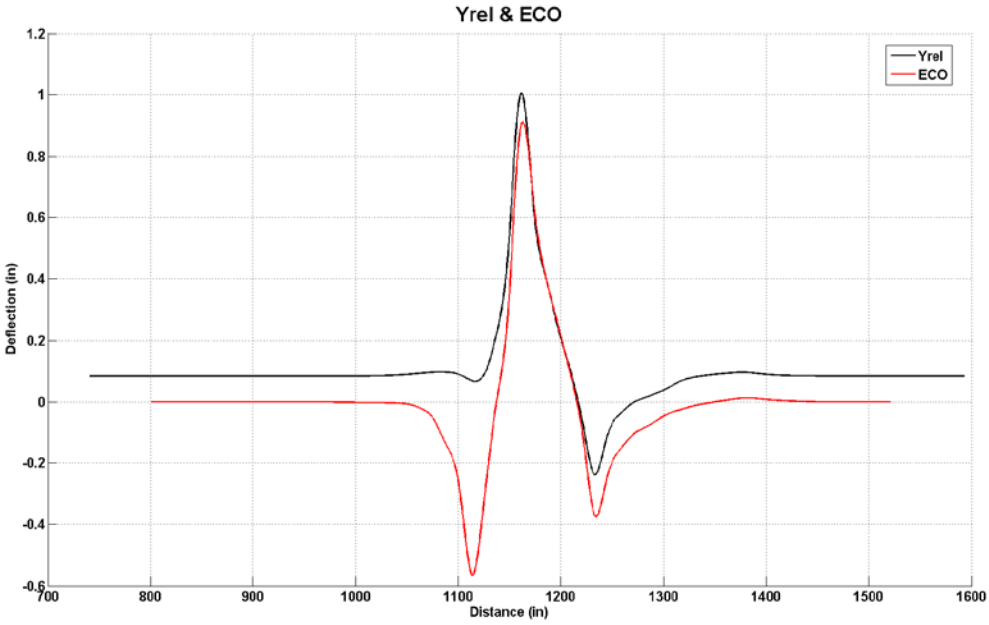

Figure 7-15. Yrel and ECO Results from FEA Simulation with Pin Joint and Two Bad Ties

7.3.3 Pin Joint with Voids

The complexity of the simulation is further increased with the inclusion of voids and nonlinear elements as shown in Figure 7-16. The voids and nonlinear elements are modeled with gap elements in ALGOR®. The size of each void is listed beneath the corresponding element in Figure 7-16. A maximum void of one inch occurs beneath the pin joint. The support modulus is also slowly decreased to a minimum beneath the joint.

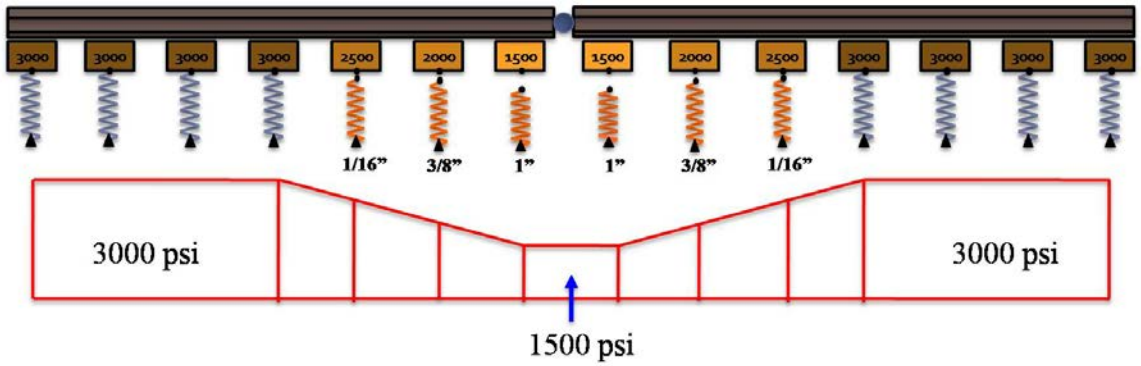

Figure 7-16. Schematic of FEA Model with Pin Joint, Bad Ties, and Voids

The use of gap elements prevents the foundation from "pulling down" on the track where it lifts up from the foundation. The configuration of the gap elements with voids leads to a nonlinear deflection curve as shown in Figure 7-17. This sort of nonlinear deflection curve is similar to the one measured by Zarembski and Choros (1980). Despite the traditional use of linear models, the actual response of the track is expected to be somewhat nonlinear (Sussmann et al., 2001; Lu, 2008). The response shown in Figure 7-17 represents the softer support associated with the seating load followed by the stiffening of the track as the various components compress together.

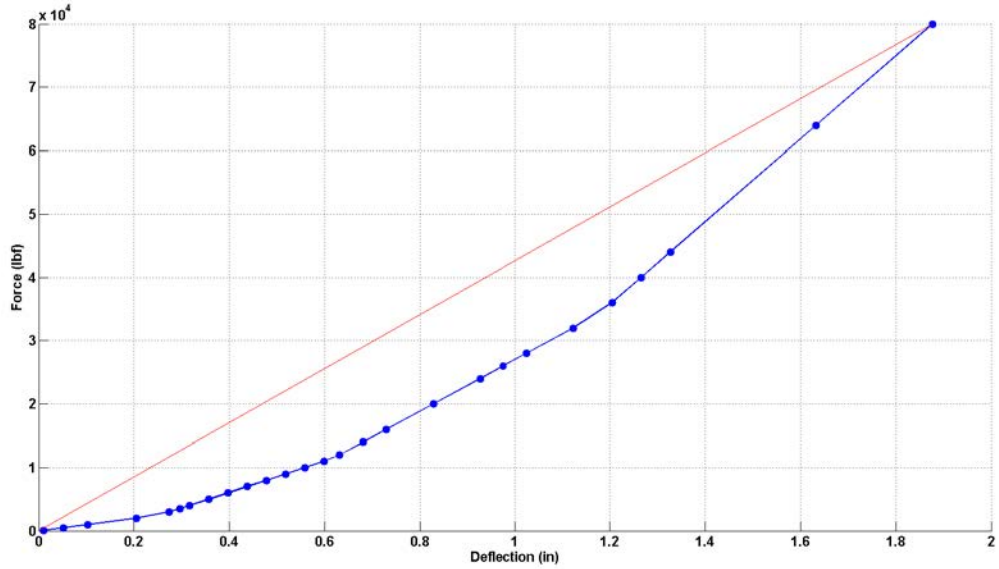

Figure 7-17. Nonlinear Deflection Curve for FEA Model with Voids

The final Yrel and ECO results are shown in Figure 7-18. The ratio of ECO to Yrel is 0.93 with the maximum Yrel peak at 1.4 in and the maximum ECO peak at 1.3 in. The decrease in support led to an increase in the Yrel peak as might be expected. However, the ratio between Yrel and ECO remained essentially the same. Therefore, the discrepancy between Yrel and ECO, found in real measured data and shown in the bottom of Figure 7-18, must result from some other effect not yet present in the simulations.

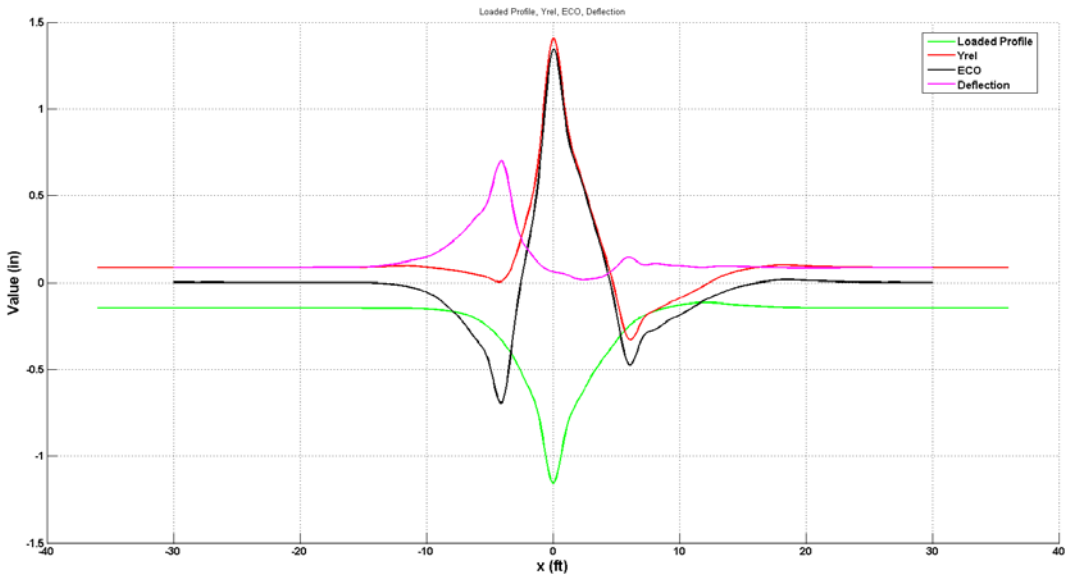

Figure 7-18. Yrel and ECO Results from FEA Simulation with Pin Joint, Bad Ties, and Voids

7.3.4 Pre-Existing Geometry

To study how pre-existing geometry influences Yrel and ECO data, a 1-inch rise over 30 ft was simulated in the track as displayed in Figure 7-19. Again, the diagram is not drawn to scale. The foundation modulus was kept constant at 3,000 psi.

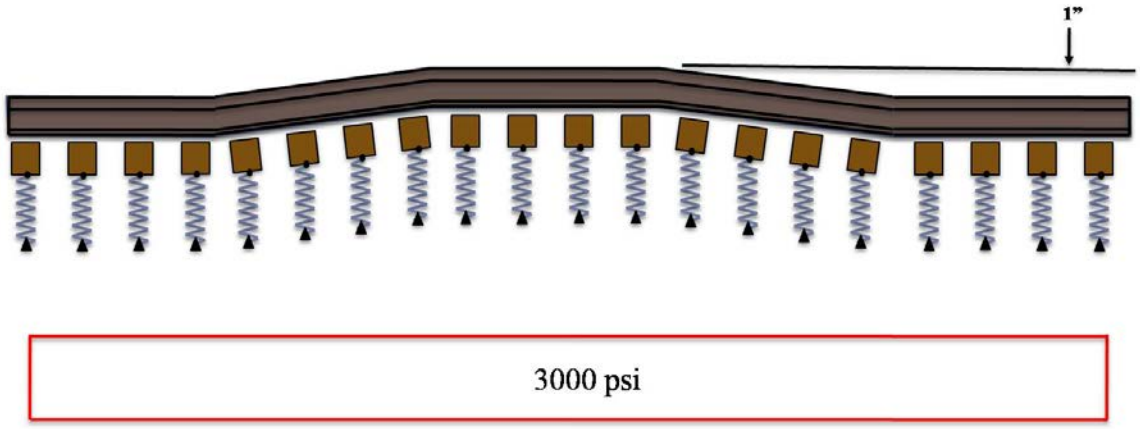

Figure 7-19. Schematic of FEA Model with Pre-Existing Geometry

The final Yrel and ECO results from the simulation are shown in Figure 7-20. The ratio of ECO to Yrel is 0.8 with the maximum Yrel at 0.46 in and the maximum ECO at 0.37 in. The data is symmetric about the geometry feature. The geometry was created with two sloped and one horizontal track segments as shown in Figure 7-19. These regions are evident in the data as both the Yrel and ECO curves peak as the loads move into and out of the sloped regions.

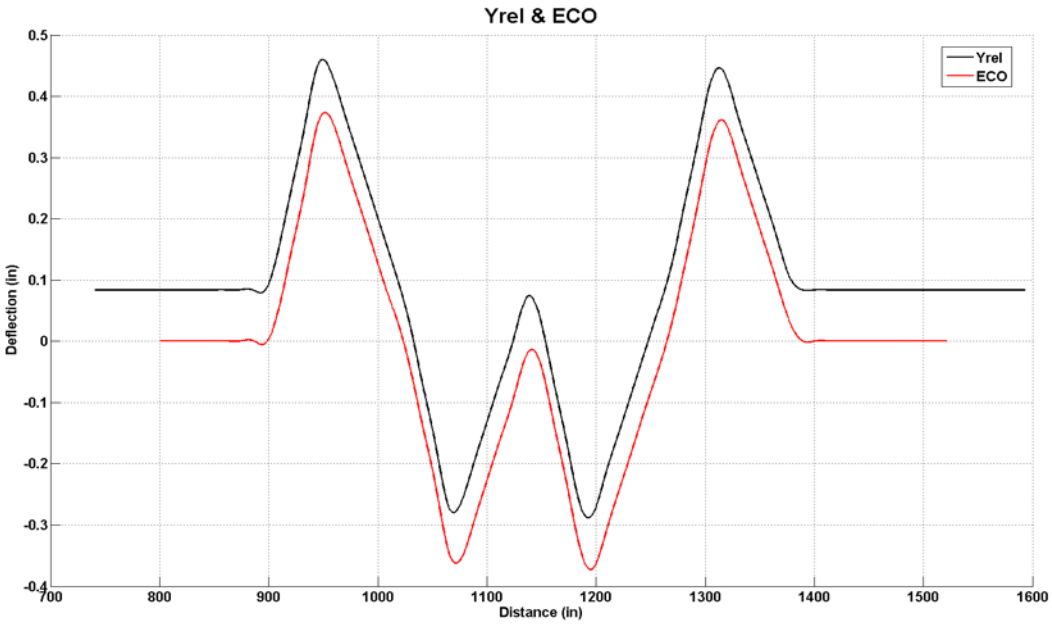

Figure 7-20. Yrel and ECO Results from FEA Simulation with Pre-Existing Geometry

The simulation results verify that relatively short wavelength geometry can affect the Yrel measurement. As shown in Figure 7-20, the Yrel and ECO data match very closely. Therefore, these results also validate the method of eliminating the effect of pre-existing geometry as described in previous chapters. Since both curves are nearly the same, subtracting ECO from Yrel should remove the geometry component in the Yrel measurement. However, the interaction between these two measurements with respect to modulus and geometry is complex. For example, ECO closely matches Yrel in the other simulations as well despite the absence of pre-existing geometry.

7.3.5 Large Mud Hole

The last simulation is completed to examine the effect of poor support over an extended region of track. The diagram for this simulation is shown in Figure 7-21. In this case, 10 ties have a reduced support modulus of 250 psi.

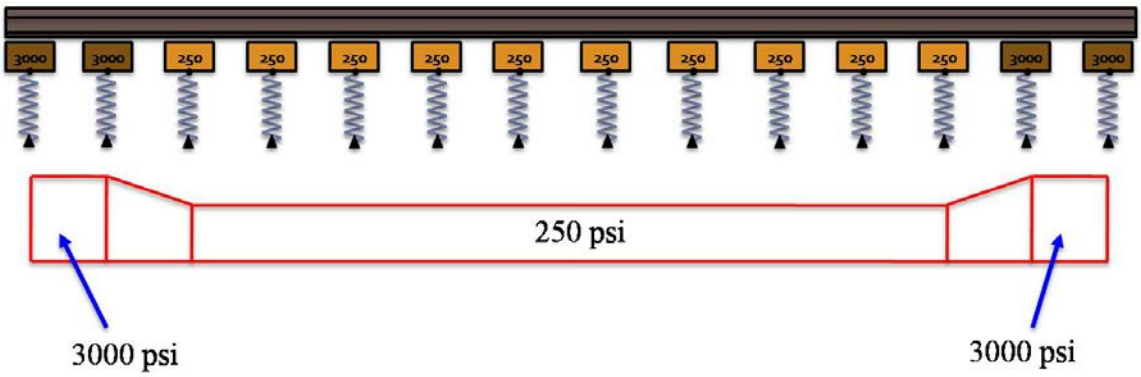

Figure 7-21. Schematic of FEA Model with 10 Bad Ties

The Yrel and ECO results from the simulation are shown in Figure 7-22. The ratio of ECO to Yrel is 0.91 with the maximum Yrel at 0.53 in and the maximum ECO at 0.48 in. Wider peaks in the data result from the long section of low support modulus. Of particular interest is that the ECO peak is shifted with respect to the Yrel peak. This effect is present in all simulations when the section of low support modulus is longer than the 10-foot chord used to calculate Yrel and ECO.

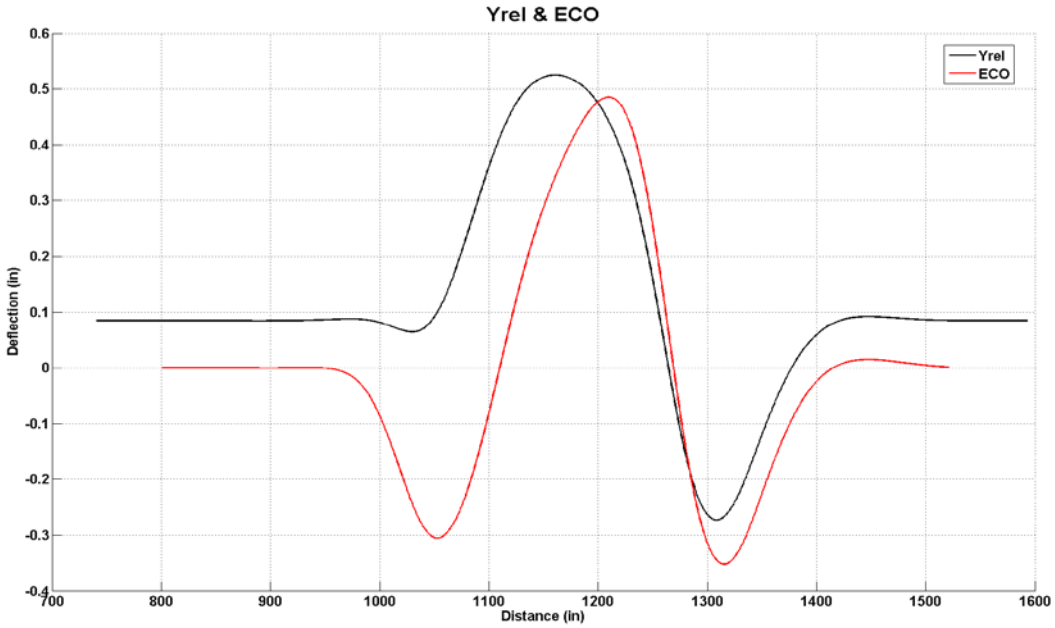

Figure 7-22. Yrel and ECO Results from FEA Simulation with 10 Bad Ties

7.4 Suggestions for Further Development

The results from all of the simulations discussed in the previous section are displayed in Table 7-1 below.

Table 7-1. Results of FEA Simulations

Simulation Scenario	Yrel (in)	ECO (in)	Ratio: ECO/Yrel
Pin joint only (linear elements)	0.28	0.15	0.54
Pin joint with two, 100 psi modulus ties on each side (linear elements)	1.0	0.91	0.91
Pin joint with 1-inch gap between joint and supporting foundation	1.4	1.3	0.93
Continuous rail with pre-existing geometry (3,000 psi modulus)	0.46	0.37	0.8
Continuous rail with 10 ties of 250 modulus (linear elements)	0.53	0.48	0.91

The simulation results provide good insight into how specific track features might affect the shape and magnitude of Yrel. Of particular interest, however, is that the ECO data nearly matched the Yrel values in each case. This effect is certainly observable in real measured data with the UNL system and has been shown at several locations, along with the deteriorated track conditions. Yet, these results do not indicate why certain track features lead to large peaks in Yrel with much smaller peaks in ECO, as shown in the lower portion of Figure 7-1. Therefore, some parameter or combination of parameters present during the actual measurement of this data is not represented in the simulations.

Considering how the FEA model is created in comparison to how the real Yrel and ECO data is measured may provide a basis for further development of the simulations. One possible discrepancy is the exclusion of dynamic interactions between the measurement vehicle and the deflection of the track. Dynamic effects were not included in the model to reduce its complexity and corresponding computation time. However, previous research has shown that at higher speeds, the dynamics should be included in the model (Carr, 1999). The dynamic response of Yrel and ECO to short wavelength perturbations may be different, and this may contribute to the missing peak in the ECO data. Therefore, it is recommended that further development of these FEA simulations include the dynamics of the rail car interacting with the deflection of the track. However, discrepancies between Yrel and ECO are observed at speeds as low as 20–25 mph (the minimum speed often supported by track profile measurement systems) where dynamic loads would not be expected to cause the observed differences in Yrel and ECO. It is believed that dynamics can account for some small portion of these differences, but that improved understanding of the mechanics of the observed track behavior is necessary to fully explain the observed differences.

Another possible contribution to the discrepancy between Yrel and ECO peaks may be the method by which ECO is calculated. The ECO measurement is calculated from space curve data provided to UNL from track geometry vehicles. Track geometry vehicles use multiple high-precision accelerometers to measure geometric properties of the track. The vertical accelerations can be integrated to determine the vertical rail profile. This profile is then used to calculate the 10-foot ECO. This method raises the possibility that sampling and frequency issues may result in missing data peaks for short-wavelength track features. The accelerometers used to measure the rail space curve have a specific sampling rate. The data is then filtered to remove low-frequency (<0.3 hertz) and high-frequency (>60 hertz) noise. The resulting signal is then integrated, filtered, and integrated again to obtain the vertical displacement of the rail profile. Finally, the ECO data is computed from the resulting space curve profile. This procedure may result in lower peaks of ECO than Yrel at the location of short-wavelength track perturbations (at failing joints, for example). Again, these limitations may contribute in part to the difference observed between Yrel and ECO.

To study how the real computation of ECO compares with the ECO measurement found in the simulations, accelerometers have been added to the UNL system as described in Section 3. These accelerometers are mounted to the bearing adapters above the inboard axle (axle 3 of the UNL car). These accelerometers have been used in a few tests, but as of yet, have not produced conclusive results. Ongoing development is underway to match the UNL accelerometer output with data provided by track geometry vehicles. The goal is that these instruments will eliminate

the need for data provided by the track geometry vehicles and verify the computation of ECO used in the UNL deflection measurement system.

The sites that show a difference between Yrel and ECO are likely the most significant finding of this research. These sites are the focus of research to understand the complex track behavior and dynamics that occur in deteriorated track sites. These sites are significant and often exist on real track and have been commonly observed during tests. It is believed that these locations have nonuniform support and the track behavior at these locations is complex. It is also believed that these differences cannot be fully explained with vehicle dynamics and measurement differences or sampling issues. These sites not behaving according to expected standards may pose a risk to the safe maintenace of track. More analysis, and most importantly, field tests and site instrumentation data are needed to fully understand these sites so that the risks can be more fully understood and the data from the UNL measurement system can be properly thresholded to identify and prioritize these potentially significant problem sites.

8 Summary and Conclusions

UNL has been conducting research sponsored by FRA's Office of Research and Development to create a system to measure VTD/modulus from a moving rail car. Previous work has suggested that the system can identify critical maintenance problems not detected by other inspection methods including standard track geometry.

This report presents the theoretical basis for the UNL-developed measurement system, as well as a review of mathematical representations of track stiffness and resulting track support analysis. FEA analysis is presented that represents quasi-static track analysis with a complex track model with nonlinear and varying stiffness. Also, a new theoretical model for track, along with a nontraditional definition of track modulus, is presented that represents a cubic relationship between the applied distributed load and the track vertical deflection.

The system has been implemented and significant field testing has been performed. The prototype field system is described along with a calibration procedure. Results of a field validation test are presented that show the measurement is accurate and repeatable. Finally, results of field tests are presented along with some interpretation and analysis of various sites including the relative changes in stiffness over joints, bridges, and approaches.

The work presented here has been closely analyzed by personnel at FRA and the John A. Volpe National Transportation Systems Center (Volpe Center). FRA, Volpe Center, and UNL will continue to consider the following issues:

1) There is indication that the UNL measurement, designated as Yrel, can locate and systematically quantify track problem sites.

2) The UNL measurement (Yrel) is different from standard geometry measurements (e.g., ECO calculated from loaded profile information).

3) The UNL system can identify critical maintenance problems not found by other inspection methods including short wavelength processed track geometry or VTI data.

4) Some guidelines are suggested here to form a basis of thresholds for interpreting Yrel and associated track deflection data, but more study and tests are needed to define threshold criteria.

5) More work including field tests and site specific measurements are needed to better characterize the complex behavior of locations and evaluate the risk at sites where advanced track deterioration has been associated with the trend of the UNL measurement (Yrel) significantly exceeding comparable ECO data from track geometry.

9 References

[1] Arnold, R., Lu, S., Hogan, C., Farritor, S., Fateh, M., and El-Sibaie, M. (2006). Measurement of vertical track modulus from a moving railcar. In Proceedings of the *AREMA 2006 Annual Conference*, Louisville, KY, 17–20 Sept.

[2] ASCE-AREA Special Committee on Stresses in Railroad Track, Bulletin of the AREA, First Progress Report Vol. 19, 1918; Second Progress Report Vol. 21, 1920.

[3] Boresi, A. P., and Schmidt, R. J. (2003). *Advanced mechanics of materials* (6th ed.). New York: John Wiley.

[4] Cai, Z., Raymond, G. P., and Bathurst, R. J. (1994). Estimate of static track modulus using elastic foundation models. *Transportation Research Record 1470*, 65–72.

[5] Carr, G. A. (1999 Sept.). Dynamic response of railroad track induced by high speed trains and vertical stiffness transitions with proposed method of measurement. (Master thesis). Tufts University, Medford, MA.

[6] Davis, D. D., Otter, D., Li, D., and Singh, S. (2003 Dec.). Bridge approach performance in revenue service. *Railway Track and Structures*, pp. 18–20.

[7] Ebersohn, W., Trevizo, M. C., and Selig, E. T. (1993). Effect of low track modulus on track performance. In Proceedings of the *Fifth International Heavy Haul Conference*, International Heavy Haul Association, pp. 379–388.

[8] Ebersohn, W., and Selig, E. T. (1994). Track modulus on a heavy haul line. *Transportation Research Record 1470*, 73–83.

[9] Heelis, M. E., Collop, A. C., Chapman, D. N., and Krylov, V. (1999). Predicting and measuring vertical track displacements on soft subgrades. In Proceedings of the *Railway Engineering—Second International Conference and Exhibition*, London, UK, 25–26 May.

[10] Kerr, A. D. (1976). On the stress analysis of rails and ties. In Proceedings of the *American Railway Engineering Association*, Vol. 78, pp. 19–43.

[11] Kerr, A. (2003). *Fundamental of railway track engineering.* Omaha, NE: Simmons-Boardman Books.

[12] Kierzenka, J., and Shampine L. F. (2001). A BVP Solver based on residual control and the MATLAB PSE. ACM TOMS, Vol. 27, No. 3, pp. 299–316.

[13] Li, D., Hass, K., and Meddah, A. (2002 June). Moving closer to performance-based track geometry inspection. *Railway Track and Structures*, 15–17.

[14] Lu, S. (2008). *Real-time vertical track deflection measurement system*. (Doctoral dissertation). Department of Mechanical Engineering, University of Nebraska, Lincoln, NE.

[15] Lu, S., Hogan, C., Minert, B., Arnold, R., Farritor, S., GeMeiner, W., and Clark, D. (2007). Exception criteria in vertical track deflection and modulus. In Proceedings of the *2007 ASME/IEEE Joint Rail Conference and Internal Combustion Engine Spring Technical Conference*, Pueblo, CO, 13–16 March.

[16] Lu, S., Farritor, S., Arnold, R., GeMeiner, W., Clark, D., Al-Nazer, L., Carr, G., and El-Sibaie, M. (2008). Measurement of vertical track modulus—Field testing, repeatability, and effects of track geometry. In Proceedings of the *2008 Joint Rail Conference*, Wilmington, DE, 22–24 April.

[17] McVey, B. (2006 May). *A nonlinear approach to measurement of vertical track deflection from a moving railcar*. (Master thesis). University of Nebraska, Lincoln, NE.

[18] Meyer, M. B. (2002 May). *Measurement of railroad track modulus on a fast moving railcar*. (Master thesis). University of Nebraska, Lincoln, NE.

[19] Norman, C. (2004 May). *Measurement of track modulus from a moving railcar*. (Master thesis). University of Nebraska, Lincoln, NE.

[20] Raymond, G. P. (1985). Analysis of track support and determination of track modulus. *Transportation Research Record 1022*, 80–90.

[21] Read, D., Chrismer, S., Ebersohn, W., and Selig, E. (1994). Track modulus measurements at the Pueblo soft subgrade site. *Transportation Research Record 1470*, 55–64.

[22] Selig, E. T., and Li, D. (1994). Track modulus: Its meaning and factors influencing it. *Transportation Research Record 1470*, 47–54.

[23] Sussmann, T. R., Ebersohn, W., and Selig, E. T. (2001). Fundamental nonlinear track load-deflection behavior for condition evaluation. *Transportation Research Record 1742*, 61–67.

[24] Thompson, R., and Li, D. (2002 Feb.). Automated vertical track strength testing using TTCI's track loading vehicle. *Technology Digest*.

[25] Zarembski, A. M., and Choros, J. (1980). On the measurement and calculation of vertical track modulus. In Proceedings of the *American Railway Engineering Association*, Vol. 81, pp. 156–173.

[26] Zarembski, A. M., and Palese, J. (2003 Aug.). Transitions eliminate impact at crossings. *Railway Track and Structures*, 28–30.

Abbreviations and Acronyms

ASCE-AREA	American Society of Civil Engineers/
BNSF	BNSF Railway
BOEF	beam on an elastic foundation
BVP	boundary value problem
CEP	circular error probable
cm	centimeter
DAQ	data acquisition
ECO	end chord offset
FEA	finite element analysis
ft	feet
GDOP	geometric dilution of precision
GPa	gigapascal
GPR	ground-penetrating radar
GPS	global positioning system
GRMS	Gage Restraint Measurement System
in	inch
km/hr	kilometers per hour
kn	kilonewton
lb	pound
lbf	pound-force
LVDT	Linear Variable Differential Transformers
m	meter
MGT	million gross ton
mm	millimeter
MN/m	millinewton per meter
MPa	megapascal
mph	mile per hour
N	Newton
PC	personal computer
psi	pounds per square inch

PVM	precision measurement vehicle
TLV	track loading vehicle
UHF/VHF	ultrahigh frequency/very high frequency
UNL	University of Nebraska-Lincoln
UPRR	Union Pacific Railroad
Volpe Center	John A. Volpe National Transportation Systems Center
VTD	vertical track deflection
VTI	vehicle track interaction